Title
Reactive Limestone as a Strategy Towards Low-Clinker Factor Cements

Author
Puerta Falla, Guillermo Leon

Publication Date
2016

Peer reviewed|Thesis/dissertation

UNIVERSITY OF CALIFORNIA

Los Angeles

Reactive Limestone as a Strategy Towards Low-Clinker Factor Cements

A dissertation submitted in partial satisfaction of the

requirements for the degree Doctor of Philosophy

in Civil Engineering

by

Guillermo L. Puerta Falla

2016

ABSTRACT OF THE DISSERTATION

Reactive Limestone as a Strategy Towards Low-Clinker Factor Cements

by

Guillermo L. Puerta Falla

Doctor of Philosophy in Civil Engineering

University of California, Los Angeles, 2016

Professor Gaurav Sant, Chair

The production of ordinary portland cement (OPC) accounts for 5-7 % of global CO_2 emissions [1,2,3]. The growing demands for new infrastructure, and the need for modernizing existing infrastructure and the associated cement-use has brought into question the viability and sustainability of cement-based materials for the coming decades. This is significant as legislation and climate policy are expected to substantially impact the construction sector as national governments try to meet climate change agreements. Carbon dioxide emissions related to cement

production are attributable to: fuel consumption (40 %), electricity and transport (10 %) and the calcination of limestone (50 %). The last contributor ("calcination") is related to the release of CO_2 from limestone ($CaCO_3$); the principal raw materials used in cement manufacture. To reduce the CO_2 impact of cement production, there is interest in replacing OPC in the binder phase in concrete, by fine limestone. However, the replacement of OPC by limestone results in a reduction in mechanical properties, due to dilution, as the cement content is reduced. For this reason, prevailing codes limit OPC replacement at the level of 15 %, or less, by mass of binder (ASTM C 595). With this view in mind, this thesis seeks to uncover:

- If strategic manipulations in the cement chemistry made to favor the formation of the carboaluminate phases can mitigate the extent of strength reduction,
- What is the role of the solubility and dissolution rate of the carbonate source on favoring, or hindering carboaluminate phase formation, and,
- The role of kinetic and thermodynamic factors that influence ion-exchange processes and the stability of a given AFm phase for anions that occupy adjacent positions in terms of their site occupation preference in the AFm interlayer.

By the use of a multi method approach including x-ray diffraction, thermogravimetric analysis, isothermal calorimetry, compressive strength testing, thermodynamic equilibrium simulations and boundary nucleation and growth (BNG) models, this research explores all the factors that might hinder limestone partake in hydration reactions (i.e., low dissolution, slow dissolution rate of calcite and/or kinetic constrains in ion exchange processes). In order to bring about clarity on limestone effects in cementitious formulations (or lack thereof), evolution of these systems is studied in detail from the physical and chemical perspective. Of particular relevance, chemical effects include mineralogical changes produced by solvated carbonate species and their reaction

with water and aluminate species (from C_3A or CA depending on cement type) to form calcium carboaluminate (CO_3-AFm) solid phases (monocarboaluminate-Mc and hemicarboaluminate-Hc). This is a remarkable effect as the formation of these solids consumes water, counteracting dilutive effects and reducing porosity, therefore stabilizing the mechanical performance of the system even at high limestone fraction additions. An additional chemical effect is the stabilization of the sulfate phase ettringite (AFt) which does not decompose into monosulfoaluminate (SO_4-AFm) as SO_4^{2-} ions are constantly replaced by CO_3^{2-} during the carboaluminate phase formation process.

Results from this research show that the beneficial effects caused by limestone (physical and chemical) in cementitious systems can be enhanced. However, such enhancement cannot fully compensate for dilutive effects produced when large amounts of limestone are employed. In the case of physical effects, provision of additional surface area can increase early hydration rates and bring about a more efficient use of the remaining cement fraction with slightly larger degrees of hydration. Nonetheless, as further increases in the degree of hydration are sought larger surface area provided by the limestone is required, however, as limestone becomes finer agglomeration of the limestone particles initiates effectively reducing the surface area provided and, consequently, the acceleratory effects of limestone. In the case of the chemical effects, calcium carboaluminate phase formation can be enhanced by the addition of an aluminate source in the system provided that enough water and limestone are available to complete formation. However, the low solubility, slow dissolution rate of limestone appear to be a limiting factor. In order to elucidate on these limiting factors two additional experimental programs were devised: i) study of the effects of highly soluble carbonate salts (Na_2CO_3) in cementitious systems and ii) kinetics of ion exchange in AFm phases. The first approach (“highly soluble carbonate source”)

showed that even when CO_3^{2-} ion provision is enhanced, the lack of solvated Ca^{2+} species, low water activity and/or availability lead to formation of carbonate phases with low calcium content (i.e., gaylussite and thermonitrate), with formation of this phases being detrimental for the calcium carboaluminate phases (Mc and Hc). The second approach ("kinetics of ion exchange") showed that kinetics of ion exchange is mainly governed by temperature and concentration of anionic species and are not in itself a limiting factor. Taken together, the results of this research show that beneficial effects of limestone in cementitious systems can still be improved but cannot totally compensate for dilutive effects.

Acknowledgements

The completion of this Ph.D. program is the biggest scientific achievement of my life so far. It would have been impossible to complete this program without the kind love, support and encouragement of my wife Emily Puerta and my parents.

I would also like to recognize the academic and scientific support of Prof. Gaurav Sant and Magdalena Balonis-Sant for their patience guidance and teachings through this process. The scientific inputs of Professors Aditya Kumar, Narayanan Neithalath, Jeffrey Bullar, Mark Goorsky have also been of the outmost importance throughout this research endeavor.

I also wish to express my gratitude to Professors Jennifer Jay for being part of this committee. Special recognition to Professor Scott Brandenberg for his collaboration on my academic/scientific development.

Last but not least, many thanks to all members of the LCC-PARISlab scientific community as their advice and partnership have been crucial in making this doctoral degree possible.

The dissertation of Guillermo Puerta Falla is approved

Scott Joseph Brandenberg

Jennifer Ayla Jay

Mark S. Goorsky

Jeffrey W. Bullard

Narayanan Neithalath

Gaurav Sant, Committee Chair

University of California, Los Angeles

2016

Dedico este trabajo a mi padre

Table of Contents

Chapter 1: Introduction 1

1.1 Scope and Objectives 1

1.2 Organization 4

Chapter 2: A Comparison of Intergrinding and Blending Limestone on Reaction and Strength Evolution in Cementitious Materials. 9

2.1 Scope of Chapter 2 9

2.2 Materials, Mixing Procedures and Methods 9

2.3 Experimental Results and Discussion 13

2.4 Boundary nucleation and growth Model for Cement Hydration 18

2.5 Summary and Conclusions Chapter 2 24

Chapter 3: The Influence of Filler Type and Surface Area on the Hydration Rates of Calcium Aluminate Cement. 26

3.1 Scope of Chapter 3 26

3.2 Materials and Experimental Methods 27

3.3 Experimental Results and Discussion 31

3.4 Boundary Nucleation and Growth Model for Cement Hydration 37

3.5 Summary and Conclusions Chapter 3 43

Chapter 4: Elucidating the Role of the Aluminous Source on Limestone Reactivity in Portland Cement. 45

4.1 Scope of Chapter 4 45

4.2 Materials and Methods 47

4.2.1 Materials 47

4.2.2 Particle Size Analysis Using Light Scattering 50

4.2.3 Compressive Strength Measurements 51

4.2.4 Thermal Analysis (TGA/DTG/DTA) 51

4.2.5 Quantitative X-ray Diffraction Analysis Using Rietveld Refinement (QXRD) 52

4.2.6 Thermodynamic Calculations: Prediction of Hydrated Phase Assemblage 52

4.3 Experimental Results and Discussion 57

4.3.1 Influence of Calcium Aluminate Cement (CAC) Additions 58

4.3.2 Influence of Metakaolin Additions 65

4.3.3 Influence of Hydratable Alumina Additions 69

4.4 Correlating Phase Balances to Mechanical Properties and Comparing Aluminous Agents 74

4.5 Summary and Conclusions of Chapter 4 78

Chapter 5: The Influence of Slightly, and Highly Soluble Carbonate Salts on Phase Relations in Hydrated Calcium Aluminate Cements 80
5.1 Scope of Chapter 5 80
5.2 Materials and Methods 82
5.3 Thermodynamic Calculations: Prediction of Hydrated Phase Assemblage 85
5.4 Experimental Results and Discussion 87
5.4.1 Influence of Limestone (Slightly Soluble Carbonate) Additions 87
5.4.2 The influence of Sodium (Highly Soluble) Carbonate Additions 91
5.5 Thermodynamic Calculations 94
5.5.1 The Role of Water Content on Phase Equilibria 94
5.5.2 The role of the Calcium Content of the Carbonate Source 97
5.6 Summary and Concussions Chapter 5 98
Chapter 6: Kinetics of Ion Exchange in AFm phases 100
6.1 Scope of Chapter 6 100
6.2 Materials Synthesis 102
6.3 Experimental Procedures 104
6.4 Simulations 107
6.4.1 Thermodynamic Calculations 107
6.5 Experimental Results and Discussion 109
6.6 Summary and Concussions Chapter 6 124
Chapter 7: General Conclusions 126
7.1 Scope of Chapter 7 126
7.2 General Conclusions of this Research Work 126
Chapter 8: Future Work 128
8.1 Scope of Chapter 8 128
8.2 Future Research 128
Reference List 135

Table of Figures

Figure 1: Particle size distributions for (a) cement and (b) limestone used in this study. 11

Figure 2: Representative graphs showing reaction rates as measured using isothermal calorimetry to highlight the influence of intergrinding and post-blending for: (a) Type I/II OPC, and (b) 50:50 blend of Type III and Type I/II OPC and (c) Type III OPC. 14

Figure 3: Calorimetric parameters and best fit lines (dashed lines) as a function of the area multiplier for: (a) slope during the acceleration period, (b) heat flow value at the main heat peak and (c) inverse of time required to achieve the main heat peak. The solid points are adapted from [34] and the open symbols represent mixtures with 15% blended limestone. The solid line indicates the calorimetric parameter value for the interground OPC-L cement. 15

Figure 4: The evolution of compressive strength in interground and blended limestone (paste) systems for a variety of limestone particle sizes, for two cement types over: (a) the first day and (b and c) over the first 28 days of hydration. Except the plain cement pastes (marked REF), these systems were constituted at w/s = 0.450, equivalent to w/c = 0.529 for all mixtures. 16

Figure 5: Compressive strength development at ages of 1, 3, 7 and 28 days of hydration as a function of the cumulative heat normalized by water content for the OPC-L, Type I/II and Type III cements, and their limestone blended mixtures. The thick dashed line represents the (linear) best fit line with 20% bounds placed on either direction (thin dashed lines). The datapoints adapted from Kumar et al. ([34]) include evaluations conducted on Type I/II, Type II/V and Type III cements, for cement replacement levels ranging between 0-50% (mass basis) by particle size classified limestone, for strength and heat determinations carried out at 1, 3, 7 and 28 days. The compressive strength of the 50:50 OPC blends containing 15% (blended) limestone of different

particle sizes was estimated using the heat release measured through hydration, and the strength-heat correlation function detailed in the figure. 17

Figure 6: Representative graphs which show a comparison of the measured and BNG simulated heat release behavior for binary (OPC + limestone) paste systems. 21

Figure 7: Results of the BNG calculations which describe: (a) the nucleation density as a function of the limestone particle size, and product nuclei per gram of cement as a function of: (b) the AM for the various cement types used in this study and (c) effective surface area available per unit mass of cement. The datapoints adapted from [34] include evaluations conducted on Type I/II, Type II/V and Type III cements. 22

Figure 8: The particle size distributions (PSDs) of the: (a) calcium aluminate cement, (b) carbonate fillers (limestone, dolomite) and (c) quartz powders used in this study. 28

Figure 9: The area multiplier (AM) as a function of level of CAC replacement by: (a) carbonate fillers and (b) quartz fillers. The symbols represent values corresponding to the mixture formulations evaluated in this study. 30

Figure 10: XRD patterns of CACs pastes prepared at a w/s = 0.60 for: (a) CAC replacement by limestone at a level of 27% (by mass) and (b) CAC replacement by quartz at a level of 24% (by mass). The CAC replacement levels thus selected ensure AM = 2. The blue and red XRD patterns correspond to pure CAC pastes (no filler) prepared at w/s = 0.60 at ages of 8 and 24 hours for comparison. 32

Figure 11: Measured heat evolution profiles for binary paste systems (w/s = 0.60) for (a) AM=1.2 (b) AM=2 and (c) AM=3. (d) Heat evolution profiles of CAC pastes prepared at different w/c. 33

Figure 12: Heat release curves for CAC mixtures for: (a) 27% replacement of CAC and (b) 38.5% replacement of CAC, by limestone and quartz fillers. The reference designates a cementitious blend containing no filler agents, i.e., pure CAC for w/s = 0.60..... 34

Figure 13: The actual w/c of the mixtures determined by correcting for the effects of bleeding, as a function of the design w/c for: (a) carbonate fillers and b) quartz fillers. 35

Figure 14: The correlation between the calorimetric parameters and the actual w/c (determined by discounting water loss due to bleeding) for: (a) heat flow at peak, (b) slope in the acceleration regime, (c) inverse of time to main peak. The solid lines show a best fit line to the dataset while the dashed lines represent a ±10% bound to the best fit line. 36

Figure 15: The correlation between the area multiplier (AM) and: (a) heat flow at peak, (b) slope of the acceleration regime, (c) inverse of time to main peak. The solid lines show a best fit line to the data set while the dashed lines represent a ±10% bound to the best fit line. 37

Figure 16: A comparison of representative measured versus BNG simulated heat evolution profiles for a range of CAC mixtures. The % value denotes the mass-based replacement level of the CAC by a mineral filler..... 40

Figure 17: (a) A comparison of the simulation parameter, t_0 as a function of t_{peak} (time to the main peak) extracted from measured heat profiles across all systems. Product nuclei formed per gram of CAC as a function of: (b) the actual w/c and (c) area multiplier (AM). The solid line indicates best fits and the dashed lines indicate ±10% bounds..... 41

Figure 18: The average centroidal solid-to-solid distance calculated for various CAC systems prepared at a w/s = 0.60 with CAC replaced by: (a) carbonate and (b) quartz fillers at replacement levels ranging from 0 to 50% (by mass). The distances are calculated by averaging the distances between the center of a particle with respect to its nearest neighbors, packed within

a three-dimensional virtual cube for an edge length (of the cube) of 1000 µm. (c) A 2D slice of a 3D-microstructure for a system prepared at w/s = 0.60 with 10% of the CAC (red spheres) replaced by dolomite (green). 43

Figure 19: (a) Sulfate-to-alumina (SO_3/Al_2O_3) mass ratio as a function of increasing OPC replacement by a given alumina source, (b) Carbon dioxide equivalent-to-alumina (CO_2/Al_2O_3) mass ratio for the mixtures containing 30% of limestone (dosed by OPC replacement) as a function of increasing OPC replacement by a given alumina source, (c) The cumulative particle size distributions of the powders, and, (d) The compositions of the binders, minus limestone, plotted on a ternary composition diagram (with CaO-SiO_2-Al_2O_3 at the vertices)..... 49

Figure 20: The compressive strength as function of the CF at 90 days, for all the systems studied herein. The dilution line traces the extent of compressive strength reduction that would occur as the OPC content (in terms of mass fraction) was systematically reduced. For the plain OPC formulation, CF = 0.963, given the presence of limestone therein. The error bars shown, indicate the uncertainty in the strength measurements. 57

Figure 21: The normalized portlandite contents for cementitious mixtures with varying levels of OPC replacement by: (a) CAC1 and (b) CAC2. (c and d) Show the normalized portlandite contents for mixtures with 30% limestone dosed by replacement of OPC and varying levels of additional replacement by: (c) CAC1 and (d) CAC2. The portlandite contents were determined by thermogravimetric analysis (TGA/DTG) and normalized by the OPC content of a mixture.. 58

Figure 22: Representative DTG traces for the neat OPC mixture and systems wherein 15% (by mass) of the OPC is replaced by either CAC1 or CAC2, respectively..... 59

Figure 23: Representative XRD patterns for the plain OPC, limestone enriched (30% OPC replacement by limestone) and CAC enriched mixtures composed for limestone deficient and

excess conditions. Here: Hc (hemicarboaluminate), Mc (monocarboaluminate), CH (portlandite), AFt (ettringite) and Hy (hydrogrossular). All enrichments are carried out by replacement of OPC by an aluminous source, and/or limestone. 60

Figure 24: Phase assemblages estimated using GEMS for: (a) 15% CAC1 replacement, (b) 15% CAC1 and additional 30% limestone replacement, (c) 15% CAC2 replacement and (d) 15% CAC2 and additional 30% limestone replacement. All replacements were carried out by reducing the quantity of OPC on a mass basis. Monosulfoaluminate (Ms), ettringite (AFt), monocarboaluminate (Mc), hemicarboaluminate (Hc), strätlingite (C_2ASH_8), hydrogrossular (Hy) and hydrotalcite (M_4AH_{10}) are denoted. The dashed lines locate the estimated phase assemblage after 90 days, based on the degree of CAC reaction as estimated by QXRD. 63

Figure 25: Representative DTG curves of OPC mixtures for: (a) 0-to-15% MET replacement, (b) 0-to-15% MET replacement with additional 30% of limestone dosed by OPC replacement. The normalized (by CF) portlandite contents for OPC mixtures for: (c) 0-to-15% MET replacement, (b) 0-to-15% MET replacement with additional 30% of limestone dosed by OPC replacement. The portlandite contents were determined by thermal analysis (TGA/DTG). All replacements were carried out by reducing the quantity of OPC on a mass basis..... 66

Figure 26: Representative XRD patterns for the plain (100% OPC), limestone enriched (30% OPC replacement by limestone) and MET enriched mixtures composed for limestone deficient and excess conditions. Here: Hc (hemicarboaluminate), Mc (monocarboaluminate), CH (portlandite), AFt (ettringite) and Hy (hydrogrossular). All enrichments are carried out by replacement of OPC. 67

Figure 27: Phase assemblages estimated using GEMS by incremental reaction of MET for: (a) 15% MET and (b) 15% MET and additional 30% limestone replacement of OPC after 90 days of

hydration. Monosulfoaluminate (Ms), ettringite (AFt), monocarboaluminate (Mc), hemicarboaluminate (Hc), strätlingite (C_2ASH_8), and hydrotalcite (M_4AH_{10}) are denoted. The dashed lines locate the estimated phase assemblage and MET degree of hydration, after 90 days, based on the portlandite match-point from TGA data as discussed in the text..... 68

Figure 28: Representative DTG curves for OPC mixtures for: (a) 0-15% HA replacement, (b) 0-15% HA replacement with additional 30% of limestone dosed by OPC replacement. The normalized (by CF) portlandite contents for OPC mixtures for: (c) 0-15% HA replacement, (d) 0-15% HA replacement with additional 30% of limestone dosed by OPC replacement. The portlandite contents were determined by thermal analysis (TGA/DTG). All replacements were carried out by reducing the quantity of OPC, by HA and/or limestone, on a mass basis..... 70

Figure 29: Representative XRD patterns for the plain (100% OPC), limestone enriched (30% OPC replacement by limestone) and HA enriched mixtures composed for limestone deficient and excess conditions. Here: Hc (hemicarboaluminate), Mc (monocarboaluminate), CH (portlandite), AFt (ettringite) and Hy (hydrogrossular). All enrichments are carried out by replacement of OPC by HA and/or limestone, by mass. 71

Figure 30: Phase assemblages estimated using GEMS by incremental reaction of HA for: (a) 15% MET and (b) 15%MET and additional 30% limestone replacement of OPC after 90 days of hydration. Monosulfoaluminate (Ms), ettringite (AFt), monocarboaluminate (Mc), hemicarboaluminate (Hc), strätlingite (C_2ASH_8), Hydrogrossular (Hy) and hydrotalcite (M_4AH_{10}) are denoted. The dashed lines locate the estimated phase assemblage and MET degree of hydration, after 90 days, based on the portlandite match-point from TGA data as discussed in the text..... 73

Figure 31: (a) Calculated strength-porosity trends for cementitious blends containing HA or MET at 28 and 90 days of hydration and (b) The strength as a function of the C-S-H volume fraction for all the cementitious blends considered in this study. 75

Figure 32: The quantity of limestone consumed as a percentage of the initial quantity of limestone present (mass basis) in excess limestone systems as evaluated using thermogravimetric analysis for the range of aluminous sources considered in this study. 77

Figure 33: (a) Carbon dioxide equivalent-to-aluminum oxide ($CO_{2\text{-}eq}/Al_2O_3$), (b) calcium-to-aluminum oxide (CaO/Al_2O_3), and, (c) carbon dioxide equivalent-to-calcium oxide ($CO_{2\text{-}eq}/CaO$) mass ratios as a function of the CAC replacement level for each carbonate source. (d) The particle size distributions (PSDs) of the solid reactants used in this study. 83

Figure 34: The compressive strength of CAC pastes: (a) As a function of age for various levels of CAC replacement by limestone and (b) After 90 days of hydration as a function of the CAC mass fraction in the binder. For all the mixtures illustrated in the figure, w/s = 0.45. 88

Figure 35: Representative XRD patterns for the hydrated blends wherein 10 mass % of CAC has been replaced by limestone for blends prepared at: (a) w/s = 0.40, (b) w/s = 0.45 and (c) w/s = 0.70. In all plots, Mc denotes the monocarboaluminate phase ($Ca_4Al_2(CO_3)(OH)_{12}\cdot 5H_2O$). 90

Figure 36: The residual $CaCO_3$ content quantified using thermal analysis (TGA/DTG) in CAC-limestone blends wherein 10 mass % of the CAC was replaced by limestone at different w/s. .. 90

Figure 37: Representative XRD patterns of the hydrated CAC-Na_2CO_3 blends for: (a) w/s = 0.40, 10% Na_2CO_3, (b) w/s = 0.70, 10% Na_2CO_3 and (c) w/s = 0.70, 30% Na_2CO_3. In all plots, G: gaylussite ($Na_2Ca(CO_3)_2\cdot 5H_2O$), Th: thermonatrite ($Na_2CO_3\cdot H_2O$), Mc: monocarboaluminate ($Ca_4Al_2(CO_3)(OH)_{12}\cdot 5H_2O$), and Hc: hemicarboaluminate ($Ca_4Al_2(CO_3)_{0.5}(OH)_{13}\cdot 5.5H_2O$). 93

Figure 38: Representative DTG traces for the hydrated CAC-Na_2CO_3 blends for: (a) w/s = 0.40, 10% Na_2CO_3, (b) w/s = 0.70, 10% Na_2CO_3 and (c) w/s = 0.70, 30% Na_2CO_3. In all plots, G: gaylussite ($Na_2Ca(CO_3)_2{\cdot}5H_2O$), Th: thermonatrite ($Na_2CO_3{\cdot}H_2O$), Mc: monocarboaluminate ($Ca_4Al_2(CO_3)(OH)_{12}{\cdot}5H_2O$), and Hc: hemicarboaluminate ($Ca_4Al_2(CO_3)_{0.5}(OH)_{13}{\cdot}5.5H_2O$). 93

Figure 39: The volumetric phase assemblage calculated to exist when 10 mass % CAC has been replaced by limestone ($CaCO_3$) for: (a) w/s = 0.40 and (b) w/s = 0.70. In these plots: Mc: monocarboaluminate ($Ca_4Al_2(CO_3)(OH)_{12}{\cdot}5H_2O$) and M_4AH_{10}: OH-hydrotalcite. 95

Figure 40: The volumetric phase assemblage calculated to exist for w/s = 0.70 when CAC has been replaced by Na_2CO_3 at the level of (by mass): (a) 10 mass % and (b) 30 mass %. In these plots: G: gaylussite ($Na_2Ca(CO_3)_2{\cdot}5H_2O$), Mc: monocarboaluminate ($Ca_4Al_2(CO_3)(OH)_{12}{\cdot}5H_2O$) and M_4AH_{10}: OH-hydrotalcite. 96

Figure 41: The volumetric phase assemblage calculated to exist for w/s = 0.70 when 30 mass % of the CAC has been replaced by a combination of: (a) CaO and $CaCO_3$ and (b) CaO and Na_2CO_3. In these plots: G: gaylussite ($Na_2Ca(CO_3)_2{\cdot}5H_2O$), Mc: monocarboaluminate ($Ca_4Al_2(CO_3)(OH)_{12}{\cdot}5H_2O$) and M_4AH_{10}: OH-hydrotalcite. 98

Figure 42: (a) The layered structure of $3CaO{\cdot}Al_2O_3{\cdot}Ca(NO_3)_2{\cdot}10H_2O$ (i.e., NO_3-AFm) refined by Renaudin et al [] showing the locations of [AlO_6], [CaO_7] polyhedral, charge compensating anions (NO_3^-), bound (OW1) and free water (OW2). The projection of the crystal structure is shown along the [110] plane, and, **(b)** The particle size distributions of the as-synthesized $Ca_3Al_2O_6$ and the NO_3-AFm powders. 105

Figure 43: The volumetric distributions of AFm phases at 25 °C obtained via a progressive equilibrium simulation for: **(a)** NO_3-AFm exposed to Cl^- solutions (i.e., in direction of preferred ion-exchange, see Equation 1), and, **(b)** Cl-AFm exposed to NO_3^- solutions (i.e., in direction of

non-preferred ion-exchange, see Equation 1). The dashed lines show the concentrations of ions (C_0) initially present in the exchange solution in the experimental studies that follow. 108

Figure 44: Representative Cl^- concentration evolutions as a function of time for NO_3-AFm undergoing ion-exchange under static and convective (stirred) mixing conditions for an initial Cl^- concentration of 0.1 mol/L at: **(a)** 5 ˚C, and, **(b)** 45 ˚C. Also shown are the initial (C_0) and final (C_f) concentrations of Cl^- ions that persist when ion-exchange begins, and completes. 110

Figure 45: (a) Representative NO_3^- ion concentrations as a function of time for convectively mixed NO_3-AFm systems undergoing ion-exchange (i.e., that are taking up Cl^- species) at 25 ˚C for initial chloride concentrations (C_0) of 0.01 mol/L, 0.1 mol/L and 1 mol/L. **(b)** An illustration of the stoichiometry of the NO_3-AFm ion-exchange reaction (see Equation 1) which illustrates that, as expected, per unit of Cl^- uptake into the AFm structure, a unit of NO_3^- species is released into the solution..... 111

Figure 46: Representative evolutions of Cl^- ion concentrations as a function of time for NO_3-AFm systems undergoing ion-exchange in solutions having an initial Cl^- concentration of 0.1 mol/L under stirred conditions at: **(a)** 5 ˚C, **(b)** 25 ˚C and **(c)** 45 ˚C. The experimental data is fitted by a first-order reaction equation of the form: $Ct = Cf + (C0 - Cf)e - kt$ where, C is the concentration (mol/L), t denotes time (seconds), k is the reaction rate constant (s^{-1}) and the subscripts ‘0’ and ‘f’ indicate the initial and final ion concentrations, respectively. 112

Figure 47: (a) The reaction rate constant as a function of the initial Cl^- concentration at 25°C. **(b)** The reaction rate constant as a function of temperature for NO_3-AFm systems transforming to Cl-AFm (via ion-exchange) in solutions with an initial Cl^- concentration (C_0) of 0.1 mol/L under static and convectively mixed conditions. The data are fitted by exponential functions of the form: y = Aexp(Bx) where A and B are numerical coefficients. The data corresponding to static

and convectively mixed solution conditions are separated by a constant "y-offset". **(c)** An Arrhenius plot showing the natural logarithm of the reaction rate constant (k, s^{-1}) as a function of the inverse temperature for AFm systems undergoing ion-exchange in both in the forward (NO_3-to-Cl AFm) and reverse (Cl-to-NO_3 AFm) directions. 116

Figure 48: Representative comparisons of measured and calculated concentration profiles for ion-exchange in the forward direction (i.e., NO_3-AFm converting to Cl-AFm) for different combinations of reaction temperature and C_0: **(a)** C_0 = 0.1 mol/L Cl^-, T = 25°C, **(b)** C_0 = 0.1 mol/L Cl^-, T = 45°C, and, **(c)** C_0 = 1 mol/L Cl^-, T = 25°C. 118

Figure 49: (a) Representative XRD reflections of the AFm solids following ion-exchange under convective mixing, for an initial concentration of the Cl^- solution (C_0) of 0.1 mol/L at T= 5 ˚C, 25 ˚C and 45 ˚C. **(b)** Representative XRD reflections of the AFm solids following ion-exchange for C_0 = 0.01 mol/L, 0.1 mol/L and 1 mol/L at T= 25 ˚C under static conditions. The XRD pattern for the NO_3-AFm precursor is shown for reference. 120

Figure 50: (a) Representative XRD reflections of the AFm solids following ion exchange for an initial concentration of the NO_3^- solution of 0.1 mol/L at 5 ˚C and 45 ˚C under convective mixing conditions. The XRD pattern of the Cl-AFm precursor is shown for reference. All data shown corresponds to "reverse direction" ion exchange reactions. **(b)** A schematic of the ion-exchange pathway for the thermodynamically preferred ("forward") and non-preferred ("reverse") directions showing the formation of a solid-solution as an intermediate step in the "reverse" direction of ion-exchange. 122

Figure 51: (a) A Lippmann diagram showing solidus and solutus traces for a solid-solution with end-members comprising NO_3-AFm (Pole 0) and Cl-AFm (Pole 1). **(b)** The Gibbs energy of ideal mixing (ΔG_{id}), excess Gibbs energy of mixing (ΔG_{ex}) and the molar Gibbs energy of

mixing (ΔG_M) calculated using Equation (5) for the two component system comprising NO_3-AFm and Cl-AFm are shown. 123

Figure 52: Schematic representation of ion exchange reaction in the (a) forward and (b) reverse directions. 131

VITA

2007	B.S., Civil Engineering Univerisdad Nacional de Colombia Bogota, Colombia
2010-2012	Teaching/Research Assistant University of Wisconsin-Milwaukee Milwaukee, Wisconsin
2012	M.S., Civil Engineering University of Wisconsin-Milwaukee Milwaukee, Wisconsin
2012-2016	Teaching/Research Assistant University of California, Los Angeles Los Angeles, California

Selected Publications and Presentations

- **Puerta-Falla, Guillermo**, Aditya Kumar, Lauren Gomez-Zamorano, Mathieu Bauchy, Narayanan Neithalath, and Gaurav Sant. "The influence of filler type and surface area on the hydration rates of calcium aluminate cement." Construction and Building Materials 96 (2015): 657-665.
- **Puerta-Falla, Guillermo**, Magdalena Balonis, Gwenn Le Saout, Aditya Kumar, Melanie Rivera, Gabriel Falzone, Narayanan Neithalath, and Gaurav Sant. "The influence of slightly and highly soluble carbonate salts on phase relations in hydrated calcium aluminate cements." Journal of Materials Science: 1-13.
- Kumar, Aditya, Tandre Oey, **Guillermo Puerta Falla**, Ryan Henkensiefken, Narayanan Neithalath, and Gaurav Sant. "A comparison of intergrinding and blending limestone on reaction and strength evolution in cementitious materials." Construction and Building Materials 43 (2013): 428-435.
- **Puerta-Falla, Guillermo**, Magdalena Balonis, Gwenn Le Saout, Gabriel Falzone, Carolyn Zhang, Narayanan Neithalath, and Gaurav Sant. "Elucidating the Role of the Aluminous Source on Limestone Reactivity in Cementitious Materials." Journal of the American Ceramic Society 98 (2015): 4076-4089.
- **Puerta-Falla, Guillermo**, Magdalena Balonis, Gwenn Le Saout, Narayanan Neithalath, and Gaurav Sant. "The Influence of Metakaolin on Limestone Reactivity in Cementitious Materials." In Calcined Clays for Sustainable Concrete, pp. 11-19. Springer Netherlands, 2015.
- **Puerta-Falla, Guillermo**, Narayanan Neithalath, Aditya Kumar, Lauren Gomez-Zamorano, Mathieu Bauchy, Gaurav Sant. “The influence of filler type and surface area on the hydration rates of calcium aluminate cement." ACI Fall Convention, November 8-12, 2015, Denver, Colorado, USA.

Chapter 1: Introduction

1.1 Scope and Objectives

Ordinary portland cement production accounts for at least 5% of global CO_2 emissions [1,2]. As the principal component in concrete formulations in addition to the expansion, modernization and retrofitting of infrastructure in developed and developing countries, the share of greenhouse emissions is certain to expand [3,4]. This environmental burden has brought questions with regard to cement as a sustainable material in the coming decades. The use of low-clinker factor cements has been thought as a means to a reduced CO_2 footprint material, one way of achieving this is through the use of secondary cementitious materials (SCM's) with pozzolanic properties (i.e., fly ash, furnace slag, silica fume, metakaolin, etc…), these materials have been widely used to reduce cement fractions while maintaining, sometimes even improving, mechanical properties of binders [5,6]. However, availability of SCM's, particularly a local scales, as well as durability related problems (i.e, carbonation, reinforcement corrosion, etc…) have hindered the increase of SCM's use in cement [7,8]. An attractive alternative is the use of limestone (calcite, $CaCO_3$) as part of the binder formulation with or without SCM's [9,10,11,12], while part of cement production as raw material and also present in commercially available cements, limestone fractions remain limited to 15% [13] in the United States due to detrimental effects on durability and mechanical properties mainly due to dilution.

In addition to dilution, addition and/or replacement of cement by limestone, also induces other effects such as accelerated hydration at early ages (resulting from the so-called "filler effect") [14,15,16,17], as well as changes in particle packing and microstructure of the system when limestone and cement have different particle sizes [11,18]. It is important to notice that these acceleratory effects on early age hydration have also been considered to be a result of larger

water availability for cement hydration as an inert (or almost inert) powdered material replaces OPC. Bentz [19] showed that the degree of hydration observed in OPC is in close relation to the volume fraction of the "water filled" porosity, this implies that in cases of OPC replacement by an inert filler such as limestone, the increase in OPC hydration can be attributed to the net increase in water-to-cement ratio. However, Oey et al [17] through the use of isothermal calorimetry showed that heat of hydration (per mass of cement in the system) is not a function of the water-to-cement ratio and hence, the acceleratory effects are a related to filler size and level of replacement. This acceleratory effect has limitations as filler sizes get smaller (less than 3μm) agglomeration occurs reducing surface area provided and degree of hydration of the OPC fraction. Furthermore, the authors also showed that the filler's material properties (i.e., surface energy, reactivity, etc...) are also important with limestone being more efficient than quartz at increasing OPC hydration under equal replacement level and size conditions. In the case of CAC systems, the acceleratory effects produced by finely powdered fillers have not yet been measured, this in part due to the complexities associated with the water and temperature dependency of the hydration products (CAH_{10}, C_2AH_8 and C_3AH_6) [20].

Other studies have shown that, although very limited, limestone partakes in OPC hydration reactions inducing chemical changes as the formation of calcium carboaluminate phases and stabilization of ettringite [14,21]. Calcium carboaluminate formation is an interesting outcome as aluminate species, from aluminate phases in the clinker, react with water and limestone to produce a solid phase. This implies that the binder chemistry could, in theory, be manipulated to boost calcium carboaluminate phase formation while reducing the amount of free water in the system, such combined effect would increase the solid fraction of the system reducing dilution and allowing for an extended amount of limestone without detrimental repercussions to

mechanical properties. In the particular case of CAC systems, limestone additions have been studied for endodontic [22] applications and carbon dioxide sequestration [23] with formation of calcium carboaluminate phases being observed [22]. Formation of a calcium carboaluminate, in the case of CAC systems, is also interesting as it can provide stability to the hydrates and prevent the problematic conversion of metastable hydrates (CAH_{10} and C_2AH_8) into hydrogarnet (C_3AH_6) [20].

Based on the potential beneficial outcomes of extended limestone additions in OPC and CAC systems, it is important to note that some detrimental effects can also be present. One of these is the system's performance at high temperatures (T>38˚C) as stability of calcium carboaluminate phases is compromised in favor of calcite and monosulfoaluminate [24]. Furthermore, interactions between CO_3^{2-} (from limestone) and SO_4^{2-} (from gypsum or sulfate attack) can produce formation of thaumasite in OPC systems with detrimental effects due to expansion, Lothenbach et al [25] showed that even though thaumasite is thermodynamically stable at 20˚C, significant formation of this phase only occurs at low temperatures and is preceded by delayed ettringite formation. These detrimental effects of limestone in OPC systems at low temperatures also include brucite formation and consumption of C-S-H [26], the latter is especially problematic as C-S-H is directly linked to mechanical performance.

This research intends to provide new insights into the possibilities of extended limestone replacement in both calcium aluminate and ordinary portland cements (CAC and OPC respectively). The effects of limestone on hydration rates as well as its chemical/mineralogical implications are analyzed to further increase the use of limestone in cementitious systems.

Limitations are also studied to better understand the factors controlling chemical and physical interactions between each of the cements studied and the limestone addition.

1.2 Organization

This document is divided into 8 main chapters, the current chapter (1) serves as an introduction and explains the motivations for the research work. Chapter 2 explores the physical effects that limestone induces in ordinary Portland cement (OPC) systems and elucidates on the differences between interground and limestone blended cementitious systems, through the use of isothermal calorimetry and boundary nucleation and growth (BNG) models it is shown that increases in surface area can induce higher early age hydration rates.

Chapter 3 explores the physical effects of limestone in calcium aluminate cement (CAC) systems, this work was carried out as a comparison to effects in OPC as the nature of these systems (i.e., composition, stability and crystallinity of hydration products, etc…) varies dramatically. By the use of isothermal calorimetry and BNG models, it was found that an increase in surface area does increase the hydration rates of CAC systems. However, clear differences with respect to OPC systems were found: i) the nature (surface properties) of the filler appear not to play a role and ii) the water content of the systems does increase hydration rates. The former difference is remarkable as quartz and limestone fillers, provided both induce the same level of area availability is the system, appear to favor higher hydration rates with limestone being more favorable that quartz in OPC systems, this is not the case in CAC systems where both fillers appear to favor higher early hydration rates in a similar magnitude. The second difference between OPC and CAC systems has to do with the left shift peak in the heat evolution

when a higher water content is allowed in the systems. While this this left shift in the heat evolution is clear in the CAC systems, it is absent in the OPC ones.

Chapter 4 serves as an attempt to induce higher limestone partake in hydration reactions. Since limestone remains mainly inert in OPC systems with limited formation of calcium carboaluminate phases (monocarboaluminate-Mc and hemicarboaluminate-Hc), it is hypothesized that an artificial increase in the alumina content of the OPC system (given the low amount of C3A present in OPC) can bring a larger extend of carboaluminate formation with is related water consumption. Such approach would render limestone as a participant of hydration reactions with a reduced dilutive effect when large limestone mass fractions are used. By the used of 4 different alumina sources (calcined alumina, metakaolin and two different calcium aluminate cements) at 3 different mass fractions (5, 10, 15%), used in systems with large limestone mas fractions (30%), it is shown that limestone partake in reactions can be enhanced. This enhancement in calcium carboaluminate phase formation and reduction of calcite as hydration times increase, as detected from x-ray diffraction and TGA, is larger for the calcined alumina, however, mechanical properties of those systems are not fully compensate for dilutive effects. It is concluded that metakaolin is the best alumina source in light of the mechanical properties displayed although this “improved mechanical properties” are only on account of the pozzolanic nature of metakaolin and not on limestone activation. From the research work carried out in chapter 4, it was concluded that the limited enhancement in calcium carboaluminate phase formation (limestone activation) could be on account of one or a combination of two factors; i) low solubility and slow dissolution rate of limestone and/or ii) kinetic restrains in the ion exchange reactions taking place at the AFm phase interlayer.

Chapter 5 addresses the first of the two possible factors that were brought up in chapter 4 by studying the influence of a highly soluble carbonate salt (Na_2CO_3) in CAC systems, results are also compared with the effects produce by limestone. While the use of a highly soluble carbonate salt allows a larger amount of CO_3^{2-} species in solution, and hypothetically a larger extend of calcium carboaluminate phase formation, this was not observed. By replacing the cement fraction by Na_2CO_3, the high availability of $CO_3$2- species is also accompanied by large Na^+ concentrations, this combination leads to the formation of compounds with larger sodium and carbon content (i.e., gaylussite and thermonitrtate). Formation of these new compounds introduce for competition CO_3^{2-} species available which in turn suppressed carboaluminate phase formation. Moreover, it was found that any calcium carboaluminate phase formed becomes unstable over time leading to additional formation of sodium-carbonate compounds. This effect was surprising as carboaluminate phases, upon formation, are stable in normal cementitious systems. This instability appears to be on account of either low water availability or low water activity. Low water availability is a result of high water intake of the sodium-carbonate compounds formed in these systems (gaylussite and thermonitrate) while low water activity is a result of the high concentrations present in solution due to the high solubility of the carbonate salt. These results bring the question of calcium carboaluminate stability as a function of not only of temperature and ionic availability but also as a function of water activity.

Chapter 6 presents the results of research carried out to study the kinetics of ion exchange in AFm phases, this in order to determine if calcium carboaluminate formation is kinetically restrained, as proposed at the end of chapter 4, as a result of limited ion exchange (not availability of anionic species in solution). By the use of pure NO_3-AFm and Cl-AFm, ion exchange reactions were induced at three different temperatures (5, 25 and 45˚C) and three

different ionic concentrations (0.01, 0.1 and 1 mol/l) under two different regimes (diffusive and convective). NO_3-AFm conversion into Cl-AFm was accomplished through the use of $CaCl_2$ solutions while Cl-AFm conversion into NO_3-AFm was accomplished thought $Ca(NO_3)_2$ solutions. It is concluded, from these experimental results, that ion exchange reaction kinetics is a function of anion availability in solution and temperature. The transport regime also appears to play a relevant role where convective conditions appear to enhance rates of exchange as compared to purely diffusive cases. From the research program presented in chapters 5 and 6, it can be conclude, with a high level of confidence, that it is the low solubility and slow dissolution rate of limestone what limits the formation of calcium carboaluminate phases in cementitious systems.

Chapter 7 of this document presents the general conclusions of this research program based on the experimental and computational results obtained.

Chapter 8 presents a proposal for future research topics related to calcium carboaluminate phases and ion exchange reactions in AFm. Some of the most interesting and attractive areas are the stability of calcium carboaluminate phases as a function of water activity, the effect of other anion species (other than NO_3^- and Cl^-) on ion exchange reactions at different temperature, concentration and transport conditions, in particular the effect of different anionic charge (from monovalent to divalent and vice versa) in ion exchange kinetics. Mechanical properties of the alumina doped limestone-OPC systems (i.e., compressive strength and modulus of elasticity), this as the volumetric fractions of carboaluminate are higher than in normal limestone-OPC formulations. Capacity of calcium-magnesium hydrotalcites (different LDH as compared to the calcium-alumino compounds “AFm” studied herein) to intake carbonate ions. The latter is

particularly attractive as it appears that OH-hydrotalcite can be one of the more stable compounds (as compared to the Cl-hydrotalcite) which appears to be contrary to findings in AFm phases. The expansive properties of NO_3-AFm as a function of water intake as a possible application for late water release or shrinkage mitigation in cement pastes. Each of these topics are developed in more detail in chapter 8 with the help of corresponding references.

The last section of this document presents the references.

Chapter 2: A Comparison of Intergrinding and Blending Limestone on Reaction and Strength Evolution in Cementitious Materials.

2.1 Scope of Chapter 2

Cement replacement by limestone can be achieved by either: (1) intergrinding cement clinker and limestone through the cement production process [27,28] or (2) blending the cement and graded limestone powders through the concrete batching-mixing process. It should be noted that in the case of commercially produced interground formulations, performance similarity to pure OPC formulations is achieved by over-grinding the clinker and the limestone. Thus, such interground binders are essentially a composition of a fine cement and a (finer) limestone- as the limestone, being a softer phase than the clinker, grinds to a finer particle size [29,30].

While both means of cement replacement (i.e., intergrinding or blending) appear equivalent, it is unclear if similar rates and extents of reaction and property development can be achieved by both means, so long as the clinker composition and surface areas (fineness) of the solid phases are similar. This aspect is important to understand, if from an industrial concrete proportioning perspective, limestone blended formulations can be constituted to display performance similar to interground limestone cements. To understand these aspects of limestone replacement and binder fineness in more detail, this chapter evaluates interground and blended limestone binders to understand if there exists a means to establish reaction and property (strength) equivalence between these materials.

2.2 Materials, Mixing Procedures and Methods

Three commercially available cements were used in this study. The phase composition of the cements is provided in Table 1. The limestone powders used are (nominally pure) commercially

available, particle size classified products produced by OMYA A.G. Particle size distributions (PSD, Figure 1) of the solids were measured using static light scattering using isopropanol and sonication for dispersing the powders to primary particles [31]. The uncertainty in the scattering measurements was determined to be around 6% based on measurements performed on six replicate powder samples assuming the density of the cement and limestone to be 3150 kg/m^3 and 2700 kg/m^3 respe9ctively.

Table 1: The estimated phase compositions of the cements used in this study

ID	Phase	Mass %	ID	Phase	Mass %	ID	Phase	Mass %
OPC I/II	C_3S	59.1	OPC-L	C_3S	63.6	OPC III	C_3S	63.3
	C_2S	15.9		C_2S	8.9		C_2S	10.3
	C_3A	3.7		C_3A	7.1		C_3A	3.9
	C_4AF	10.8		C_4AF	9.5		C_4AF	14.2
	Na_2O (eq)	0.40		Na_2O (eq)	0.70		Na_2O (eq)	0.50
	Limestone	≈ 0-5%		Limestone	≈ 6-15%		Limestone	≈ 0-5%

Cementitious paste mixtures were prepared using de-ionized (DI) water at a fixed water-to-solids ratio (*w/s* = 0.45) as described in ASTM C305 [13]. It should be noted that in the case of blended mixtures, the dry cement and limestone powders were homogenized, prior to mixing in a planetary mixer. To understand the role of the limestone introduction mode (intergrinding or blending) and limestone fineness, for the Type I/II and Type III cements, the cement content was reduced by the maximum permissible limit; to permit 15% (mass) replacement of cement, by limestone powders of varying particle sizes while the interground cement (i.e., designated OPC-L), was evaluated as supplied. Further experiments were performed by composing blended binders where the OPC fraction (85%, by mass) was constituted as a 50:50 (mass) blend of Type I/II and Type III OPCs, to achieve a cement fineness midway between the individual OPC types,

while the residual mass fraction consisted of limestone powders of varying fineness, added to achieve a 15% (by mass) cement replacement level [32].

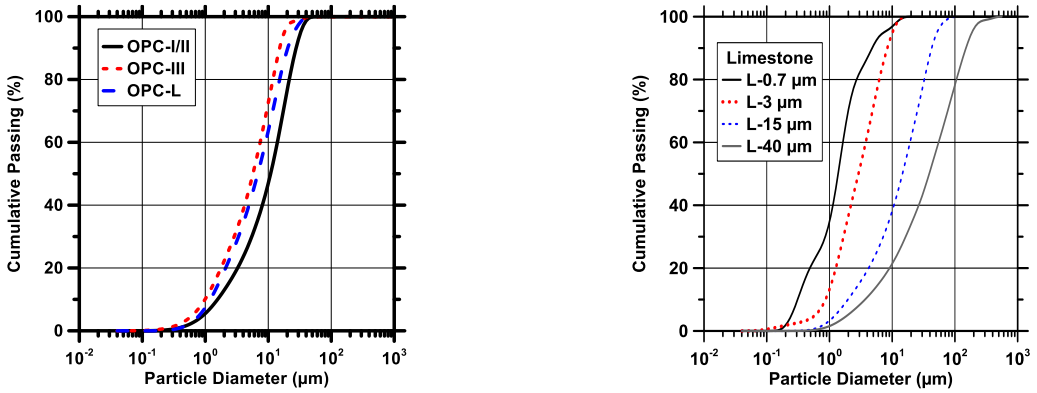

(a) (b)

Figure 1: Particle size distributions for (a) cement and (b) limestone used in this study.

The influence of limestone additions (i.e., cement replacement) on the solid surface area of the system is described using an area multiplier (AM, unitless) as shown in Equation (1):

$$AM = \frac{100 + \frac{(r.SSA_F) + ((100 - r).SSA_C)}{((100 - r).SSA_c)}}{100} \qquad \text{(equation 1)}$$

where: r (mass %) is the percentage replacement of cement by limestone filler and SSA_C and SSA_F (m^2/g) are the specific surface areas of the cement and limestone respectively - calculated using the particle size distribution of the powder materials, while assuming spherical particles. It should be noted that solid particle surface areas calculated within this approximation are likely underestimated by a factor of 1.6-1.8, given the angular nature of the cement and limestone particles [33]. Thus, the AM is a scaling factor that describes the relative change in the solid surface area induced by filler addition in comparison to the surface area provided by a unit mass (1 g) of cement (reactant). In other words, AM is the surface area of filler per unit surface area of

cement in the system. The greater this quantity, either because the limestone is finer or because it is present in greater amounts, the more AM will exceed unity. It should be noted that the calculation of the AM is subject to uncertainties that stem from measurements of particle size distributions and the assumptions of spherical particle shape. Calculated specific surface area (SSA) and d_{50} values for the powders used in this research are provided in table 2.

The influence of cement replacement on the rates of reactions was tracked using isothermal conduction calorimetry. The thermal power and energy measured were then used to assess the influence of powder additions on the reaction kinetics and the cumulative heat release of the cement paste.

The compressive strength of cubic (50 mm x 50 mm x 50 mm) specimens cured at 25 ± 1°C, in a sealed condition was measured as described in ASTM C109 at 1, 3, 7 and 28 days for all the mixtures with the exception of the Type III plain cement paste and the 15 μm, 15% limestone containing Type III (blended) paste for which datasets are available at 1, 3 and 7 days and 1 day respectively [13]. Also, it should be noted that strength determinations were not carried out for the 50:50 OPC blend mentioned above, which was evaluated only in terms of its reaction rate behavior. The compressive strength reported is typically the average of three specimens cast from the same mixing batch. The coefficient of variation (CoV) in the measured strength was determined to be around 10% for samples cast from the same batch.

Table 2: Measured d_{50} and calculated specific surface area (SSA) values for the cement and limestone powders, as determined using static light scattering (Figure 1).					
Cement ID	**ASTM C150 OPC**		**Size Classified Limestone**		
	d_{50} (µm)	**SSA_C (m^2/kg)**	**Limestone ID**	**d_{50} (µm)**	**SSA_F (m^2/kg)**
Type I/II	9.83	486.00	L-0.7 µm	1.40	2592.10
OPC-L	6.76	601.50	L-3 µm	2.98	1353.20
Type III	5.61	780.27	L-15 µm	14.87	399.20
Type I/II & III (50:50)	~	633.14	L-40 µm	40.10	228.60

2.3 Experimental Results and Discussion

Figure 2 shows the influence of cement type (i.e., fineness) and limestone particle size on the rate of hydration reactions. It is noted that, in general, an increase in the cement fineness, limestone fineness, or cement replacement level acts to increase the rate of chemical reactions. This increase (i.e., acceleration) manifests as a left-shift of the heat flow curve and elevation in the heat flow value at the main peak [17,14,34]. While this effect is somewhat influenced by the chemistry of the mineral filler and its interfacial/compositional properties – this response is as expected, as an increase in the fineness of the cement and/or the limestone, would increase the surface area available for reactions, resulting in an acceleration in hydration [17,34].

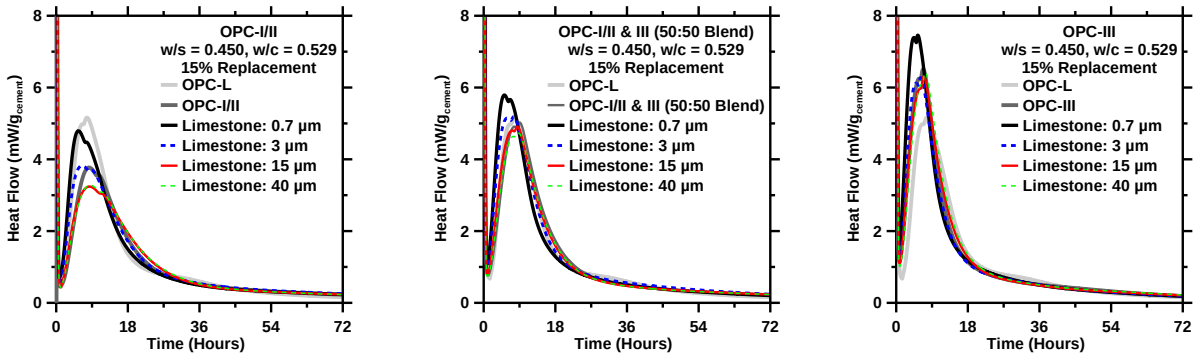

(a) (b) (c)

Figure 2: Representative graphs showing reaction rates as measured using isothermal calorimetry to highlight the influence of intergrinding and post-blending for: (a) Type I/II OPC, and (b) 50:50 blend of Type III and Type I/II OPC and (c) Type III OPC.

To better quantify the acceleration in binder hydration due to limestone additions, calorimetric parameters including: (a) the slope during the acceleration period, (b) the heat flow at the main peak and (c) the inverse of time needed to achieve the heat peak are plotted as a function of the AM (Figure 3) [[34]]. The trends indicate that rates of reactions are enhanced in proportion with the AM of the system (i.e., a function of the cement and limestone fineness). Thus, the reaction rates of the 50:50 OPC blends and the OPC-L mixtures lie intermediate between the reaction response of the Type I/II (lowest surface area) and Type III (highest surface area) OPCs, for mixtures prepared at equivalent dilution (*w/s*). While these results do suggest that an ever progressive increase in the AM will amplify the reaction rate, this is an effect of diminishing returns. For example: as is clarified by Figure 3, indeed increasing the AM, does act to increase reaction rates, but this effect is applicable only up to AM $\leq$ 4 after which no further acceleration in reactions is noted. This limiting role of the AM on the reaction rate (parameters) does likely result from: (1) the enhanced agglomeration of fine solid particles, which would act to reduce their exposed surface area and trap water in flocs inducing a less than expected acceleration in reactions and/or (2) a surface area saturation effect, wherein for AM $\geq$ 4, the available surface

area is more than that is needed for reaction of the available quantity of cement, resulting in a plateau in the measured reaction parameters [17,34].

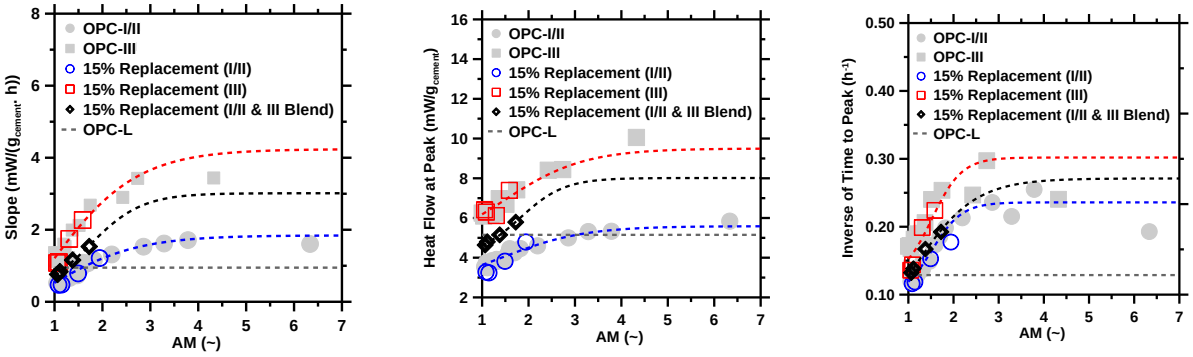

Figure 3: Calorimetric parameters and best fit lines (dashed lines) as a function of the area multiplier for: (a) slope during the acceleration period, (b) heat flow value at the main heat peak and (c) inverse of time required to achieve the main heat peak. The solid points are adapted from [34] and the open symbols represent mixtures with 15% blended limestone. The solid line indicates the calorimetric parameter value for the interground OPC-L cement.

To examine the influence of the limestone addition mode, i.e., intergrinding or blending on the mechanical properties, compressive strength determinations were carried out. It is noted that the plain cement pastes, (i.e., *w/c* = 0.45), for both the Type I/II and Type III OPCs show the best strength behavior, being around 10% stronger than the limestone containing mixtures [29]. The exception is at 1 day, when the OPC-L mixture develops a *very slightly* higher strength than the Type I paste (Figure 4a). For all the limestone mixtures, unsurprisingly and in accordance with the reaction evolution trends, the compressive strength at 1 day was noted to scale as shown in Figure 4(a) wherein: Type III > OPC-L > Type I/II, as linked to the fineness of the cement and the limestone contained in each formulation. However, by later ages (i.e., 28 days), it is noted that all limestone containing pastes show compressive strengths that are similar to each other (Figure 4b and 4c). It should be noted however, that this study does not consider any differences in microstructural packing that may manifest, as the particle size of the limestone is changed.

Early-age strength evolves in relation to the binder fineness, with the Type III mixtures showing higher early age strengths than similarly constituted Type I/II OPC systems, and the OPC-L system showing intermediate strengths. These results suggest that in blending operations, the partial or complete use of a fine cement would be a viable means to achieve elevated early strengths [32].

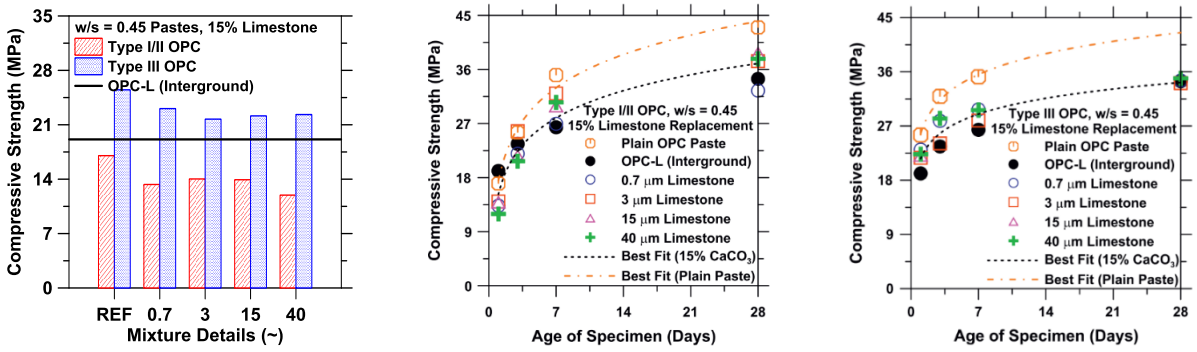

(a) (b) (c)

Figure 4: The evolution of compressive strength in interground and blended limestone (paste) systems for a variety of limestone particle sizes, for two cement types over: (a) the first day and (b and c) over the first 28 days of hydration. Except the plain cement pastes (marked REF), these systems were constituted at w/s = 0.450, equivalent to w/c = 0.529 for all mixtures.

The evolution of the compressive strength has been shown to be linearly related to the release of heat through hydration [34,35,36]. It should be noted that the measured heat is normalized by a mixture's water content (volume basis, assuming the density of water, ρ_W = 1 g/cm^3), as the initial volumetric water content is a measure of the initial porosity of the system- i.e., space that can be progressively filled by the hydration products towards achieving better engineering properties. To better quantify this relationship for both blended and interground systems, heat-strength datasets for the current mixtures were plotted alongside a larger dataset previously developed for blended, OPC-limestone mixtures made using limestone powders having varying median particle sizes, where the OPC content was reduced in 10% increments, from 0-to-50% (by mass) as shown in Figure (5).

As noted in Figure (5), the heat-strength relationship of the current set of mixtures is in good agreement with previously developed datasets. A linear correlation of this nature is significant in that, it suggests that irrespective of limestone addition mode (i.e., intergrinding or blending), measures of heat release through isothermal calorimetry can be used to infer the evolution of mechanical properties in these binders [34,36]. It is also noted that the estimated strength of the 50:50 OPC blends lies intermediate to the Type I/II and Type III OPC mixtures, and is essentially equivalent or slightly superior to the OPC-L mixtures- an expected outcome based on the intermediate AM (Table 2) and level of reaction evolution noted in the 50:50 OPC blended systems as shown in Figures 2 and 3. This relationship then clarifies that for any given mixture, equivalence in terms of cumulative heat release through hydration, when normalized by the water content indicates mechanical property equivalence between the mixtures.

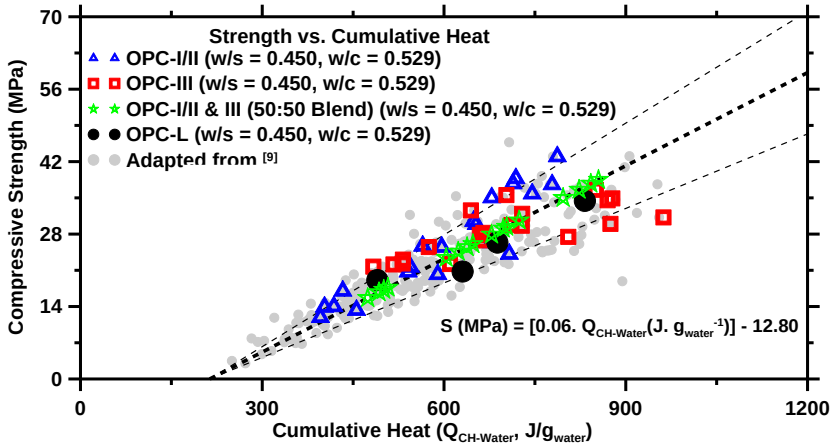

Figure 5: Compressive strength development at ages of 1, 3, 7 and 28 days of hydration as a function of the cumulative heat normalized by water content for the OPC-L, Type I/II and Type III cements, and their limestone blended mixtures. The thick dashed line represents the (linear) best fit line with 20% bounds placed on either direction (thin dashed lines). The datapoints adapted from Kumar et al. ([34]) include evaluations conducted on Type I/II, Type II/V and Type III cements, for cement replacement levels ranging between 0-50% (mass basis) by particle size classified limestone, for strength and heat determinations carried out at 1, 3, 7 and 28 days. The compressive strength of the 50:50 OPC blends containing 15% (blended) limestone of different particle sizes was *estimated* using the heat release measured through hydration, and the strength-heat correlation function detailed in the figure.

2.4 Boundary nucleation and growth Model for Cement Hydration

Classical and modified forms of boundary nucleation and growth (BNG) models have often been applied to describe the hydration of cement systems [17,37,38,39,40]. These models simulate reactions as a nucleation and growth process that starts at the solid phase boundaries. In these models, a single product of a constant density is assumed to nucleate and its growth is treated as the rate-controlling mechanism that determines the kinetics of the reaction [39,41,42]. BNG models have been formulated with a variety of assumptions for the reaction rate-controlling mechanisms, including nucleation site saturation [39,43], product growth control [39,44,45], and continued nucleation of products [46,47]. This study applies a modified form of a BNG formulation to better interpret the influence of the limestone addition mode (i.e., blending or intergrinding) on the kinetics of reactions using Equations (2-6) as shown below [17]:

$$Extent\ Transformation\ (X) = 1 - exp[-2a_{BV} \int_{0}^{G_{out}t} \left(1 - exp\left(-A_f\right)\right)dy] \quad \text{(equation 2)}$$

where: X is the volume fraction of the reactant transformed to product, G_{out} is the isotropic outward growth rate of the product phase, y is a variable of integration, a_{BV} is the boundary area per unit volume, t is the simulation time (h) and A_f is the extended area of the transformed product phase described in Equations (3) and (4).

$$A_f = \pi \left[I_{density}.G_{par}^2.\left(t_r^2 - \frac{y^2}{G_{out}^2}\right) + I_{rate}.G_{par}^2.\left(\frac{t_r^3}{3} - \frac{y^2 t_r}{G_{out}^2} + \frac{2y^3}{3G_{out}^3}\right)\right] if (y \geq G_{out}.t_r) \quad \text{(equation 3)}$$

$$and, A_f = 0\ \ if\ (y < G_{out}.t_r) \quad \text{(equation 4a)}$$

$$Here, (t_r = (t - t_0)) \quad \text{(equation 4b)}$$

where: $I_{density}$ (μm^{-2}) is the nucleation density of the product, that is, the starting number of supercritical nuclei per unit surface area, I_{rate} ($\mu m^{-2}. h^{-1}$) is the nucleation rate, G_{par} ($\mu m. h^{-1}$) is the growth rate parallel to the particle surface, and G_{out} ($\mu m. h^{-1}$) is the outward growth rate, perpendicular to the particle surface. The cumulative heat evolved by reaction of the cement is computed using a scaling parameter, A (kJ/mol), as shown in Equation (5) [46]:

$$Rate\ of\ heat\ evolution\ \left(\frac{dH}{dt}\right) = A.\left(\frac{100}{100-r}\right)\frac{dX}{dt} \qquad \text{(equation 5)}$$

where: r (%) is the (mass) percentage replacement level of filler which accounts for the effects of dilution (i.e., a reduction in reactive cement content). In addition, since the simulations begin only at the end of the induction period which varies slightly from one mixture to another, the simulation time is mapped to real time by using a parameter t_0 to designate the time at which the induction period ends as shown in Equation (4b). As such, the free variable t_0 is assigned an increasingly positive value when the simulated curve is to be left-shifted, and a decreasingly negative value when the induction period is lengthened and the simulation curve needs to be right shifted along the temporal (time, x) axis. The boundary area per unit volume, a_{BV} (μm^{-1}), is calculated by adding the surface areas of both the cement and limestone filler and dividing by the volume of the overall system (total solid content plus water):

$$a_{BV} = \frac{SSA_{cement}.a_{factor}.\rho_{cement}.\ (100.\ f_{cement})}{V_{free}} \qquad \text{(equation 6)}$$

where, f_{cement} (unitless) is the initial volume fraction of cement, ρ_{cement} is the density of the cement (3.15 $g.cm^{-3}$), V_{free} (μm^3) is initial volume of water present in the system and SSA_{cement} is

the specific surface area of the cement. The parameter a_{factor} (unitless) acts as a free variable representing a "virtual AM" used in the simulations. For all simulations, the values of I_{rate}, G_{out} and G_{par} are drawn from prior simulations of OPC/limestone blends [17] and are thus noted as 0.0 $\mu m^{-2}.h^{-1}$, 0.03 $\mu m.h^{-1}$ and 4.0 $\mu m.h^{-1}$ respectively. It should be noted that the assignment of I_{rate} = 0.0 $\mu m^{-2}.h^{-1}$ would correspond to the case of nucleation site-saturation, implying that growth of the product phase begins from nuclei that are initially present, or form at very early ages such that no further nuclei are permitted to form after the initial *nucleation burst*. While site saturation was the assumption considered in this case, impositions of a constant nucleation rate (i.e., I_{rate} > 0) and product growth rate control have also been demonstrated to successfully simulate cement hydration [17,39,45,47]. In all the equations above, f_{cement} (unitless) and a_{BV} (μm^{-1}) serve as input variables while A (kJ/mol), $I_{density}$ (μm^{-2}), a_{factor} (unitless) and t_0 (hour) remain free (fitting) variables. To fit the response of the limestone containing pastes, a simplex algorithm [17] was applied as follows: (1) $I_{density}$ and a_{factor} are varied within defined constraints to match the upslope and the time of peak through the acceleration regime, (2) the parameter A is scaled to match the amplitude corresponding to the heat flow rate at the time of the main peak, and (3) t_0 is adjusted to shift the simulated heat flow response to the right or to the left to temporally match the measured heat response as shown in figure 6.

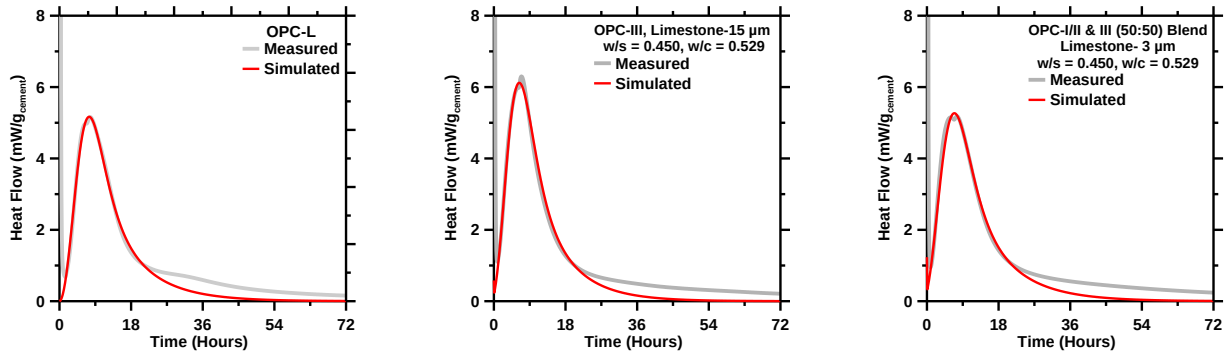

(a) (b) (c)

Figure 6: Representative graphs which show a comparison of the measured and BNG simulated heat release behavior for binary (OPC + limestone) paste systems.

Figure 7 and Table 3 show representative best-fit results and parameters used in simulations for the interground and limestone blended systems. The parameter optimizations suggest that A and t_0 varied within a small range between (57-68 kJ. mol^{-1}) and (0 to -1.13 hours) respectively, but no systematic trend was found in their variation. The values of a_{factor} (i.e., virtual AM) and $I_{density}$ (i.e., nucleation density) both do increase with decreasing limestone size (and surface area) indicating that fine limestone is a better acceleration agent than coarse limestone (Figure 7c) [47]. As a starting point: information of particle size dependence can be correlated with the calculated nucleation density as shown in Figure (7a), to determine how reaction evolution in blended Type I/II and Type III OPCs can be equated to any interground systems. For example: Figure (7) suggests that *reaction equivalence* to the interground system can be achieved by blending (by mass), 15% limestone of progressively increasing fineness, as the OPC fineness decreases, e.g., finer limestone for a Type I/II OPC and coarser limestone for a Type III OPC respectively. This result is intuitively reasonable (e.g., Table 1 and 2), as actions of this nature would act to boost the solid surface area of the Type I/II mixtures, and depress the surface area of the Type III mixtures as a means to equate reaction rates. Expectedly, the blended OPC (50:50, Type I/II and

Type III) mixtures lie between the two extreme cases- a function of their intermediate solid surface area.

The fitting parameters a_{factor} and $I_{density}$ were combined to calculate the number of supercritical product nuclei produced per gram of reactant as shown in Equation (7). Here, product nuclei (g_{cement}^{-1}) denotes the number of supercritical nuclei produced per gram of cement reacted and $SSA_{Effective,Simulations}$ (m^2. kg_{cement}^{-1}) and $SSA_{Effective,Measured}$ (m^2. kg_{cement}^{-1}) represent the simulated and measured values of surface area per unit mass of cement that is *effectively* available for the nucleation (and onward growth) of the hydration products.

$$Product\ Nuclei\ (\#/g_{cement}) = \left(SSA_{cement}.a_{factor}\right).I_{density} \quad \text{(equation 7a)}$$

$$where, SSA_{Effective,Simulations} = SSA_{cement}.a_{factor} \quad \text{(equation 7b)}$$

$$and, SSA_{Effective,Measured} = SSA_{cement}.\ AM \quad \text{(equation 7c)}$$

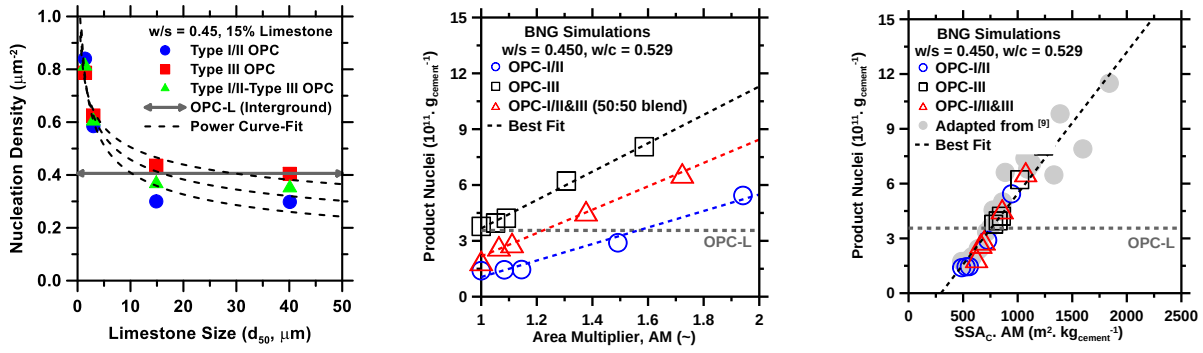

(a) (b) (c)

Figure 7: Results of the BNG calculations which describe: (a) the nucleation density as a function of the limestone particle size, and product nuclei per gram of cement as a function of: (b) the AM for the various cement types used in this study and (c) effective surface area available per unit mass of cement. The datapoints adapted from [34] include evaluations conducted on Type I/II, Type II/V and Type III cements.

The number of supercritical product nuclei produced per gram of cement reacted is plotted against the AM (Figure 7b). For each cement type, increasing the available solid surface area, by the incorporation of size classified limestone (or reducing the OPC fineness), results in a linear increase in the number of nuclei that participate in reactions. This trend suggests that, all other parameters remaining equal, fine limestone by provisioning a higher solid surface area for a given mass is able to induce the formation of a larger number of supercritical hydration product nuclei which participate in reactions (i.e., higher $I_{density}$ values, while I_{rate} remains fixed), an action which would enhance the formation of the reaction products, and thus accelerate early age reactions [48,49].

Table 3: Parameters used to simulate the hydration response of interground and blended paste systems using a modified BNG formulation.

Batch	**A**	**I_{rate}**	**$I_{density}$**	**G_{out}**	**G_{par}**	**SSA_{cement}. a_{factor}**	**t_0**
#	**($kJ.mol^{-1}$)**	**($\mu m^{-2}.h^{-1}$)**	**(μm^{-2})**	**($\mu m.h^{-1}$)**	**($\mu m.h^{-1}$)**	**($m^2.kg_{cement}^{-1}$)**	**(h)**
OPC-I/II							
L-0.7µm	59.11	0.0	0.840	0.03	4.0	6481.00	-0.21
L-3µm	60.71	0.0	0.585	0.03	4.0	4955.40	-0.69
L-15µm	56.74	0.0	0.300	0.03	4.0	4862.00	-1.13
L-40µm	57.39	0.0	0.298	0.03	4.0	4861.21	-1.00
OPC-III							
L-0.7µm	68.24	0.0	0.787	0.03	4.0	10239.04	-0.65
L-3µm	60.32	0.0	0.625	0.03	4.0	9944.69	-0.56
L-15µm	63.03	0.0	0.435	0.03	4.0	9697.56	-0.72
L-40µm	64.47	0.0	0.404	0.03	4.0	9691.22	-0.52
50:50 Blend of OPC-I/II and OPC-III							
L-0.7µm	61.56	0.0	0.812	0.03	4.0	8176.85	-0.48
L-3µm	61.04	0.0	0.604	0.03	4.0	7623.01	0.00
L-15µm	60.37	0.0	0.367	0.03	4.0	7899.08	-0.87
L-40µm	59.55	0.0	0.351	0.03	4.0	7763.99	-0.68
OPC-L							
OPC-L	60.18	0.0	0.406	0.03	4.0	8771.53	-0.06

In addition to the nucleation density, the number of (supercritical) product nuclei estimated by the simulations can also be plotted as a function of the AM, and the $SSA_{Effective,Measured}$ (Equation 7c) as shown in Figure 7 (b and c). It is noted that the discrete trend-lines in Figure 7(b) collapse onto a single master curve in the latter case. This result indicates a linear dependence between the number of product nuclei produced through hydration (7.70×10^{14} nuclei per unit area), and the surface area of the system (independent of the limestone addition mode), which is only a function of the specific surface area of the constituent phases, i.e., OPC and limestone. This result suggests that, blended systems can be designed to have equivalent reaction kinetics (and thus strength evolution behavior) as interground systems, and vice-versa, by programming their effective surface areas to be equivalent; by tailoring the: (a) OPC fineness, (b) limestone fineness and/or (c) the extent of OPC replaced by limestone filler. Of course, it should be noted that while this procedure would be simple when blending cements which have *similar* phase chemistries, this endeavor would be much less trivial when blending cements of vastly different phase compositions.

2.5 Summary and Conclusions Chapter 2

This work has compared and contrasted the evolution of hydration and strength in interground and blended limestone systems. By the careful integration of experiments and simulations it is demonstrated that reaction and by extension strength evolution in these systems, is for similar OPC chemistries, broadly a function of the OPC and limestone fineness, and the extent (mass fraction) of OPC replacement by limestone. This result indicates that performance equivalent systems can be proportioned by either blending or intergrinding OPC and limestone so long as the: (1) level of OPC replacement is similar and (2) OPC and/or the limestone fineness can be tailored to achieve *similar* solid surface areas in the system. Of course it should be noted that this

approach would be bounded by limits of: (1) dispersion and agglomeration which may prove problematic when the limestone (or OPC) particle size is sufficiently small, and the level of cement replacement substantial and (2) gel-space ratio [34,48] i.e., quantity of hydration product (C-S-H) formed from the hydration reactions, as beyond a certain point, independent of reaction evolution, if insufficient hydration product formation occurs, strength development will be suppressed [34,49]. It is also important to note that the existence of a single strength-heat master curve *(SHMC)* capable of describing strength evolution in both interground and blended binder systems is significant in that it enables estimations of properties in mixtures constituted by either means [36]. However and as a caveat, it is important to note that the relationship shown in Figure 5 only applies to plain and binary mixtures constituted using broadly *inert* fillers (e.g., limestone). This is because filler agents depending on their reactivity may change the slope of the best-fit line relevant to the SHMC and thus alter the mathematical form of the relationship sketched in Figure 5.

Chapter 3: The Influence of Filler Type and Surface Area on the Hydration Rates of Calcium Aluminate Cement.

3.1 Scope of Chapter 3

As shown in chapter 1, significant efforts have been made to reduce the use of cement as the primary binding agent in concrete [1,2,50]. One topic of significant study has been the so-called filler effect [15,17,34,51,52,53,54], wherein the replacement of OPC by a suitable filler (i.e., quartz, limestone, rutile) results in enhanced reaction rates, allowing for reduction of the OPC content without compromising property gain at early ages. In chapter 2, it was determined that the filler effect results from the enhanced nucleation of hydration products as additional surface area is provided by fine filler agents such as limestone. While a wide range of fillers have been evaluated, in OPC, carbonate-based fillers (e.g., limestone, dolomite) have been noted to show filler effects superior to other mineral agents on account of their superior surface properties, and chemical composition [14,52,55].

Unlike OPC, calcium aluminate cements (CACs) consist dominantly of monocalcium aluminate ($CaO{\cdot}Al_2O_3$, CA) and gehlenite ($2CaO{\cdot}Al_2O_3{\cdot}SiO_2$, C_2AS) [20,56,57,58]. In spite of several decades of use, the influence of fillers on CAC hydration has been lesser studied. Towards this end, the current study uses a combination of experiments and simulations to elucidate the effects of the filler content (i.e., CAC replacement level and w/c increase), filler type (i.e., $CaCO_3$, $CaMg(CO_3)_2$ and α-SiO_2) and surface area (i.e., fineness of fillers) on CAC hydration kinetics. A boundary nucleation and growth model is used to explain the links between surface area, and mineral type on hydration rates [17,34]. The results suggest that CAC-based binders are far less sensitive to mineral filler type, than OPC-based systems.

3.2 Materials and Experimental Methods

A commercially available grey calcium aluminate cement (CAC, referred to as CAC or cement interchangeably, hereafter) Secar®51 produced by Kerneos Aluminate Technologies was used. The oxide composition (Table 1) of the CAC was determined by X-ray florescence (XRF). The mineralogical composition of the CAC as determined using Rietveld refinement of X-ray diffraction (XRD) patterns is (by mass): 73.3% CA, 18.1% C_2AS, 4.9% CT with minor phases in the form of 0.8% CaO, 0.6% C_2F, 1.5% C_3FT and 0.8% Fe_3O_4. The limestone and quartz powders used are commercially available size classified products produced by OMYA A.G. and U.S. Silica. The dolomite used was produced by Blue Mountain Minerals. Oxide compositions of CAC and as well as the main components for the fillers used can be found in Table 4.

The particle size distributions (Figure 8) of the solids were measured using a Beckman Coulter static light-scattering (SLS) analyzer (LS13-320) using isopropanol/sonication for dispersing the powders to primary particles. This methodology allows the quantification of volume fractions of the particles corresponding to each size class ranging between 0.04 μm and 2000 μm using the Mie theory for analysis of light scattering data. Assuming spherical shape of the particles, the total surface area of the particles belonging to each size class is calculated and, ultimately, added to estimate the cumulative surface area per unit volume (m^2/m^3) of the material. By factoring in the density of each powder (i.e. 3150, 2700, 2650 and 2850 kg/m^3 for the CAC, limestone, quartz and dolomite respectively), the specific surface area is obtained in the units of m^2/kg. The uncertainty in the light scattering was determined to be ≈6% based on multiple measurements performed on six replicate samples.

Table 4: Oxide composition of CAC and Main components of fillers				
Sample	**CAC: Secar 51**	**Limestone**	**Dolomite**	**Quartz**
SiO_2	4.71	~	0.70	100.00
Al_2O_3	51.04	~	~	~
Fe_2O_3	2.22	~	~	~
CaO	38.94	~	~	~
MgO	0.59	~	~	~
SO_3	0.00	~	~	~
Na_2O	0.07	~	~	~
K_2O	0.31	~	~	~
TiO_2	2.02	~	~	~
P_2O_5	0.11	~	~	~
$CaCO_3$	~	100.00	19.30	~
$CaMg(CO_3)_2$	~	~	80.00	~
Sum	100.00	100.00	100.00	100.00

Given the irregular, angular nature of the particles considered, the spherical particle assumption results in an underestimation of the solid surface area by a factor of 1.6-to-1.8 [33] for typical pulverized powders. The median diameter (d_{50}) and the specific surface area (SSA) for all materials are presented in Table 5.

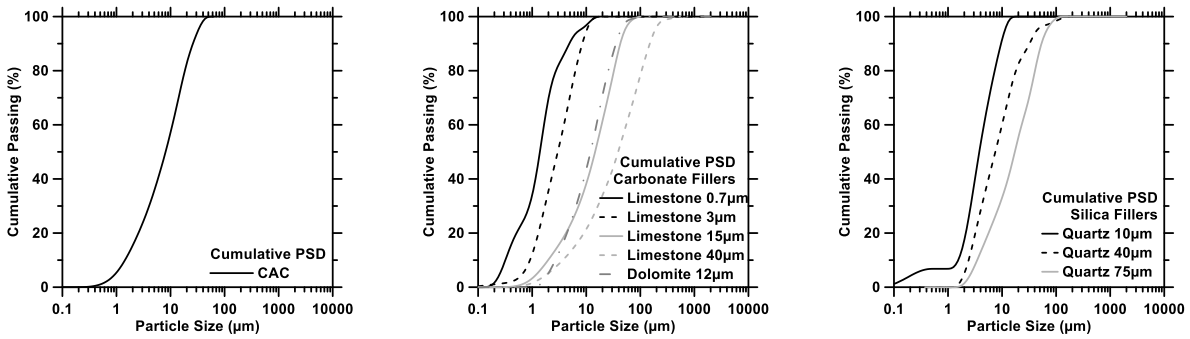

(a) (b) (c)

Figure 8: The particle size distributions (PSDs) of the: (a) calcium aluminate cement, (b) carbonate fillers (limestone, dolomite) and (c) quartz powders used in this study.

Table 5: The nominal specific surface area (SSA) and d_{50} of the solids as calculated using the measured particle size distributions.		
Materials	**SSA (m^2/kg)**	**Size (d_{50}, µm)**
Secar 51	504.85	8.15
Limestone 0.7 µm	2592.13	1.38
Limestone 3 µm	1353.29	2.92
Limestone 15 µm	399.29	14.26
Limestone 40 µm	228.62	39.78
Dolomite	297.25	11.83
Quartz-10 µm	1610.05	3.86
Quartz-40 µm	464.56	7.42
Quartz-75 µm	270.22	17.18

Cementitious pastes were prepared using deionized water at a fixed water-to-solid (w/s = 0.60, mass basis) ratio using a planetary mixer as described in ASTM C305 [13]. To better understand the role of fillers, the CAC content was reduced at mass-based replacement levels ranging from 0-to-50% (mass-basis) by limestone, quartz or dolomite powders. The replacement levels were selected to match the overall area of solids per gram of anhydrous cement across the different fillers used. The additional surface area provided by the fillers was calculated using an area multiplier (AM) proposed by Oey et al. [17] (see equation 8):

$$AM = 1 + \frac{r\, SSA_{filler}}{(100 - r)\, SSA_{cement}} \qquad \text{(equation 8)}$$

where, r (mass %) is percentage of CAC replaced by a filler, SSA_{cement} and SSA_{filler} (m^2/kg) are the specific surface areas of the CAC and filler respectively. The AM parameter accounts for both the dilution effect (i.e., CAC replacement level) and the specific surface area of the solids (i.e., CAC and filler) as was the case in OPC system (chapter 2). By matching AMs, several mixtures were proportioned with an equivalent surface area of solids per gram of anhydrous CAC, i.e., for AM = 1.2, 1.5, 2.0, 3.0. Figure 9 shows the replacement level required to achieve

each AM value for all the fillers used, so long as the CAC replacement level was maintained at ≤ 50%. Table 6 shows the level of CAC replacement required by each filler to ensure the targeted AM values. It should be noted that AM = 3.0 means that this mixture shows a solid surface area which is 3x larger than the pure CAC mixture (i.e., where AM = 1.0). The differences in equation 1 (in chapter 2) and equation 8 arise from the need to easily back calculate the replacement level for a given AM values, in such case the use of equation 1 would have been problematic.

The influence of cement replacement on the rate of CAC reaction was tracked using isothermal conduction calorimetry. The rate and extent of heat release are normalized by the mass of CAC and, as such, the heat evolution profiles serve as direct indicators of hydration kinetics of CAC.

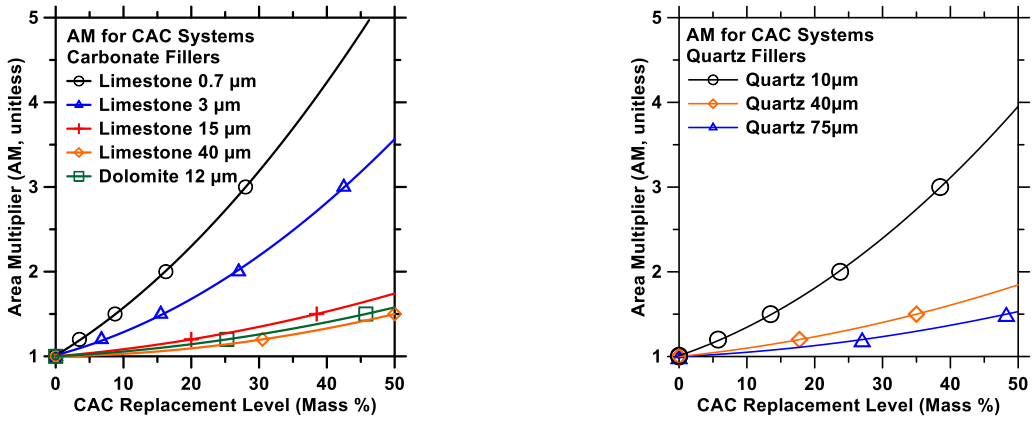

Figure 9: The area multiplier (AM) as a function of level of CAC replacement by: (a) carbonate fillers and (b) quartz fillers. The symbols represent values corresponding to the mixture formulations evaluated in this study.

Table 6: The level of CAC replacement (%) calculated for each filler so as to maintain an equivalent value of the area multiplier (AM).				
Filler	**AM=1.2**	**AM=1.5**	**AM=2**	**AM=3**
Limestone 0.7 µm	3.50	8.75	16.25	28.00
Limestone 3 µm	6.75	15.50	27.00	42.50
Limestone 15 µm	20.00	38.50	N/A	N/A
Limestone 40 µm	30.50	50.00	N/A	N/A
Dolomite	25.25	45.75	N/A	N/A
Quartz 75µm	27.00	48.25	N/A	N/A
Quartz 40µm	17.75	35.00	N/A	N/A
Quartz 10µm	5.75	13.50	23.75	38.50

3.3 Experimental Results and Discussion

Due to the use of ambient temperatures and for w/c $\geq$ 0.60, it is expected that CAH_{10}, C_2AH_8 and AH_3 hydrates form, and are present in the systems considered herein [20]. Representative X-ray diffraction (XRD) patterns shown in Figure 10 illustrate that at ages less than 2 days, CAH_{10} and C_2AH_8 are the primary hydration products independent of the filler present. In systems prepared without and with fillers, C_2AH_8 and CAH_{10} are the primary hydration products respectively. Formation of CAH_{10}, which is a water-rich hydration product, instead of C_2AH_8, at early ages, can be explained due to a higher water-to-cement ratio (w/c) in systems prepared with fillers. It should be noted that due to the very low dissolution rates of limestone and dolomite [59,60], substantial reaction between CA and carbonate provided by carbonate based fillers is not expected [22,61]. This is corroborated by the XRD patterns shown in Figure 10(a), wherein the weak intensities of monocarboaluminate indicate its presence in minute quantities. Therefore, it is assumed that all fillers used in this study do not partake in reaction with the anhydrous CAC, and, as such, remain "inert" for the ages considered.

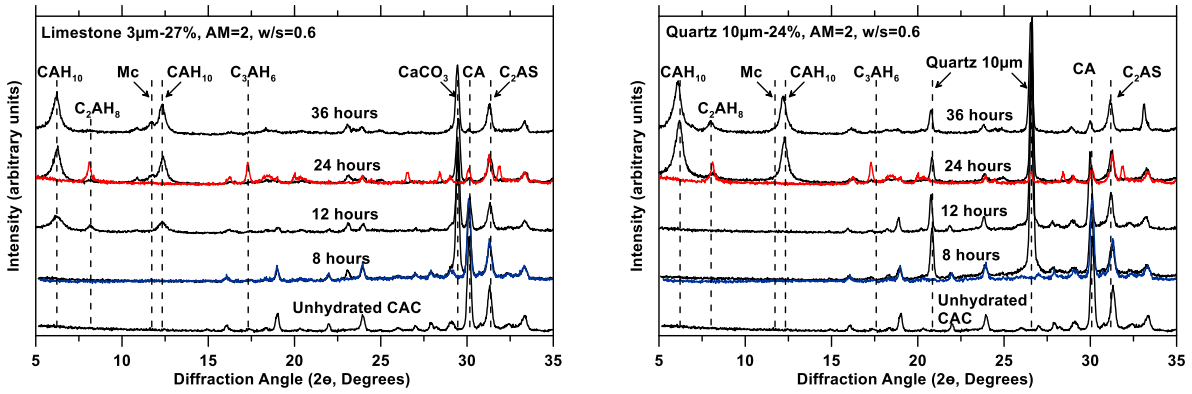

Figure 10: XRD patterns of CACs pastes prepared at a w/s = 0.60 for: (a) CAC replacement by limestone at a level of 27% (by mass) and (b) CAC replacement by quartz at a level of 24% (by mass). The CAC replacement levels thus selected ensure AM = 2. The blue and red XRD patterns correspond to pure CAC pastes (no filler) prepared at w/s = 0.60 at ages of 8 and 24 hours for comparison.

Figure 11 shows representative heat evolution profiles for the plain and binary pastes (i.e., CAC + filler) prepared for AM = 1.2, 2.0 and 3.0. The reference system corresponds to a pure CAC (no filler) paste prepared at w/s = w/c = 0.60 (w = water, s = solids, c = CAC, on a mass basis). It is important to clarify that, in this study; w/c refers exclusively to the relation (mass basis) of water to CAC without consideration of the filler. On the other hand, w/s refers to the mass relation of water to all the solids present in the binder (i.e., CAC + filler). In cases where no filler is present w/c = w/s. From Figure 11 it is observed that CAC hydration is accelerated in the presence of fillers as compared to the reference system. The enhancement in hydration is noted qualitatively in terms of the increase in the value of the main heat-flow peak. Increasing the filler replacement level induces a shortening of the induction period and left-shift of the main heat-flow peak (Figure 11a). This is interesting because in mixtures having equivalent AM's (but not CAC replacement), the total solid surface area available for the nucleation of the hydrates is the same, but the effective w/c is different and scales with the replacement level. This relationship between the hydration kinetics and w/c thus, suggests that independent of surface area, a higher

w/c leads to enhanced hydration of CAC's. To verify this hypothesis, the hydration kinetics of pure CAC pastes prepared at different w/c were examined (Figure 11d). Indeed, increasing the w/c results in enhanced reactivity. Similar results have been reported by Gosselin et al. [62] and Siddiqui et al. [63], wherein enhanced reactivity of CA was attributed to the enhanced growth of the CAC hydrates when additional space is available in the microstructure. It is however postulated that hydration of CAC with increasing w/c is enhanced only up to a limiting w/c value, after which no further enhancement is noted.

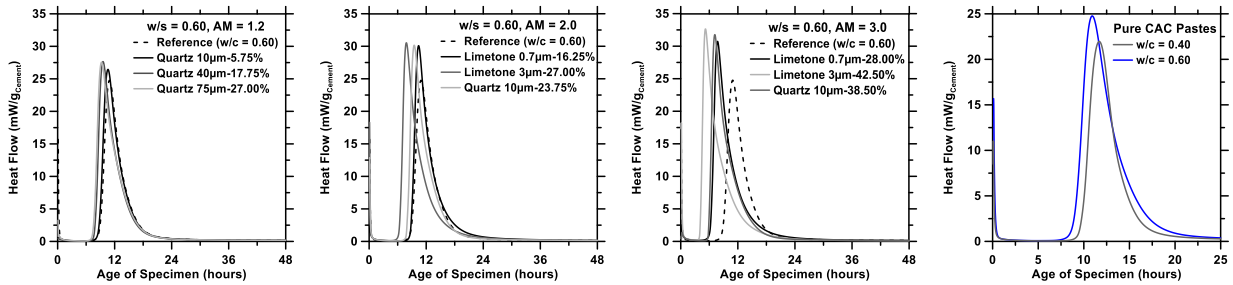

(a) (b) (c) (d)

Figure 11: Measured heat evolution profiles for binary paste systems (w/s = 0.60) for (a) AM=1.2 (b) AM=2 and (c) AM=3. (d) Heat evolution profiles of CAC pastes prepared at different w/c.

In order to distinguish the effects of surface area from water availability, mixtures having the same level of CAC replacement constituted using different mineral fillers were compared. These mixtures showed different solid surface areas, albeit at the same CAC (mass) replacement level and thus w/c. Figure 12 shows the heat evolution profiles for systems containing 27% and 38.5% of the CAC replaced by limestone and quartz fillers. It is seen that at the same replacement level (i.e., same amount of water available for CAC hydration), the reaction rate enhances with AM on account of a higher surface area being available for product phase nucleation. These results indicate that two factors i.e., surface area availability and water availability both exert controls on the CAC reaction rates.

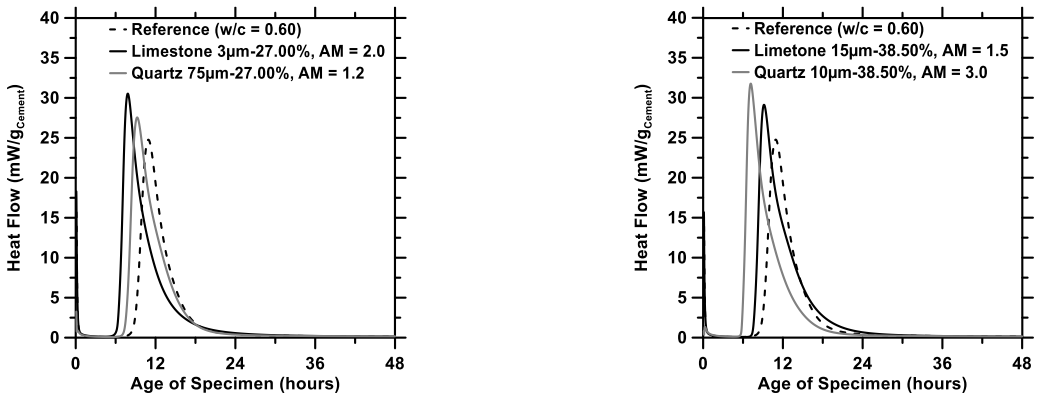

Figure 12: Heat release curves for CAC mixtures for: (a) 27% replacement of CAC and (b) 38.5% replacement of CAC, by limestone and quartz fillers. The reference designates a cementitious blend containing no filler agents, i.e., pure CAC for w/s = 0.60.

While discussing water availability it should be pointed out that some of the filler containing mixtures considered herein, showed a tendency to bleed. It is important to quantify the content of such bleed water as if the mixture is to set with bleed water on the surface, this water is not uniformly available to partake in hydration – and should be discounted from consideration [64]. The consolidation of the paste in the vertical direction during the plastic state also alters the packing of particles – resulting in a reduction in the solid-solid separations in the material. To better quantify bleeding effects, the bleed water exhausted to the sample surface was removed and its mass determined for all mixtures considered herein, over the first 8 hours of hydration. This data was used to quantify the actual w/s and w/c for each mixture to understand any possible impact on CAC hydration rates. Expectedly, the high w/c systems (i.e., those containing a higher quantity of mineral filler) expel more water; an effect which exacerbates as the filler particle size increases (i.e., when filler particles coarser than the CAC are introduced; as shown in Figure 13).

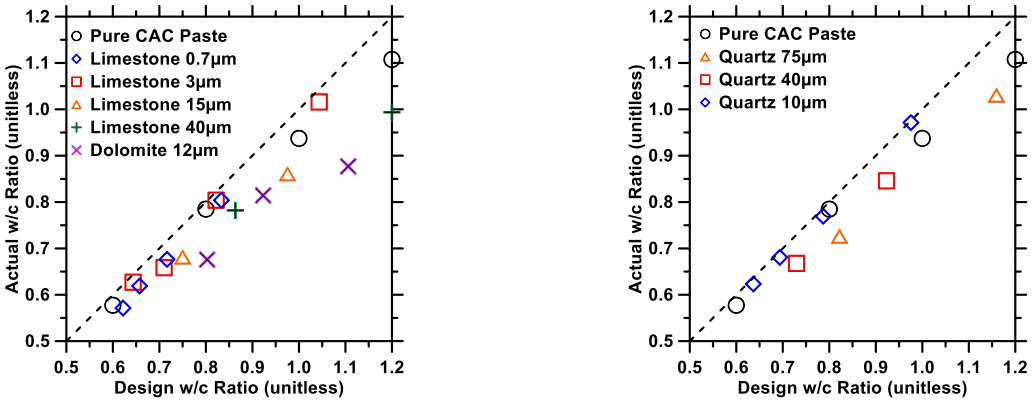

(a) (b)

Figure 13: The actual w/c of the mixtures determined by correcting for the effects of bleeding, as a function of the design w/c for: (a) carbonate fillers and b) quartz fillers.

The heat evolution profiles presented in Figures (12-13) were processed to extract calorimetric parameters indicative of CAC hydration kinetics including: (a) slope during acceleration regime, (b) inverse of time elapsed from initial water contact to the main heat peak, and (c) amplitude of the heat peak (i.e., the heat flow value at the main peak). These quantities were analyzed in the context of the actual w/c and the surface area of the solids, presented in the form of the AM. Figure 14 shows the calorimetric parameters as function of the actual w/c for each mixture. It is seen that as w/c increases, CAC hydration is enhanced, as indicated by the broadly linear correlation between the calorimetric parameters and w/c. It is also noted that at equal w/c, the acceleration induced by all fillers is comparable to each other.

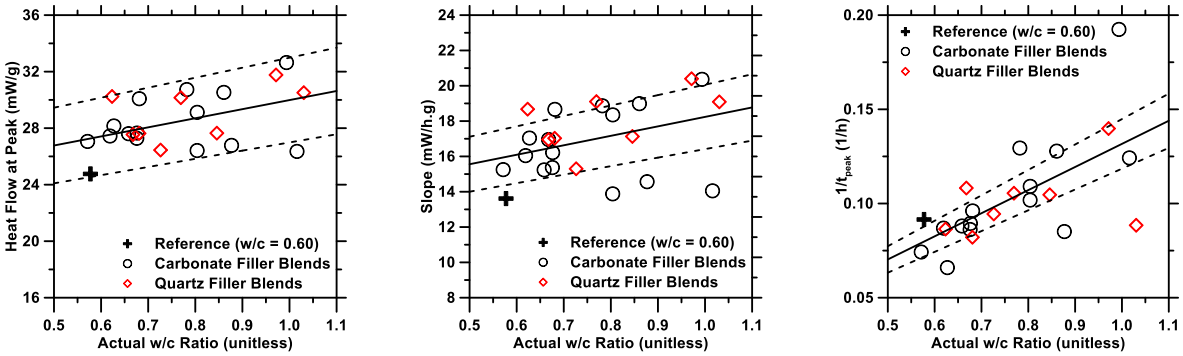

(a) (b) (c)

Figure 14: The correlation between the calorimetric parameters and the actual w/c (determined by discounting water loss due to bleeding) for: (a) heat flow at peak, (b) slope in the acceleration regime, (c) inverse of time to main peak. The solid lines show a best fit line to the dataset while the dashed lines represent a ±10% bound to the best fit line.

In addition to water availability, the amount of surface area available and its relation to CAC hydration kinetics was also examined (Figure 15). CAC hydration is enhanced as the amount of surface area provided by the fillers increases. It is noted that all three fillers: quartz, limestone and dolomite, enhance hydration of CAC equivalently – a significant conclusions which indicates that all fillers, at equivalent surface areas, contribute equally towards enhancing CAC hydration. In light of results shown in Figure (14-15), it is postulated that in CAC binders both carbonaceous and quartz fillers have equivalent acceleratory effects because: (a) the primary hydrates formed in CAC systems are not sensitive to the uptake of carbonate ions and (b) neither of these fillers provide a desired surface (i.e., more desired than the CAC grains themselves) for the nucleation of the CAC hydrates. It should be noted that the scatter in the datasets presented in Figures (14-15) can be attributed to: (a) bleeding, which cannot be remediated during isothermal calorimetry measurements and (b) differences in surface morphologies of the fillers, which may contribute to some differences in reaction rates. The morphologies of the filler can indeed have an impact in the density of product nuclei that form on their surface. Some of the morphological features that can vary amongst the fillers are distribution of defects, etc. Such features, however,

cannot be detected precisely, by means of light scattering or BET surface area determination methods. In the particular case of bleeding, it is possible that even after the CAC paste has hardened, bleed-water could progressively permeate into the sample and, consequently, affect hydration of CAC and heat evolution profiles.

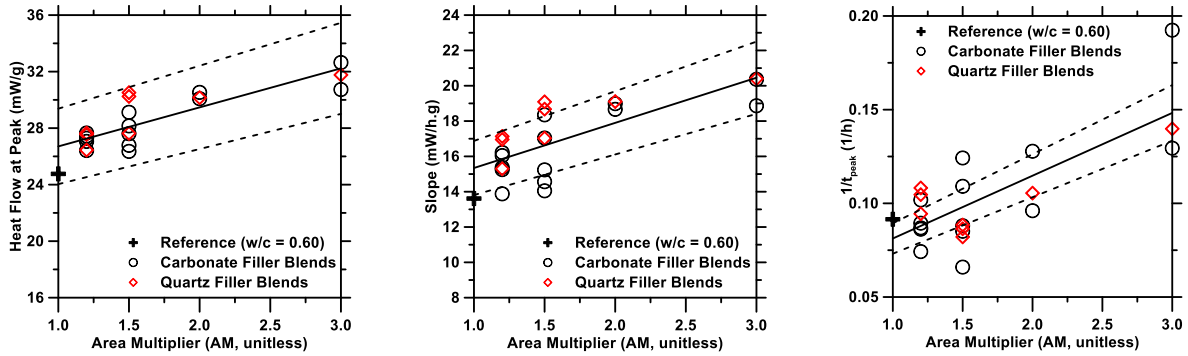

(a) (b) (c)

Figure 15: The correlation between the area multiplier (AM) and: (a) heat flow at peak, (b) slope of the acceleration regime, (c) inverse of time to main peak. The solid lines show a best fit line to the data set while the dashed lines represent a ±10% bound to the best fit line.

3.4 Boundary Nucleation and Growth Model for Cement Hydration

The hydration of OPC's and pure cement phases has widely been studied using phase boundary nucleation and growth (BNG) models [37,44,65,66,67,68] as was presented in chapter 2 of this document. These models simulate the nucleation and growth of a single product phase that starts at the solid phase boundaries. However, these models can incorporate different assumptions about the nucleation process (i.e., homogeneous or heterogeneous), frequency of nucleation (i.e., site saturation or continuous nucleation) and mechanisms of product growth (i.e., isotropic or anisotropic growth of product). Due to their flexibility, BNG models have been successfully extended to study the effects of various process parameters including addition of chemical admixtures [69,70] and mineral filler additions [17,34].

Few studies have applied BNG models to describe hydration of CAC-based systems. Ukrainczyk [71] applied a combination of three different mechanisms: i.e., nucleation and growth, chemical interaction and mass transfer to simulate CAC hydration. This study applies a modified BNG formulation, described previously to track the influences of different fillers on the kinetics of reactions in CAC based systems [17,34,37,66,69,72,73]. A filler is assumed to accelerate CAC reactions, the extent of which is calculated from Eq. (9), by providing only additional surface area for product nucleation, without any impacts on the nature of the CAC hydration products, in terms of their properties or composition, i.e., the filler is assumed to be inert (see Figure 10). It is important to notice that these same equations were used in chapter 2 to describe the nucleation and growth model for OPC hydration, these equations are presented again to facilitate the reading of this chapter.

$$Extent\ Transformation\ (X) = 1 - exp[-2a_{BV} \int_0^{G_{out}t} \left(1 - exp\left(-A_f\right)\right)dy] \qquad \text{(equation 9)}$$

where: X is the volume fraction of the reactant transformed to product, G_{out} is the isotropic outward growth rate of the product phase, y is a variable of integration, a_{BV} is the boundary area per unit volume, t is the simulation time (h) and A_f is the extended area of the transformed product phase described in Equations (10-11).

$$A_f = \pi \left[I_{density}.G_{par}^2.\left(t_r^2 - \frac{y^2}{G_{out}^2}\right) + I_{rate}.G_{par}^2.\left(\frac{t_r^3}{3} - \frac{y^2 t_r}{G_{out}^2} + \frac{2y^3}{3G_{out}^3}\right)\right] \qquad \text{(equation 10)}$$

$$if (y \geq G_{out}.t_r)$$

$$and, A_f = 0 \ if \ (y < G_{out}.t_r) \qquad \text{(equation 11a)}$$

$$Here, (t_r = (t - t_0)) \qquad \text{(equation 11b)}$$

The model formulation is discussed in detail in chapter 2 and elsewhere [17,34,69]. The parameters used in the model include: (a) $I_{density}$ (μm^{-2}), the nucleation density of the product, that is, the number of supercritical nuclei per unit surface area formed at the time of nucleation event ($t_{0)}$, (b) I_{rate} ($\mu m^{-2}. h^{-1}$), the nucleation rate, (c) G_{par} ($\mu m. h^{-1}$), the growth rate parallel to the particle surface, (d) G_{out} ($\mu m. h^{-1}$), the outward growth rate perpendicular to the particle surface and (e) a_f (unitless), the simulation analogue of the area multiplier (AM) which represents in the increase the in solid surface area provided by fine fillers. The w/s, specific surface area of the CAC and the fillers (SSA_{cement} and SSA_{filler}) and CAC replacement level (r, %) are used as inputs. The cumulative heat evolved by the reaction of the CAC is computed using a scaling parameter, A (kJ/mole), as shown in Equation (12):

$$Rate of\ heat evolution = \frac{dH}{dt} = A\left(\frac{100}{100-r}\right)\frac{dX}{dt} \qquad \text{(equation 12)}$$

where: X is the volume fraction of reactant transformed to product, r (%) is the mass-based percentage replacement level of mineral filler (when present) which accounts for the effects of dilution (i.e., a reduction in the CAC content). In addition, since the simulations begin only at the end of the induction period which varies slightly from one mixture to the another, the simulation time is mapped to real time by using a parameter t_0 (hours).

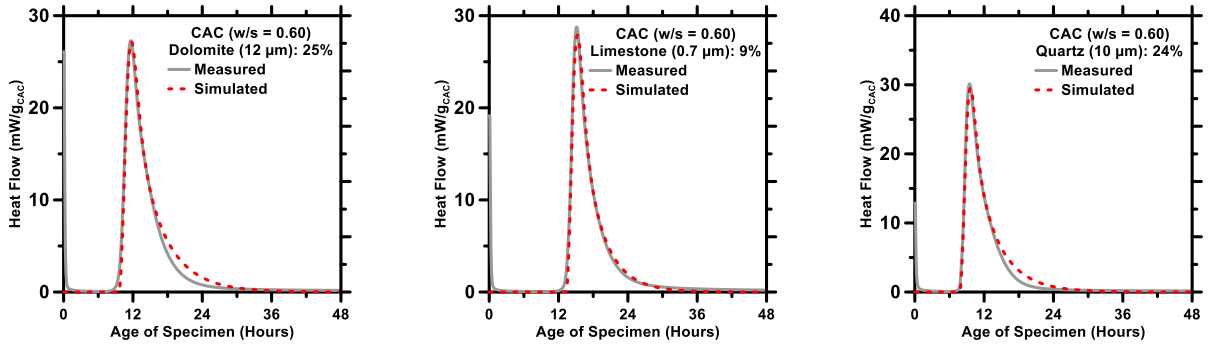

(a) (b) (c)

Figure 16: A comparison of representative measured versus BNG simulated heat evolution profiles for a range of CAC mixtures. The % value denotes the mass-based replacement level of the CAC by a mineral filler.

For all simulations, I_{rate}, G_{out} and G_{par} are fixed; taking values of 0.00 $\mu m^{-2}.h^{-1}$, 0.054 $\mu m.h^{-1}$ and 0.027 $\mu m.h^{-1}$ respectively. The 2:1 ratio of the outward product growth rate with respect to the parallel one is representative of dendritic growth of the product [45]. Since, the growth rates of the hydration products in CAC systems have not been measured, the value of the outward growth rate is drawn from simulations of other cementitious systems [17]. It is pointed out that the assignment of I_{rate} = 0.00 $\mu m^{-2}.h^{-1}$ corresponds to nucleation site-saturation, implying that growth of the product phases begins from nuclei that are initially present, or form at very early ages, and no further nuclei are permitted to form after the initial nucleation burst. To fit the reaction response of the mixtures, a simplex algorithm was applied, which iteratively varies the values of the $I_{density}$, a_{factor}, A and t_0, within pre-defined constraints, to minimize the difference between the simulated and measured heat evolution profiles [17]. When the simplex algorithm converges, the values of the fitting parameters are extracted and noted as the optimum values. Amongst the variable parameters, a_f and $I_{density}$, are most critical as they can be combined with SSA_{Cement} to calculate the number of supercritical product nuclei produced per gram of CAC as shown in Equation (13).

$$Product\ \ Nuclei(\#/g_c) = (SSA_c.a_f).I_{density} \qquad \text{(equation 13)}$$

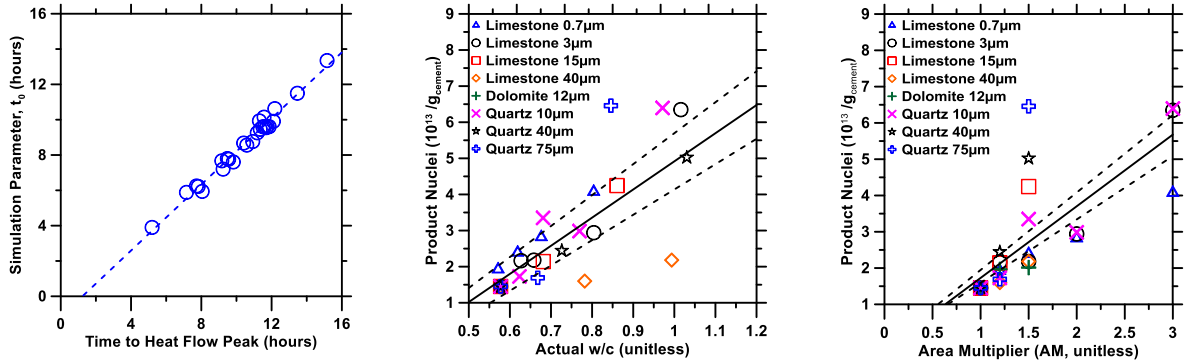

(a) (b) (c)

Figure 17: (a) A comparison of the simulation parameter, t_0 as a function of t_{peak} (time to the main peak) extracted from measured heat profiles across all systems. Product nuclei formed per gram of CAC as a function of: (b) the actual w/c and (c) area multiplier (AM). The solid line indicates best fits and the dashed lines indicate ±10% bounds.

Figure 16 shows representative heat evolution profiles obtained via BNG simulations, compared against experiments. There is good agreement between the experiments and simulations across systems containing different fillers and CAC replacement levels. Excellent agreement is noted between the simulation parameter, t_0, and the time to the main peak (see Figure 17a). This is expected because systems in which the onset of product formation is accelerated, values of t_0 are low. The values of the supercritical product nuclei formed at the end of the induction period were examined. As seen in Figure 17(b), with increasing w/c, the number of the product nuclei formed increases in a linear manner. This trend is in good agreement with observations from Figure 14, suggesting that the hydration of CAC is enhanced when there is more space (i.e., water, or porosity per unit mass of CAC) available in the microstructural volume [62]. It should be clarified here that a higher water content per unit mass of cement (w/c) does not necessarily translate to a higher solid-to-solid (i.e., inter-particle) distance, as explained later in this section. This increase in the number of product nuclei is also noted with an increase in the AM (Figure 17c), suggesting

that the availability of water and surface are both important contributors to CAC reaction rates. It is uniformly noted, no preference to a given filler is seen, with all fillers provided the same acceleration in CAC hydration – for equivalent AM, and w/c.

Figure 18 shows the inter-particle distance calculated at the time of mixing of the solids with water calculated using a microstructural model [34], for all three mineral fillers across different CAC replacement levels. It is seen that fillers which are finer than CAC, cause a progressive decrease in the inter-particle distance with increasing replacement levels. On the other hand, coarser fillers cause an increase in the inter-particle distance, more so as the replacement level of CAC by a coarse filler increases. It is seen that at the same replacement level, (i.e., equivalent w/c) the quartz, limestone and dolomite filler produce widely different inter-particle distances on account of differences in their particle size distributions. However, as shown in Figure 17(b), at the same w/c, all three fillers enhance hydration of CAC similarly. These trends show that the enhancement in CAC hydration depends on the effective w/c, i.e., a measure of the total space available in the microstructure per unit mass of cement, but not necessarily the inter-particle (i.e., solid to solid) distance so long the amount of available surface area remains consistent.

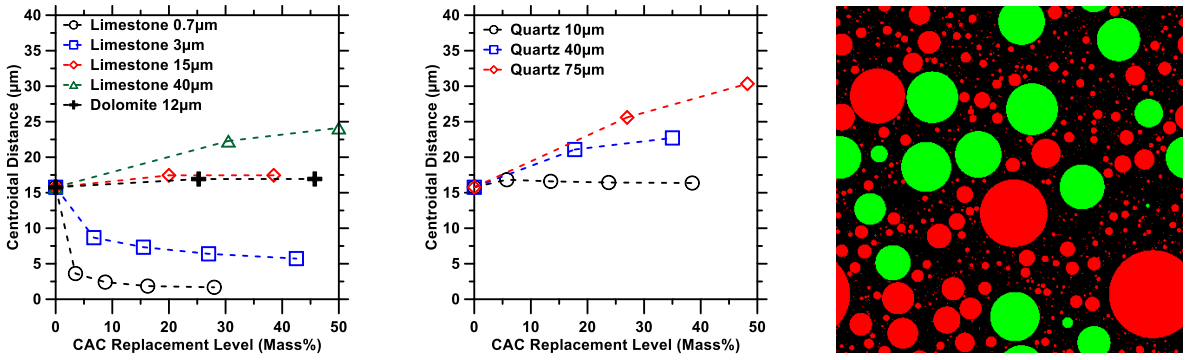

(a) (b) (c)

Figure 18: The average centroidal solid-to-solid distance calculated for various CAC systems prepared at a w/s = 0.60 with CAC replaced by: (a) carbonate and (b) quartz fillers at replacement levels ranging from 0 to 50% (by mass). The distances are calculated by averaging the distances between the center of a particle with respect to its nearest neighbors, packed within a three-dimensional virtual cube for an edge length (of the cube) of 1000 µm. (c) A 2D slice of a 3D-microstructure for a system prepared at w/s = 0.60 with 10% of the CAC (red spheres) replaced by dolomite (green).

Figure 17(c) shows that the number of product nuclei, formed at the end of the induction period, is linearly proportional to additional surface area provided by the fillers. This suggests that CAC hydration is enhanced by the provision of additional solid surface area for the heterogeneous nucleation of products. For equivalent (incremental) surface areas provided by the different fillers, the enhancement in CAC hydration remains broadly similar. This supports the idea that all three filler types used in this study promote the nucleation of products onto their surfaces equivalently, and rules out the possibility of the carbonaceous fillers participating in any substantial chemical interaction with the anhydrous or product phases present in CAC systems, especially so at early ages (i.e., less than 7 days, see Figure 10).

3.5 Summary and Conclusions Chapter 3

The hydration kinetics of CAC-based mixtures has been examined in the presence of both carbonate (i.e., limestone and dolomite) and quartz fillers. By using the concept of an area multiplier (AM), the increased surface area provided by the fillers has been correlated with noted

increases in CAC reaction rates. In addition to surface area, CAC reaction rates are also dependent on w/c, i.e., the amount of space available in the microstructure, this is remarkable as water availability seems not to play a role in OPC hydration (chapter 1). Unlike the case of OPC (chapter 1), CAC's show no preference for filler chemistry, or type – as such, for an equivalent increase in surface area, all fillers provide equivalent enhancements in reaction rates. This equivalence in acceleratory effects amongst the three fillers examined herein is attributed to: (a) their inert nature, i.e., their inability to partake in chemical reactions with the CAC, especially at early ages and for the temperatures considered, and, (b) equivalent affinity for heterogeneous nucleation of hydration products onto their surfaces. These conclusions are supported by the outcomes of phase boundary nucleation and growth modeling applied to CAC hydration. It is also shown that the enhancement in hydration of CACs is related to the increase in w/c (i.e., dilution effects) but not necessarily the inter-particle distance between the solid particles at the time of mixing.

Chapter 4: Elucidating the Role of the Aluminous Source on Limestone Reactivity in Portland Cement.

4.1 Scope of Chapter 4

Towards reducing OPC use in binder formulations, emphasis has been placed on replacing OPC with supplementary cementitious materials (SCMs) in the form of: fly ash, blast furnace slags, silica fume, etc. [52,74]. While capable of providing suitable properties, quantities of common SCMs available to replace OPC are often, especially at local scales, inadequate to satiate the desired OPC replacement demand [3,75]. Due to concerns of the limited and the localized availability of SCMs, there is interest in using limestone ($CaCO_3$), an abundant mineral, to reduce clinker factors of OPC, and thus OPC use in concrete. As shown in previous chapters, the replacement of OPC by limestone induces a variety of effects including:

(i) dilution and strength reduction [34,76], (chapter 1 and 2)

(ii) accelerated hydration at early ages that results from the so-called filler effects [17], and,

(iii) changes in particle packing, and hence the microstructure that result when the limestone used has a particle size different from the cement [77]

Of these effects, dilution, i.e., the reduction in strength that accompanies OPC replacement is a considerable issue, as technologically this is the most significant limitation which has ensured that, in practice, OPC replacement by $CaCO_3$ remains limited, and most often on the order of less than or equal to 15% on a mass basis (ASTM C595) [13].

OPC is comprised of four main phases: tricalcium silicate (C_3S), dicalcium silicate (C_2S), tricalcium aluminate (C_3A) and the ferrite (C_4AF) phases, wherein the kinetics of hydration of each phase differs from the others [78]. Hydration of the C_3A in the presence of gypsum ($C\bar{S}H_2$), forms ettringite ($C_6A\bar{S}_3H_{32}$, AFt) at early ages and monosulfoaluminate ($C_4A\bar{S}H_{12}$, sulfate-AFm,

Ms), at later ages when the sulfate source is exhausted. However, when carbonate ions may be present, (e.g., when provisioned by the dissolution of limestone), C_3A reacts with carbonate species to form CO_3-AFm (i.e., carbonate-AFm) phases [14,21,79,80]. Typically, monocarboaluminate ($C_4A\bar{C}H_{11}$, Mc) forms when there is an abundance of calcium carbonate present, and hemicarboaluminate ($C_4A\bar{C}_{0.5}H_{12}$, Hc) forms under carbonate-deficient conditions [21,79]. The presence of the $CaCO_3$ has also been shown to limit the transformation of the ettringite into Ms [14,21,79,80]. C_4AF forms similar hydration products as C_3A, but the kinetics of its reactions are slower [81]. These reactions are detailed in Eqs. (14-18). While the mass balance of the AFt and AFm phases formed is dictated by the SO_3/Al_2O_3 and CO_2/Al_2O_3 ratio(s) of the binder, the stabilization of the CO_3-AFm phases is a significant observation [14,21,79] which indicates that when a favorable (i.e., aluminate rich) chemistry exists, *carbonaceous reactions* resulting in the formation of CO_3-AFm phases can be provoked and perhaps enhanced in cementitious systems.

$$C_3A + 3C\bar{S}H_2 + 26H \rightarrow C_6A\bar{S}_3H_{32} \quad \text{(equation 14)}$$

$$2C_3A + C_6A\bar{S}_3H_{32} + 4H \rightarrow 3C_4A\bar{S}H_{12} \quad \text{(equation 15)}$$

$$C_3A + C\bar{C} + 11H \rightarrow C_4A\bar{C}H_{11} \quad \text{(equation 16)}$$

$$C_3A + 0.5C\bar{C} + 0.5CH + 11.5H \rightarrow C_4A\bar{C}_{0.5}H_{12} \quad \text{(equation 17)}$$

$$3C_4A\bar{S}H_{12} + 2C\bar{C} + 18H \rightarrow C_6A\bar{S}_3H_{32} + 2C_4A\bar{C}H_{11} \quad \text{(equation 18)}$$

In typical OPCs, the aluminate (mainly C_3A) phase content is regulated by governing standards (ASTM C595) [13]. This ensures that the extent of $CaCO_3$ that can react in a typical OPC is quite small and in the range of 2-5% (by mass) [79]. As such, if it is desirable to increase $CaCO_3$ reactivity (defined herein as the rate, and extent of reaction) and thus OPC replacement by

limestone, it is also necessary to enhance the quantity of aluminous phases present. Such enhancements would provide sufficient $Al(OH)_4^-$ (aluminate) species, which under conditions of portlandite saturation would react with $CaCO_3$ to produce CO_3-AFm phases. While a variety of aluminous substances exist, the characteristics of an optimal aluminous source remain unclear. To better understand these aspects, this work evaluates a variety of commercially available aluminous substances including: (1) a grey calcium aluminate cement (CAC1), (2) a white calcium aluminate cement (CAC2), (3) metakaolin (MET) and (4) an amorphous, finely divided hydratable alumina (HA). Each aluminous source is studied separately, in both limestone deficient and excess systems (i.e., $CaCO_3$ contents ranging between 3.5-to-32%, by mass of binder). Deficiency corresponds to the presence of limestone intrinsic to the OPC, while excess corresponds to the replacement of OPC by limestone at a dosage of 30%, by mass. The results are harmonized to comment on the suitability of an aluminous agent as being capable of provoking/enhancing limestone reactions.

4.2 Materials and Methods

4.2.1 Materials

An ASTM C150 [13] compliant Type I/II ordinary portland cement (OPC) was used. The limestone used is a commercially available (>95% $CaCO_3$) product produced by OMYA A.G. The oxide compositions (disregarding minor oxides and renormalized to 100%, mass basis) of the OPC and the aluminous agents are presented in Table 7, along with their mineralogical compositions in Table 8. It is important to note the "Al_2O_3" present in CAC2 corresponds to corundum, which presents marginal (if any) reactivity in aqueous environments [82]. This is a consequence of the CAC2's intended use for refractory applications. HA and MET are amorphous compounds, though some traces of TiO_2 (anatase) are noted in MET. Table 8

additionally presents values of median particle size (d_{50}, μm) and specific surface area (SSA) of the solid reactants used in this study.

Table 7: The simple oxide compositions of the solid materials utilized in this study as determined using X-ray fluorescence (XRF).

Oxide (%)	Type I/II OPC	CAC1	CAC2	HA	MET
SiO_2	20.54	4.87	0.00	0.34	51.36
Al_2O_3	4.97	52.12	80.27	98.99	47.60
Fe_2O_3	3.10	2.28	0.10	0.00	0.39
CaO	65.75	39.75	18.76	0.11	0.02
MgO	2.43	0.60	0.37	0.00	0.09
SO_3	2.75	0.00	0.00	0.00	0.08
Na_2O	0.18	0.07	0.50	0.56	0.28
K_2O	0.29	0.32	0.00	0.00	0.18
Total	**100.00**	**100.00**	**100.00**	**100.00**	**100.00**

Table 8: Density, median particle diameter (d_{50}), specific surface area (SSA) and the mineralogical components of solid reactants used in this study.

Property	Type I/II OPC	CAC1	CAC2	MET	HA	Limestone
Density (kg/m^3)	3150	3150	3040	2200	3200	2700
d_{50} (μm)	8.5	8.15	2.66	5.11	7.09	3.06
SSA (m^2/kg)	509.4	505.8	1899.1	2540.8	347.2	1247.1
C_3S (%)	57.8	-	-	-	-	-
C_2S (%)	18.2	-	-	-	-	-
C_3A (%)	5.5	-	-	-	-	-
C_4AF (%)	9.1	-	-	-	-	-
$Ca(OH)_2$ (%)	0.4	-	-	-	-	-
MgO (%)	1.3	-	-	-	-	-
$CaSO_4 \cdot 2H_2O$ (%)	0.8	-	-	-	-	-
$CaSO_4 \cdot 0.5H_2O$ (%)	1	-	-	-	-	-
$CaSO_4$ (%)	1.2	-	-	-	-	-
CA (%)	-	73.3	38.1	-	-	-
C_2AS (%)	-	18.1	-	-	-	-
CA_2 (%)	-	-	7.5	-	-	-
CT (%)	-	4.9	-	-	-	-
C_3FT (%)	-	1.5	-	-	-	-
C_2F (%)	-	0.6	-	-	-	-
$C_{12}A_7$ (%)	-	-	5.8	-	-	-
CaO (%)	0.5	0.8	-	-	-	-
Al_2O_3 (%)	-	-	48.6	-	-	-
Fe_2O_3 (%)	-	0.8	-	-	-	-
$CaCO_3$ (%)	4.2	-	-	-	-	98.08

A series of cementitious paste mixtures were prepared using de-ionized (DI) water at a fixed water-to-solids ratio (*w/s* = 0.45, mass basis) using a planetary mixer as described in ASTM C305 [13]. The series of mixtures produced comprised: (A) a plain OPC paste, (B) a cementitious paste in which 30% of the OPC (mass basis) is replaced by fine limestone, (C) cementitious pastes in which 5-to-15% of the OPC is replaced in 5% increments (by mass) of a given aluminous source and (D) cementitious pastes in which 5-to-15% of the OPC is replaced in 5% increments by a given aluminous source and an additional 30% of the OPC is then replaced by fine limestone. All OPC replacements are carried out on a mass basis. As such, the cement factor (CF, i.e., the quantity of clinker + gypsum in a given mixture, as a fraction) ranges between: (A) CF = 0.96 (i.e., the $CaCO_3$ content in the OPC is 3.7%, by mass), (B) CF = 0.67, (C) $0.82 \leq CF \leq 0.91$ and (D) $0.53 \leq CF \leq 0.67$ for the range of mixtures considered.

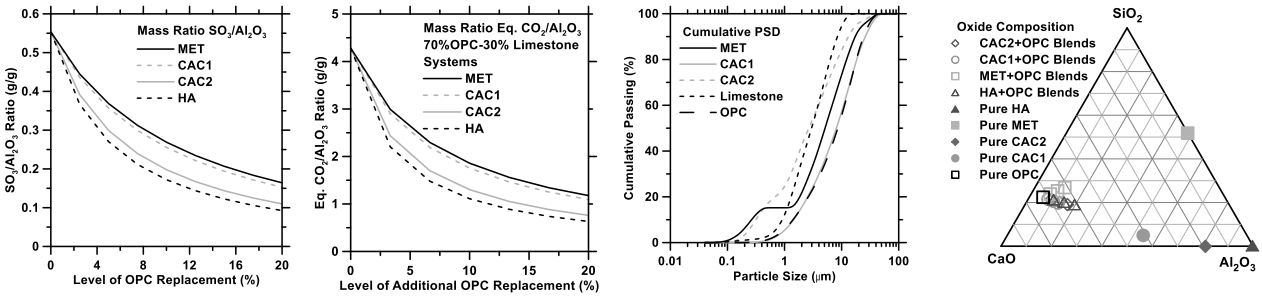

(a) (b) (c) (d)

Figure 19: (a) Sulfate-to-alumina (SO_3/Al_2O_3) mass ratio as a function of increasing OPC replacement by a given alumina source, (b) Carbon dioxide equivalent-to-alumina (CO_2/Al_2O_3) mass ratio for the mixtures containing 30% of limestone (dosed by OPC replacement) as a function of increasing OPC replacement by a given alumina source, (c) The cumulative particle size distributions of the powders, and, (d) The compositions of the binders, minus limestone, plotted on a ternary composition diagram (with CaO-SiO_2-Al_2O_3 at the vertices).

To discount early age kinetic effects, our evaluations are restricted to determinations at 28 and 90 days, at which time the systems are expected to have hydrated substantially. This selection is made to permit characterizations when the systems presents near equilibrium constitutions. It should be noted that the mixtures evaluated present ranges of sulfate-to-alumina (SO_3/Al_2O_3) and

carbonate (equivalent CO_2)-to-alumina (CO_2/Al_2O_3) ratios, by mass, as a function of the aluminous source, and the extent of OPC replacement (see Figure 19). The changes in the binder chemistry are provoked to alter the AFt, and AFm phase balances, and to favor the formation of CO_3-AFm phases. These aspects will be discussed in detail later. It should be noted that cementitious binders are produced to a sulfate optimum which regulates setting time, strength gain, etc. The cementitious binders formulated herein were not optimized for sulfates under the assumption that the OPC used is already optimized, in terms of its sulfate content. Also, in contrast to practical circumstances, the (non-OPC) materials used were of a high-purity, a reflection of the laboratory-scope of the work.

4.2.2 Particle Size Analysis Using Light Scattering

The particle size distributions (PSDs, Figure 19c) of the solids were measured using a Beckman Coulter Static Light Scattering Analyzer (LS13-320) using isopropanol (IPA) and ultrasonication for dispersing the powders to primary particles. The uncertainty in the light scattering analysis was determined to be ≈6% based on analysis of six replicate samples assuming the density of the OPC, limestone, MET, CAC1, CAC2 and HA to be 3150 kg/m^3, 2700 kg/m^3,2200 kg/m^3, 3150 kg/m^3, 3040 kg/m^3 and 3200 kg/m^3 respectively.

The particle size distribution (PSD) of the HA could not be sampled due to significant particle agglomeration, flocculation and clumping. Based on data provided by the manufacturer, the HA presents a N_2-BET sampled surface area in excess of 10000 m^2/kg. Based on the measured PSD, the MET, CAC1, CAC2, OPC and limestone present surface areas of: 1741 m^2/kg, 506 m^2/kg, 1844 m^2/kg, 510 m^2/kg and 1353 m^2/kg respectively assuming that their particles are spherical. This assumption can result in an underestimation of the surface area by a factor of 1.6-to-1.8 [33].

4.2.3 Compressive Strength Measurements

Compressive strength measurements were carried out at 28 and 90 days using cubic specimens (50 mm x 50 mm x 50 mm) cured at 25 ± 1°C in lime water as described in ASTM C109 [13]. The strength reported is the average of three specimens cast from the same batch. The coefficient of variation (CoV) in the measured strength data was in general less than 8% across all samples.

4.2.4 Thermal Analysis (TGA/DTG/DTA)

A Perkin Elmer STA 6000 simultaneous thermal analyzer with a Pyris data acquisition interface was used to determine solid phase quantities in cementitious mixtures. The temperature and mass sensitivity of the analyzer used were 0.25°C and 0.1 μg respectively. To arrest hydration, solvent exchange was performed using isopropanol wherein at a desired age, the hydrated pastes were crushed to a size less than 5 mm and submerged in isopropanol for fourteen days, with isopropanol being replaced at seven days [83]. Following solvent exchange, samples were placed under vacuum, to remove the solvent, and in a desiccator for another seven days. After this, all the samples were finely powdered.

The powder samples were heated under UHP-N_2 purge at a flow rate of 20 ml/min and a heating rate of 10°C/min in neat aluminum oxide crucibles over a temperature range from 35-to-975°C. The weight loss (TG) and differential weight loss (DTG) patterns acquired were used to ascertain the quantities of $Ca(OH)_2$, $CaCO_3$, evaporable, and non-evaporable water present in the system. It should be noted that amount of phases (portlandite and $CaCO_3$) derived from TGA studies are presented in two forms: as a percentage amount of phase present in the dry paste (% dry mass) and as percentage amount of phase present in the dry paste normalized by the OPC content (% dry mass/CF) to account for reductions in the OPC content (i.e., dilution).

4.2.5 Quantitative X-ray Diffraction Analysis Using Rietveld Refinement (QXRD)

Quantitative X-ray diffraction analyses were carried out on powdered cementitious mixtures at desired ages using a Bruker D8-Advance diffractometer in a θ-θ configuration using Cu-Kα (λ = 1.54 Å) radiation. Samples were scanned between 5 and 70° (2θ) in continuous mode with an integrated step scan of 0.017° (2θ) using a VANTEC-1 detector. The time required for acquisition of x-ray diffraction patterns was around 12 minutes. A fixed divergence slit of 0.50° was used during data acquisition. Care was taken to minimize preferred orientation errors by texturing the sample surface. A rotating stage was used to suitably sample the powder during acquisition.

X-ray structure information for the relevant anhydrous and the hydrated crystalline phases was sourced from standard databases or from the literature [84]. Anhydrous materials were analyzed using a protocol described in [85]. For the hydrated pastes, an external standard (i.e., G- factor approach) was used to quantify the X-ray amorphous substances [86,87,88]. The mass attenuation coefficients of the samples were determined by X-ray fluorescence analysis taking into account the amount of bound water that was determined by TGA. Results of Rietveld analyses provide the sum of the phases normalized to 100 mass %. Due to chemical reactions, water is bound in the hydrates, so the total amount of solids increases. To correct for this effect, the amount of bound water was determined (by TGA analysis); so the results refer to the mass of anhydrous materials. The results of Rietveld quantifications in such complex mixtures should be considered carefully, and are thus semi-quantitative rather than absolute.

4.2.6 Thermodynamic Calculations: Prediction of Hydrated Phase Assemblage

Thermodynamic calculations were carried out using a geochemical speciation code, GEMS-PSI: Gibbs Energy Minimization Software, version 2.3.1 [89]. GEMS uses the initial mixture

proportions represented in the form of simple oxides for the solid precursors and the water content, as inputs and applies a convex programming approach in conjunction with datasets of the thermodynamic properties of phases (i.e., solids, liquid and air) to compute equilibrium phase balances and ion-speciation in a multicomponent system. Thermodynamic data of solid and aqueous species were sourced from the GEMS-PSI database, and then amended with additional information relevant to cementitious systems [24,90,91,92,93,94]; Table 9. Equilibrium phase balances and solution phase compositions for the systems considered in this study were computed under standard conditions (1 bar, 25°C). The simple oxide compositions of the solids (i.e., OPC, CAC, limestone etc.), were determined by X-ray fluorescence (XRF) analyses (Table 7). The gas phase at equilibrium with the solids and the liquid phase was set to be CO_2-free air.

Table 9: The Gibbs free energies of formation and molar volumes for relevant hydrated phases at 25°C and p = 1 bar [24].

Phase	$\Delta_f G^0$ ***[kJ/mol]***	**V** ***[cm³/mol]***
C_3AH_6	-5010.1	150
$C_3AS_{0.8}H_{4.4}$	-5368	143
$C_3AS_{0.1}H_{5.8}$	-5054.7	149
$C_3AS_{0.02}H_{5.96}$	-5018.8	143
$C_3AS_{0.015}H_{5.96}$	-5016.8	143
C_4AH_{13} (hydroxy-AFm)	-7326.6	274
C_4AsH_{12} (monosulfoaluminate)	-7778.5	309
C_4AcH_{11} (monocarboaluminate)	-7337.5	261
$C_4Ac_{0.5}H_{12}$ (hemicarboaluminate)	-7336	285
C_2ASH_8 (strätlingite)	-5705.1	216
M_4AH_{10} (OH-hydrotalcite)	-6394.56	220
M_4AcH_9 (CO_3-hydrotalcie)	-6580.15	220
Brucite, $Mg(OH)_2$	-832.23	25
C_6AsH_{32} (sulfate-ettringite)	-15205.9	707
C_6AcH_{32} (carbonate-ettringite)	-14565.6	650
water (H_2O)	-237.2	18
SiO_2 (amorphous)	-848.9	29
C-S-H, tobermorite-type: $C_{0.83}SH_{1.3}$	-1744.4	59
C-S-H, jennite-type: $C_{1.67}SH_{2.1}$	-2480.8	78
$Fe(OH)_3$ (microcrystalline)	-711.6	34
$Al(OH)_3$ (amorphous)	-1143.21	32
$Al(OH)_3$ (gibbsite)	-1151	32

Portlandite, $Ca(OH)_2$, CH	-897	33
Calcite, $CaCO_3$, Cc	-1129.2	37
Gypsum, $CaSO_4 \cdot 2H_2O$	-1797.8	75

C-S-H phases are described within GEMS using the solid-solution model proposed by Kulik and Kersten [95]. In this model jennite $[(CaO)_{1.67}(SiO_2)\cdot(H_2O)_{2.1}]$, tobermorite $[(CaO)_{0.83}(SiO_2)\cdot(H_2O)_{1.3}]$ and amorphous silica (SiO_2) are used as end members of two different solid solution series where one solid solution (tobermorite-jennite) describes the range $0.83 \leq$ (Ca/Si) C-S-H ≤ 1.67 while a second solid solution (amorphous silica-tobermorite) is used to describe the range $0 \leq$ (Ca/Si) C-S-H ≤ 0.83. No account is made for the influences of Al-substitution in the C-S-H, because the thermodynamic phase relations for such modifications to the C-S-H structure are not fully clear [96,97]. Thermodynamic data of relevant AFt, AFm and Fe-bearing phases were taken from the literature and used as is [80,98,99].

XRD datasets revealed the existence of a phase lying along the grossular-hydrogarnet phase line [21,98] (see discussion below). Comparison to patterns of neat hydrogarnet revealed a slight right-shift, presumably caused due to Si-substitution [100,101,102]. Jappy and Glasser [102] studied a range of silica substituted hydrogrossular-like phases (Hy) with end members, C_3AH_6-C_3AS_3. They reported that the unit cell size decreases as the silicon (Si) content increases. However, it is challenging to precisely link the XRD peak position to the exact Si-content due to the presence of a range of solid solutions between compositions of C_3AH_6-$C_3AS_{0.42}H_{5.16}$ and $C_3AS_{0.76}H_{4.48}$-C_3AS_3. Preliminary simulations which considered formation of $C_3AS_{0.8}H_{4.4}$ (i.e., a hydrogrossular phase provided in the standard thermodynamic database for cement hydrates [21]) indicated that the formation of hemicarboaluminate (Hc) would be suppressed in mixtures considered in this study. This finding was in contradiction with our experimental (XRD) data (see below).

To resolve this inconsistency parametric variations of the silicon-content in the hydrogrossular phase were considered (i.e., by interpolating solubility constants, and the density data provided in [102] along the end-members: C_3AH_6-C_3AS_3) until the existence of hemicarboaluminate (Hc) was satisfied in relevant systems. The formation of a hydrogrossular-type phase with a (presumed) composition of $C_3AS_{0.02}H_{5.96}$ was predicted for systems containing MET and CAC2. In the case of HA and CAC1 containing mixtures, the silica content in the hydrogrossular phase were found to range between 0.015-and-0.100 (molar units) respectively. While this is admittedly a trial-and-error means of designating phase equilibria, this choice was made to ensure consistency between the simulations, and the experimental phase analysis. It should be clarified, the thermodynamic properties (Gibbs free energy of formation) of the hydrogrossular phases as calculated herein, are sensitive to composition. Therefore, the compositions identified, are approximate at best [102].

When magnesium is present, hydrotalcite-type phases, which can demonstrate multiplicity in ion uptake, are stabilized [103,104]. While OH-hydrotalcite is often observed [105,106,107] (e.g., in slag bearing cementitious system), in the presence of excess carbonate, it is possible that the CO_3-hydrotalcite phase (i.e., in addition to the CO_3-AFm variants) would form. Preliminary simulations carried out under conditions of excess $Ca(OH)_2$ indicate that, OH-hydrotalcite forms in preference to CO_3-hydrotalcite, independent of the presence, or absence, of calcite. Therefore, within the scope of thermochemical data presently available, OH-hydrotalcite (M_4AH_{10}) is the only phase that is assumed to form but it is possible, and indeed likely, that in the real cement systems hydrotalcite-type phases substituted with other ions may also precipitate.

All calculations were carried out applying a progressive equilibrium approach which enabled to account for fractional reactivity (i.e., incomplete reaction) of each of the components: (1) OPC,

(2) aluminous source and (3) limestone. The amount of OPC reacted was set to be 86 ± 5 % and 91 ± 5% after 28 and 90 days of hydration respectively, as determined using QXRD analyses, across all mixtures. TGA analysis of the anhydrous OPC showed calcite contents of ≈ 3.7 %, a value in compliance with the ASTM C150 specification. Once the degree of OPC reaction was fixed, the aluminous materials were let to incrementally "react" with the OPC oxides and the $CaCO_3$ in 10% increments. These types of simulations retain the unhydrated fraction of OPC, while the quantity of the aluminous agent is systematically reduced as it is allowed to take part in hydration.

The GEMS simulations were matched to our experimental data by setting a "match-point" to the portlandite content, as assessed by TGA, for systems containing amorphous aluminous sources (MET and HA). This match point serves as a means to estimate the degree of reaction of these aluminous materials as these systems are not amenable to QXRD-based quantifications. In the case of crystalline aluminous materials (i.e., the CAC's) the degree of aluminous material reacted was established by QXRD, and the match point established directly by Rietveld analysis of residual anhydrous (CAC) phase contents. It should be noted that while quantitative XRD with Rietveld refinement provides accurate values of the residual (or initial) quantities of the crystalline phases, quantifications of less ordered phases such as, C-S-H, Hc and Mc are less precise [[108],[109]]. This is not a limitation of QXRD techniques generally, but rather a result of the nature of measurements, and refinement procedures implemented herein. Furthermore, though the methodology used herein to establish the match-points, varies for the crystalline and amorphous aluminous sources, both provide a means to assess equilibrium phase assemblages for the systems studied.

4.3 Experimental Results and Discussion

Figure 20 shows the compressive strength of the mixtures evaluated in this study after 90 days of hydration as a function of their OPC content (CF). It is noted that the replacement of OPC by a given aluminous source and/or limestone, results in strength reduction. The reductions trace a decrease in the OPC content (i.e., dilution). It is noted that within the resolution of the measured data, there are two clusters, partitioned below, and above the "dilution line". Data lying above the line (e.g. MET additions, and higher levels of HA additions) show beneficial, synergistic effects of changes in the binder chemistry, while data lying below the line (e.g., CAC and quartz, where the latter is used as an inert reference) illustrate compromised binder compositions. The trends show that mechanical properties, in relation to the aluminous source scale as: MET > HA > CAC1 > CAC2 in a descending order. These trends cast a basis of considering the influence of a given aluminous agent on limestone reactions and associated phase balances in cementing mixtures.

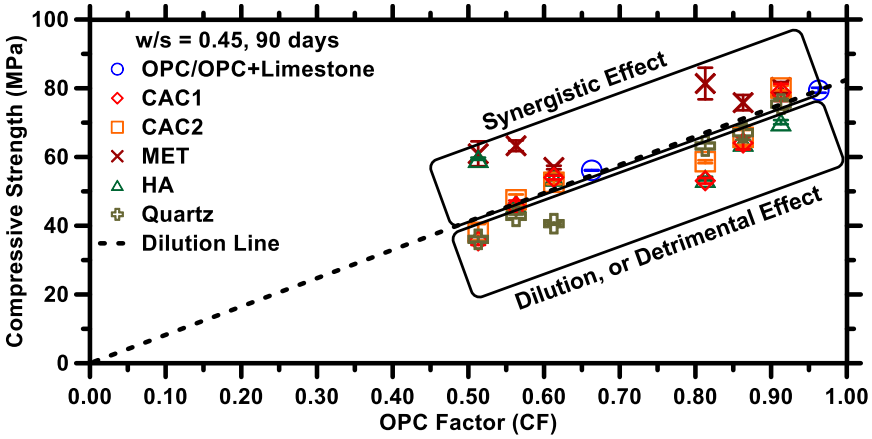

Figure 20: The compressive strength as function of the CF at 90 days, for all the systems studied herein. The dilution line traces the extent of compressive strength reduction that would occur as the OPC content (in terms of mass fraction) was systematically reduced. For the plain OPC formulation, CF = 0.963, given the presence of limestone therein. The error bars shown, indicate the uncertainty in the strength measurements.

4.3.1 Influence of Calcium Aluminate Cement (CAC) Additions

When CAC's are used as an aluminous source, with or without excess limestone (i.e., for $0.53 \leq CF \leq 0.96$), the compressive strength decreases monotonically. In fact, in the presence of the CAC's, the measured strengths are similar to those measured in the presence of quartz; an inert material. This suggests that in spite of their otherwise reactive nature (e.g., when used on their own), CAC additions, do little in terms of improving the mechanical response of OPC-dominated binders. To better understand these trends, Figure 21 shows portlandite contents of blended (OPC + CAC) mixtures, determined by TGA at 90 days normalized by the cement content, to account for OPC replacement. At low levels of OPC replacement, the normalized portlandite content is similar to the reference OPC mixture. However, at higher levels of OPC replacement, a reduction is observed. This suggests either: (a) consumption of portlandite and/or (b) a possible reduction in the extent of OPC reaction.

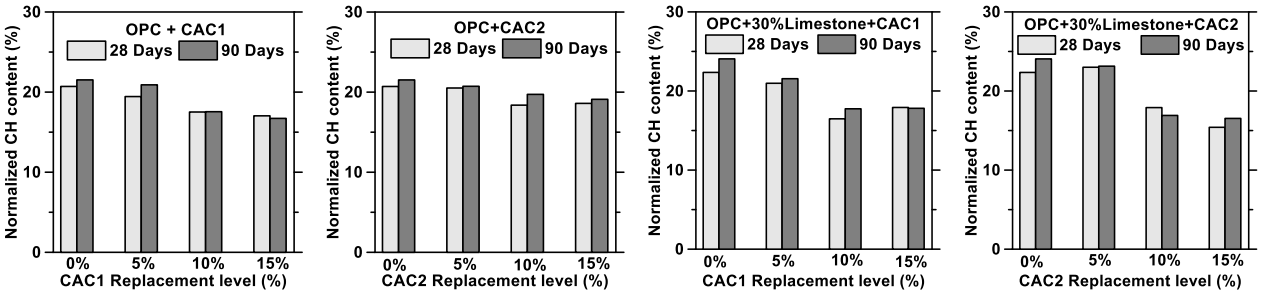

Figure 21: The normalized portlandite contents for cementitious mixtures with varying levels of OPC replacement by: (a) CAC1 and (b) CAC2. (c and d) Show the normalized portlandite contents for mixtures with 30% limestone dosed by replacement of OPC and varying levels of additional replacement by: (c) CAC1 and (d) CAC2. The portlandite contents were determined by thermogravimetric analysis (TGA/DTG) and normalized by the OPC content of a mixture.

Gu et al. [110,111] studied blended binder systems containing OPC and CAC, and concluded that OPC hydration is suppressed only at early ages in sulfate-deficient conditions, i.e., when

aluminum is in excess. Since the title study only evaluates mature systems, such hydration suppression is not expected, a point which is validated by QXRD analysis. Portlandite consumption, on the other hand, seems to play an important role in hemicarboaluminate (Hc) formation. Kuzel [112] showed that in the presence of a carbonate source, C_3A reacts with portlandite (CH) to form AFt and Hc (Equation 19). Matschei et al. [21] additionally noted that coexistence of monosulfoaluminate (Ms) and monocarboaluminate (Mc) in the presence of CH is not possible as the system would stabilize AFt and Hc as shown in Equation (20). This suggests that in the process of forming Hc, portlandite is consumed. This explanation is consistent with our XRD observations, as presented later in this paper (i.e., which confirm Hc formation in the OPC-CAC blends).

$$3C_3A + 3C\bar{S}H_2 + CH + C\bar{C} + 49H \rightarrow C_6A\bar{S}_3H_{32} + 2C_4A\bar{C}_{0.5}H_{12} \quad \text{(equation 19)}$$

$$X(\,C_4A\bar{C}H_{11}) + Y\,(C_4A\bar{S}H_{12}) + Z\,(CH) \rightarrow \frac{Y}{3}(C_6A\bar{S}_3H_{32}) + \frac{2}{3}(X+Z)\;\;(C_4A\bar{C}_{0.5}H_{12}) + \frac{Z}{3}\;CH \quad \text{(equation 20)}$$

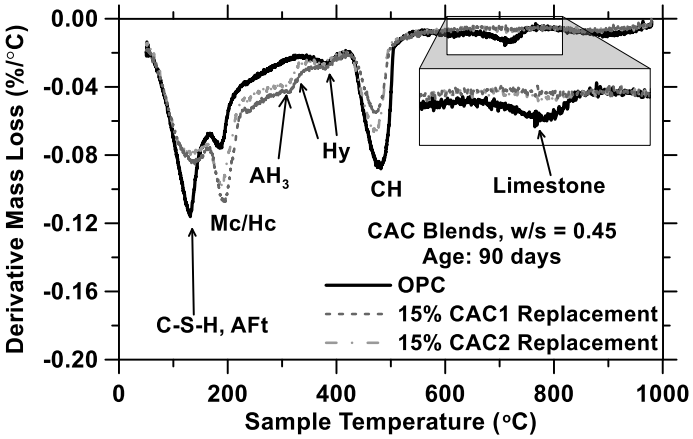

Figure 22: Representative DTG traces for the neat OPC mixture and systems wherein 15% (by mass) of the OPC is replaced by either CAC1 or CAC2, respectively.

If reductions in the portlandite content are related to the formation of Hc, such formation should be accompanied by a reduction in $CaCO_3$ content. Figure 22 shows DTG curves for neat OPC, and systems containing 15% CAC1 or 15% CAC2 after 90 days of hydration under limestone deficient conditions. It can be seen that independent of the type of CAC used, the CH and $CaCO_3$ contents decrease, which is accompanied by an increase in the peak area (quantity) corresponding to the carbonate-AFm (Mc/Hc) phases. A small amount of a hydrogrossular phase $Ca_3Al_2(SiO_4)_{3-x}(OH)_{4x}$ is also detected. It is important to note that decomposition temperatures for the hydrogrossular phases (Hy) range between 315-to-360˚C as the Si-content alters decomposition temperatures [102]. A quantity of AH_3 was identified by TGA (but not XRD or GEMS calculations) and is believed to precipitate to allocate the excess aluminum present in the system. The lack of x-ray reflections (and GEMS prediction) associated with AH_3 is estimated to be on account of its poor crystallinity [113], and/or a non-stoichiometric composition which would result in untabulated thermochemical (solubility) data and thus lack of means to consider this phase in the calculations.

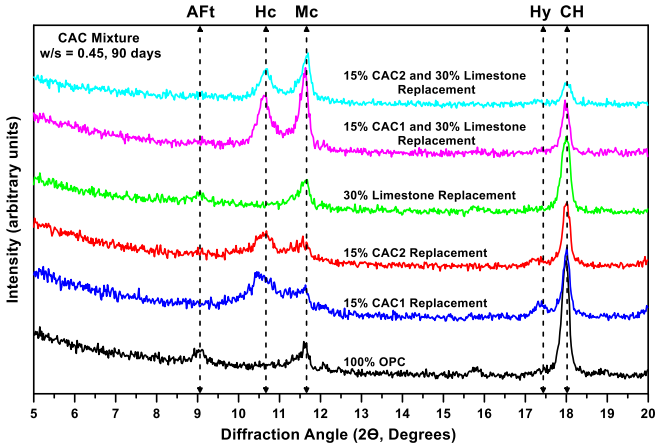

Figure 23: Representative XRD patterns for the plain OPC, limestone enriched (30% OPC replacement by limestone) and CAC enriched mixtures composed for limestone deficient and excess conditions. Here: Hc (hemicarboaluminate), Mc (monocarboaluminate), CH (portlandite), AFt (ettringite) and Hy (hydrogrossular). All enrichments are carried out by replacement of OPC by an aluminous source, and/or limestone.

Figure 23 shows XRD patterns for the neat OPC mixture, the mixture in which 30% of the OPC is replaced by fine limestone, and OPC-CAC blends for limestone deficient (i.e., with only limestone intrinsic to the OPC) and excess conditions respectively, after 90 days of hydration. It is noted that Mc is the only CO_3-AFm phase present in the neat OPC mixture, and OPC mixture in which 30% of the OPC is replaced by limestone. On the other hand, both the OPC-CAC and OPC-CAC-limestone blends show the presence of Hc, in addition to Mc in all mixtures. While Hc is dominant in the former, Mc is dominant in the latter. These observations are in agreement with previous studies in which Mc is noted to be dominant in limestone excess compositions [76,98,99,114,115,116].

In CAC systems containing a small quantity of limestone, (i.e., with no additional limestone added), Hc exists as the major AFm phase. This becomes more pronounced for higher CAC contents, (i.e., ≥ 10% by mass of binder), given the aluminum-rich and the carbonate deficient nature of these systems (e.g., $0.086 < CO_2/Al_2O_3 < 0.154$, mass ratio). In spite of the passage of time, a substantial quantity of unreacted limestone is present in systems that contain excess limestone. Based on QXRD analysis at 90 days, only around 20%-to-36% of the limestone initially present, had reacted in the excess limestone-CAC systems, with increasing limestone consumption for higher levels of CAC (15%) in the binder. Limestone consumption ranged between 21%-to-27% as assessed by TGA at 90 days. It should be noted that the portlandite content reduces as the CAC content in the binder is increased, an observation which is consistent with the increase in Hc formed in the system. The main diffraction peak corresponding to AFt, predicted to exist in excess limestone conditions (as seen in the thermodynamic simulations), is likely diminished due to the nature of the solvent exchange procedure (using IPA) used to arrest hydration – which is known to reduce the crystallinity of the AFt phase.

Strätlingite is not observed in any of the studied systems, based on lack of x-ray reflections. Given the presence of portlandite, it is unlikely that these two phases would coexist [117,118], though this condition is not strict, and a strätlingite precursor of poor-crystallinity may well exist herein [119]. The CACs themselves show different levels of reaction, with CAC1 (at 15% dosage, by mass) showing a degree of reaction on the order of 86.6% and 100% by 90 days for the deficient and excess limestone blends respectively. On the other hand, CAC2 never exceeds 59% reaction even under excess limestone conditions. This is because, in anhydrous form, CAC2 contains 48% Al_2O_3 (corundum), a substance which remains inert in cementitious environments [82]. The difference in the degree of reaction of CAC1, whether or not excess limestone is present is associated with water availability, which would be higher in the latter, than former case (e.g., see [58] for the effects of water availability on CAC hydration). These are indications of how the nature of the aluminum source and not just the aluminum content itself is relevant in favoring carbonaceous reactions.

To better explain the experimental data, thermodynamic simulations were carried out by fixing the degree of hydration (DoH) of the OPC, and incrementally allowing the CAC to react. Figure 24 shows volumetric phase assemblages calculated using GEMS for binder systems containing OPC + 15% CAC1 or OPC + 15% CAC2 (by mass) in limestone deficient or limestone excess conditions. In systems containing only OPC and CAC (and limestone intrinsic to the OPC, but not additional limestone), Hc is the dominant AFm phase that exists, though a smaller quantity of Mc may also coexist. The hydrogrossular phases are predicted to exist only in limestone deficient systems. As expected, the limestone intrinsic to the OPC is fully consumed for the degree of CAC reaction relevant herein. These observations are in agreement with the XRD and TGA data (Figures 22-23).

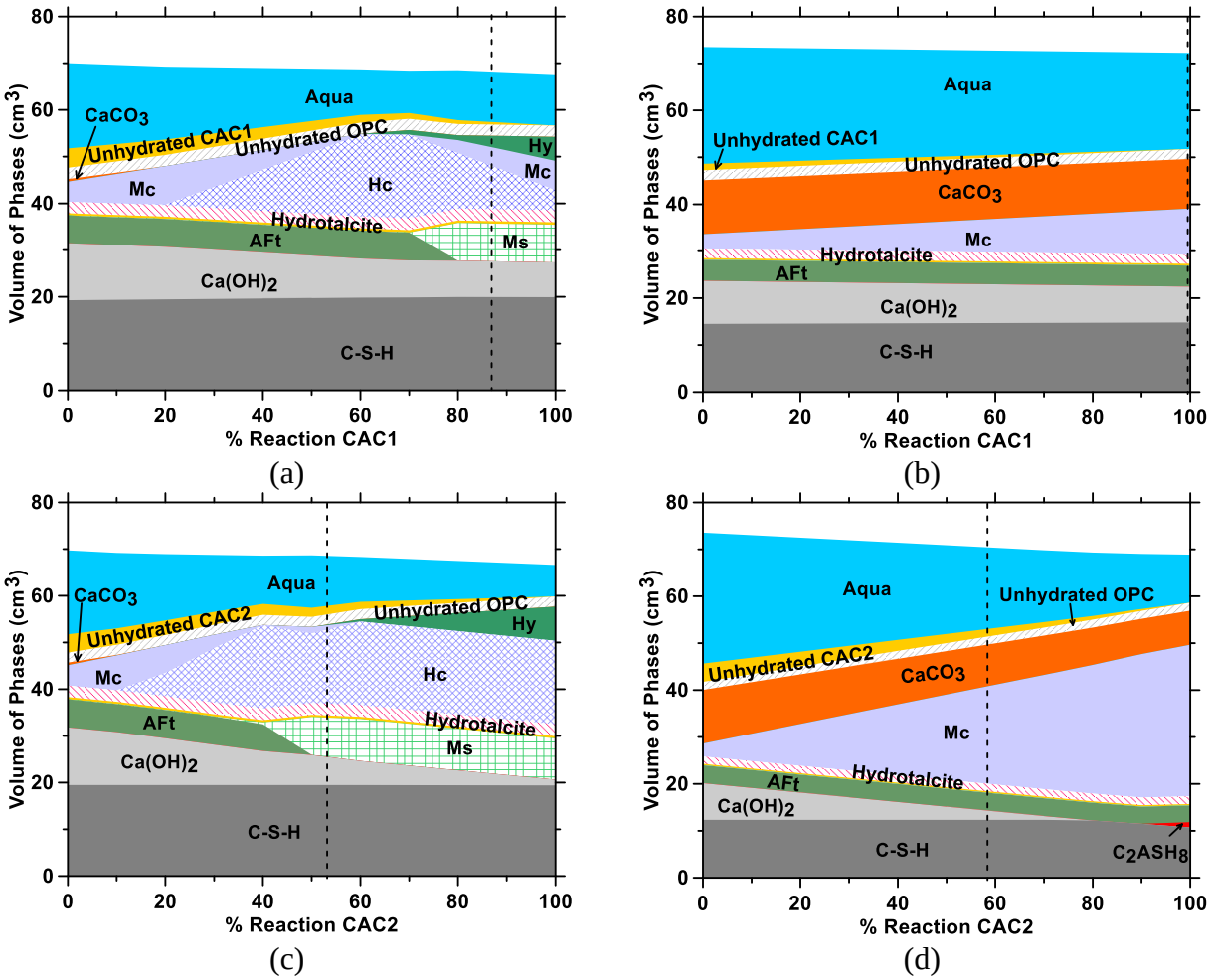

Figure 24: Phase assemblages estimated using GEMS for: (a) 15% CAC1 replacement, (b) 15% CAC1 and additional 30% limestone replacement, (c) 15% CAC2 replacement and (d) 15% CAC2 and additional 30% limestone replacement. All replacements were carried out by reducing the quantity of OPC on a mass basis. Monosulfoaluminate (Ms), ettringite (AFt), monocarboaluminate (Mc), hemicarboaluminate (Hc), strätlingite (C_2ASH_8), hydrogrossular (Hy) and hydrotalcite (M_4AH_{10}) are denoted. The dashed lines locate the estimated phase assemblage after 90 days, based on the degree of CAC reaction as estimated by QXRD.

When excess limestone is present, Mc is predicted to exist, as the singular AFm phase. This is in agreement with experimental data except when excess limestone may be present at larger CAC contents (i.e., around 10 and 15%, by mass). In such cases, Hc and Mc are noted to coexist (see XRD patterns in Figure 23), in contrast to the simulations which indicate the existence of Mc. It is speculated that this happens on the account of slow dissolution of limestone which maintains

$[CO_3^{2-}]/[OH^-]$ levels buffered at a value that is less than optimum for the formation of the Mc exclusively, or the slow kinetics of the Hc-to-Mc conversion. A substantial quantity of unreacted limestone persists in limestone excess systems in spite of a favorable binder chemistry, (i.e., an aluminum, calcium and carbonate ion-rich environment). It is postulated that if the quantity of CAC reacted was hypothetically elevated, notably in the case of CAC2, while the quantity of Mc formed would increase, unreacted limestone would continue to persist. This indicates that while the composition of CACs, and the overall binder, should favor carbonaceous reactions; the reality is different with only a small amount of limestone actually reacting. For example, the TGA data indicates that at most 27% of the limestone available (i.e., around 8.7% of the 32.4% limestone present initially, by mass) reacts in the most favorable case under limestone excess conditions, when a CAC is provisioned as an aluminous source.

Kumar et al. [59] quantified the aqueous dissolution rates of limestone, using vertical scanning interferometry across a range of solution pH's. They observed that the dissolution rate decays with pH, approaching a near horizontal asymptote for pH levels > 12 [59]. This may suggest that the low reactivity (i.e., the dissolution rate) of limestone is likely the rate-limiting step in CO_3-AFm formation. This comment is made as if limestone were indeed readily soluble, the release of the CO_3^{2-} species, and their combination with the Ca^{2+} and $Al(OH)_4^-$ species provided by the CAC (and OPC) would ensure rapid/enhanced limestone reaction. This idea is strengthened by recent observations of a CAC reacting with $Ca(NO_3)_2$, a readily, and highly soluble calcium salt. In this case, the formation of a NO_3-AFm phase is rapid and abundant – unlike the circumstance observed with $CaCO_3$ additions, when the formation of Hc/Mc is far more limited, in spite of excess $CaCO_3$ being present [22,58,120]. Therefore, it appears as though the combination of both, binder chemistry, and the low limestone dissolution rates are responsible for limited CO_3-AFm

(Hc/Mc) formation in blended binder systems. It should be highlighted that for the extent of CAC hydration estimated herein, a Hy (hydrogrossular phase) is predicted to exist in the limestone deficient CAC1 (i.e., 15% CAC1, Figure 24a) system but not in the analogous CAC2 system (Figure 24c) which is in agreement with XRD patterns shown in Figure 23. It is observed that the conversion of AFt into Ms does not occur in systems with excess limestone, whereas in the limestone deficient systems, Ms is stabilized after limestone uptake in Hc/Mc is complete, as recognized previously (see Figure 24a, 24c) [80]. It is important to note that, even though, Ms and AFt are predicted to exist (at varying levels) by thermodynamic calculation, these phases are slightly, if at all, identified by XRD. This is likely on account of the solvent exchange procedure used, which compromises the structure of AFt (rendering it x-ray amorphous [83,121]), and the potential formation of a CO_3-SO_4-AFm ordered compound in lieu of Ms as discussed further in Section 4.3.3.

4.3.2 Influence of Metakaolin Additions

As shown in Figure 20, the replacement of OPC by metakaolin consistently improves strength. Such beneficial effects of metakaolin addition, both with and without excess limestone have also been highlighted by Antoni et al. [90] and Vance et al. [15,122], and attributed to the pozzolanic character of metakaolin, and the formation of the Hc/Mc phases. This is significant in that in spite of very substantial reductions in the CF, mechanical properties near equivalent to the neat OPC mixtures can be achieved in metakaolin containing mixtures. For example, a mixture containing 60% OPC, 10% metakaolin and 30% limestone (CF = 0.58, see Figure 20) shows a compressive strength ≈80% of the neat OPC mixture in spite of 42% reduction in the OPC content.

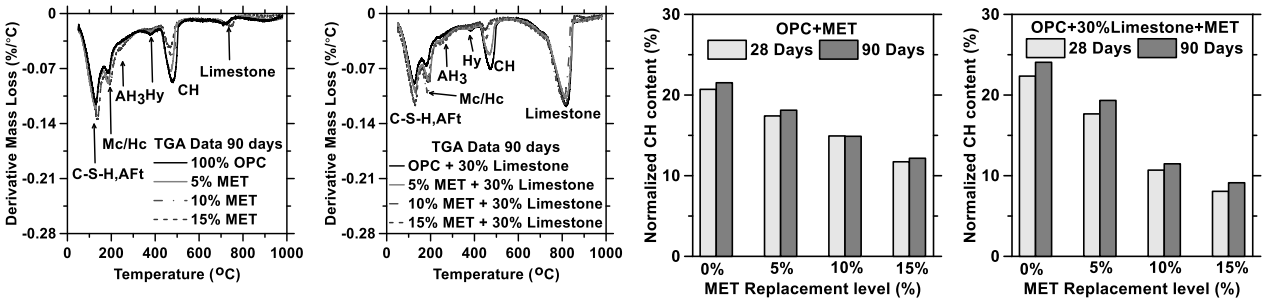

(a) (b) (c) (d)

Figure 25: Representative DTG curves of OPC mixtures for: (a) 0-to-15% MET replacement, (b) 0-to-15% MET replacement with additional 30% of limestone dosed by OPC replacement. The normalized (by CF) portlandite contents for OPC mixtures for: (c) 0-to-15% MET replacement, (b) 0-to-15% MET replacement with additional 30% of limestone dosed by OPC replacement. The portlandite contents were determined by thermal analysis (TGA/DTG). All replacements were carried out by reducing the quantity of OPC on a mass basis.

Figure 25 shows representative DTG traces at 90 days, and the portlandite content normalized by the cement factor (CF) for the metakaolin containing mixtures. It was observed that portlandite contents of a given mixture decrease with increasing OPC replacement by metakaolin, even when dilution is accounted for. This is as expected due to the pozzolanic nature of metakaolin, which consumes lime to form a lower Ca/Si, C-S-H phase. Formation of such additional C-S-H ensures that metakaolin containing mixtures show reduced decreases in their compressive strength, in spite of a substantial level of OPC replacement.

Figure 26 shows XRD patterns for the metakaolin containing mixtures after 90 days of hydration. Mc exists as the dominant phase when excess limestone is added. When only limestone intrinsic to the OPC is present, Mc is stabilized only when metakaolin is absent. When metakaolin replaces OPC, in increasing proportion, Hc is stabilized as the dominant phase. This is in agreement with the observations of Antoni et al. and Vance et al. [15,90]. The contents of the CO_3-AFm (i.e., Hc/Mc) phases, reflect trends in limestone consumption (see Figures 25-26). A higher quantity of the CO_3-AFm's forms with increasing metakaolin content, and when excess limestone is present. While these trends follow evolutions in the equivalent CO_2/Al_2O_3 ratio,

limestone consumption is only partial, once again, likely on account of the low dissolution rate of limestone. In spite of the near consumption of portlandite, (e.g., in the 15% metakaolin mixture containing excess limestone), strätlingite is not observed in the XRD patterns. Small quantities of ettringite are present in both the deficient and excess limestone mixtures, wherein the release of sulfate ions, due to preferred CO_3^{2-} ion uptake into the AFm phase, stabilizes ettringite in these systems.

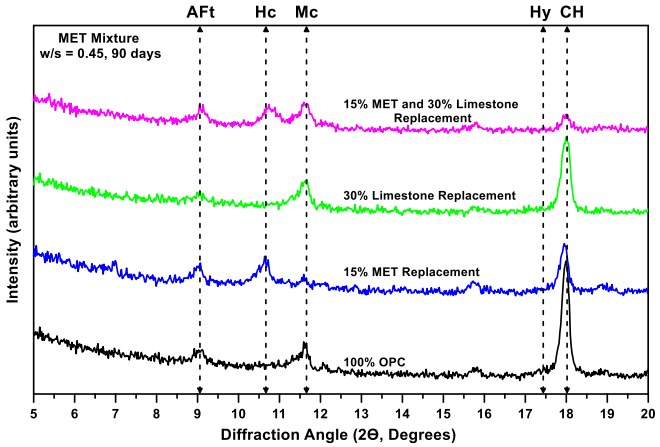

Figure 26: Representative XRD patterns for the plain (100% OPC), limestone enriched (30% OPC replacement by limestone) and MET enriched mixtures composed for limestone deficient and excess conditions. Here: Hc (hemicarboaluminate), Mc (monocarboaluminate), CH (portlandite), AFt (ettringite) and Hy (hydrogrossular). All enrichments are carried out by replacement of OPC.

Figure 27 shows volumetric phase assemblages, calculated using GEMS, for 15% OPC replacement by metakaolin in either limestone deficient or excess conditions. These systems show a degree of metakaolin reaction of 37% and 32%, in limestone deficient and excess cases respectively (see Section 4.2.6 for how the degree of metakaolin reaction is ascertained). The degree of metakaolin reaction is a function of its dosage, wherein lower dosages correspond to higher degrees of reaction. In general, the degree of metakaolin reaction ranges between 32-to-75% as assessed by the portlandite-matching criterion, from higher (15%) to lower (5%) MET

dosages respectively. The simulations are agreement with experimental indications of phase assemblages, except for specific aspects which are discussed further below.

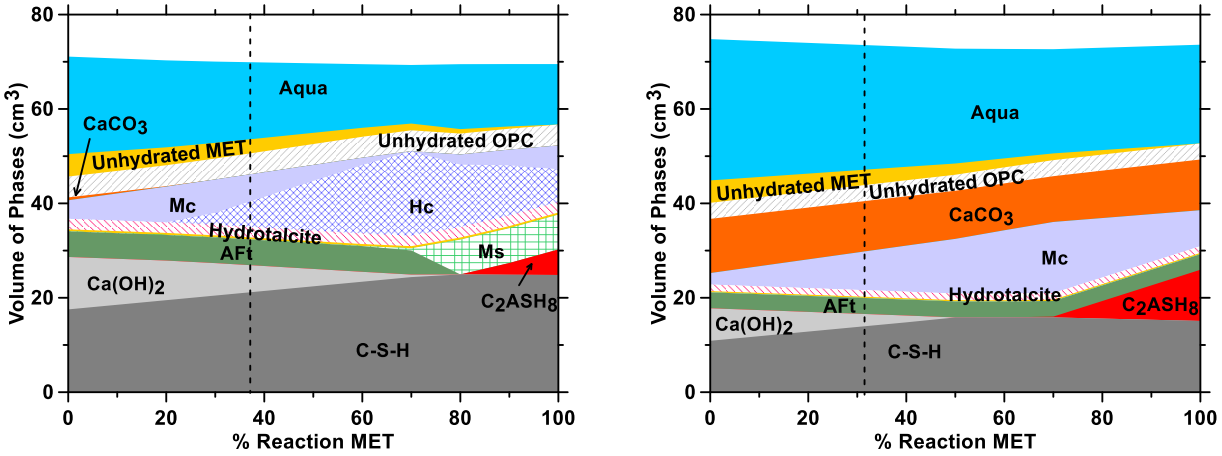

Figure 27: Phase assemblages estimated using GEMS by incremental reaction of MET for: (a) 15% MET and (b) 15% MET and additional 30% limestone replacement of OPC after 90 days of hydration. Monosulfoaluminate (Ms), ettringite (AFt), monocarboaluminate (Mc), hemicarboaluminate (Hc), strätlingite (C_2ASH_8), and hydrotalcite (M_4AH_{10}) are denoted. The dashed lines locate the estimated phase assemblage and MET degree of hydration, after 90 days, based on the portlandite match-point from TGA data as discussed in the text.

In contrast to the other aluminous agents, the pozzolanic nature of metakaolin ensures that its increasing reaction consumes lime and increases the quantity of C-S-H formed, albeit, of a lower Ca/Si ratio [123] and potentially also higher Al-substitution [104,124]. In agreement with XRD data, both C_2ASH_8 and Hy ($C_3AS_{0.02}H_{5.96}$) are not predicted to form for the levels of metakaolin reaction seen in this study. In contrast to these observations, XRD data of Antoni et al. showed the presence of C_2ASH_8 and portlandite coexisting with each other [90]. While this is a violation of thermodynamic phase relations established by Damidot et al. [125], it may be on the account of higher metakaolin contents used in their study, or due to inhomogeneous reaction zones. This discrepancy could however, also be on account of uncertainties in determination of solubility data, small variations in which could alter stability fields dramatically. For example, as noted in

the simulations shown herein (Figure 27), strätlingite is predicted to form only when portlandite is fully consumed due to: (i) pozzolanic reactions, and/or (ii) to form Hc.

When only limestone intrinsic to the OPC is present (see Figure 27a), at low levels of metakaolin reaction, Mc (monocarboaluminate) is stabilized. With the passage of time and with increase in metakaolin reaction, the phase relations change and Hc (hemicarboaluminate) is dominant with Mc existing as the minor CO_3-AFm phase. For the degree of metakaolin reaction ascertained herein, Mc and Hc appear to exist in equivalent volumetric quantities, though by mass this would translate to a larger quantity of Mc (the denser CO_3-AFm phase) [126,127] in contrast to XRD data shown in Figure 26. While this may indicate that the ascertained degree of metakaolin reaction is lower than reality, it may also suggest kinetic restraint in the formation of Hc, from Mc, Ms and portlandite (or vice-versa depending on the environment). When excess limestone is present, Mc is the dominant AFm phase (Figure 27b). This is once again in contrast to the XRD observations in Figure 26, where even under limestone excess conditions, when (15%) metakaolin is present, Hc/Mc coexist; reasons for which are discussed above (Section 4.3.1). For all degrees of metakaolin reaction, a large quantity of limestone remains unreacted, ensuring only modest levels of Hc/Mc formation. This leads to the conclusion that the compensation in the mechanical properties (see Figure 20), produced by the combined replacement of OPC, by both limestone and metakaolin, is dominantly on account of the pozzolanic nature of metakaolin and less so due to the formation of CO_3-AFm phases. This has important compositional impacts on reducing OPC use, and the selection of suitable OPC replacement agents.

4.3.3 Influence of Hydratable Alumina Additions

Blended cementitious formulations containing HA show distinct trends in compressive strength whether or not excess limestone is present. For example: as shown in Figure 20, in the absence

of excess limestone, HA containing mixtures show reductions in strength with increasing HA dosage, lying below the dilution line. However, when excess limestone is present, the trend inverts, with beneficial/synergistic effects of HA additions being noted. For example: mixtures containing 55% OPC, 30% limestone and 15% HA (CF = 0.53) show compressive strengths of ≈70% of a neat OPC formulation, i.e., significantly higher than that would be expected based on their extent of OPC replacement (47% reduction in the OPC content). This strength recovery is on the account of the formation of AFm-type phases and is explained further below.

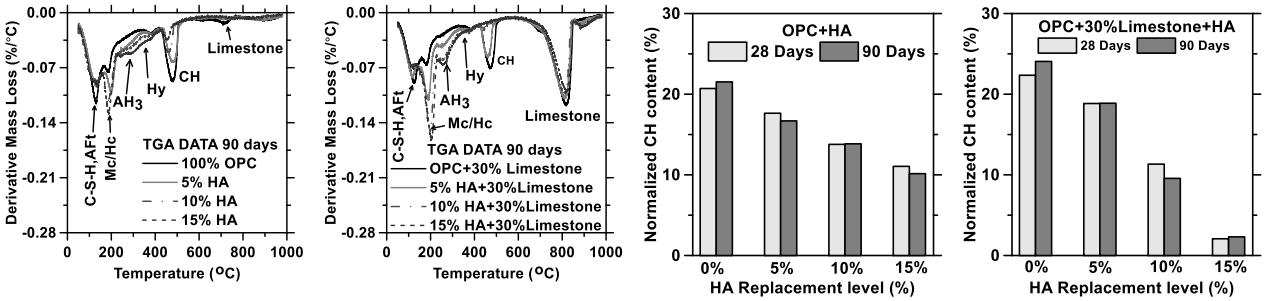

(a) (b) (c) (d)

Figure 28: Representative DTG curves for OPC mixtures for: (a) 0-15% HA replacement, (b) 0-15% HA replacement with additional 30% of limestone dosed by OPC replacement. The normalized (by CF) portlandite contents for OPC mixtures for: (c) 0-15% HA replacement, (d) 0-15% HA replacement with additional 30% of limestone dosed by OPC replacement. The portlandite contents were determined by thermal analysis (TGA/DTG). All replacements were carried out by reducing the quantity of OPC, by HA and/or limestone, on a mass basis.

Figure 28 shows DTG traces of mixtures containing HA, and the portlandite contents of HA-dosed mixtures. The portlandite content is normalized by the cement factor (CF) to account for dilution. Independent of the presence of excess, or low levels of limestone, portlandite content decreases with an increase in the HA content. This is on account of the consumption of portlandite, to form Hc, as noted in the case of CAC-dosed formulations (section 4.3.1). It is important to note that the extent of Hc or Mc formed in HA systems exceeds that of CAC or MET systems, based on TGA, and QXRD estimations. This idea is strengthened by the QXRD

data which reveals no suppression in the OPC reaction, whether or not any HA (or quartz which is an inert filler) is present.

The DTG traces reveal that the addition of HA results in increases in (with increasing HA dosage): (i) the quantity of AH_3 formed, (ii) the quantity of Hc/Mc formed, and a concurrent decrease in the unreacted limestone content and (iii) the quantity of hydrogrossular (Hy) phases formed. This indicates that HA serves as a reactive source of aluminum in such blends. It was determined by TGA quantifications that in limestone excess blends between 24-to-32% of the total limestone initially present (mass basis) is consumed by 90 days. This level of limestone consumption, higher than that noted for the other aluminous agent containing blends (see Figure 32 below), explains the enhanced formation of CO_3-AFm phases (Hc and/or Mc) in HA containing systems.

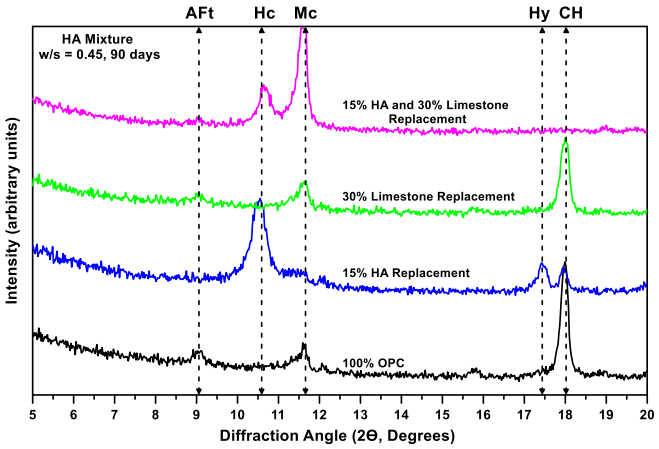

Figure 29: Representative XRD patterns for the plain (100% OPC), limestone enriched (30% OPC replacement by limestone) and HA enriched mixtures composed for limestone deficient and excess conditions. Here: Hc (hemicarboaluminate), Mc (monocarboaluminate), CH (portlandite), AFt (ettringite) and Hy (hydrogrossular). All enrichments are carried out by replacement of OPC by HA and/or limestone, by mass.

XRD observations (Figure 29), in agreement with TGA data, indicate that the portlandite content of a given mixture, in both limestone deficient and excess cases, reduces with HA dosage. In the former case, limestone is near completely consumed by 90 days. But when excess limestone is

present, a quantity of unreacted limestone persists. Mc exists as the dominant CO_3-AFm phase, though in coexistence with Hc in cases when excess limestone is present (Figure 29). When the system is limestone deficient, Mc is stabilized if no HA is added. As the HA dosage increases, Hc is the dominant phase, and is in fact the only carbonate-AFm that exists at 15% HA dosage, as observed also by Whittaker et al. [128]. Abundance of the CO_3-AFm phases (i.e., both Hc and Mc), increases with increments of HA and limestone. While strätlingite is not seen, a hydrogrossular phase is stabilized, especially at higher HA contents in limestone deficient systems. Lack of x-ray reflections for strätlingite, and AH_3 is believed to be due to similar factors as explained in Section 4.3.2. Monosulfoaluminate (Ms) is not seen, perhaps due to the nature of solvent exchange, or the potential formation of a CO_3-SO_4-AFm phase as discussed below.

Baquerizo et al. [129] investigated the water content of Ms when exposed to changes in relative humidity (RH) and temperature and showed that a reduction in RH (i.e., drying) impacts the water content and the interplanar spacing (d) and the position of the main diffraction peak. Such a shift in the main peak of Ms towards higher 2Θ angles potentially caused by solvent exchange (drying) would result in an overlap with the Hc signature. Further, though the literature does not indicate a solid-solution between CO_3-AFm and SO_4-AFm [98], recent studies conducted by Renaudin et al. [130] indicate the existence of new phase, $[Ca_2Al(OH)_6]\cdot[(SO_4)_{1/2-x}\cdot(CO_3)_{x/2}\cdot nH_2O$ (i.e., a CO_3-SO_4-AFm); an ordered compound containing both carbonate and sulfate ions in its structure. Due to the lack of precise structural, compositional and thermodynamic descriptions this phase could not be identified or predicted in the present study. Nevertheless it should not be disregarded as it is believed to have the potential to form and persist. In fact if CO_3-SO_4-AFm did form, its main diffraction peak at 2θ values of ≈11° could: (a) obscure Hc identification as

Hc has a main peak at similar 2θ location or (b) suggest that Hc and Ms formation is prevented at the expense of the CO_3-SO_4-AFm phase, which may indeed be thermodynamically more stable. Figure 30 shows the volumetric phase assemblages predicted by GEMS, for blends containing 15% HA under either limestone deficient, or excess conditions. In these calculations, the degree of OPC reaction is fixed, and the extent of HA reaction varies. Based on the portlandite content determined from TGA data, the HA was assessed to have reacted around 43%, (i.e., which is the lowest degree of HA reaction across the HA dosages considered). The degree of reaction of the HA across all dosages ranges between 43-to-93% and 50-to-63% for limestone deficient and excess conditions respectively. The slight formation of a hydrogrossular phase ($C_3AS_{0.15}H_{5.97}$) is predicted under limestone deficient conditions as shown in Figure 30(a).

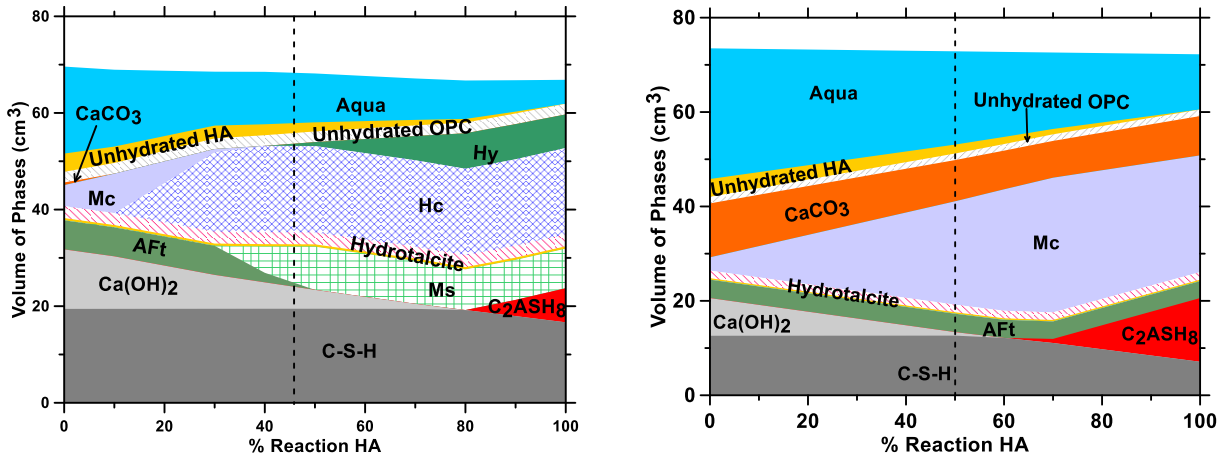

Figure 30: Phase assemblages estimated using GEMS by incremental reaction of HA for: (a) 15% MET and (b) 15%MET and additional 30% limestone replacement of OPC after 90 days of hydration. Monosulfoaluminate (Ms), ettringite (AFt), monocarboaluminate (Mc), hemicarboaluminate (Hc), strätlingite (C_2ASH_8), Hydrogrossular (Hy) and hydrotalcite (M_4AH_{10}) are denoted. The dashed lines locate the estimated phase assemblage and MET degree of hydration, after 90 days, based on the portlandite match-point from TGA data as discussed in the text.

The simulations highlight that with increasing HA dosage and its reaction, Hc becomes dominant with Mc existing as the minor CO_3-AFm phase. In the presence of excess limestone and HA, Mc

is estimated to be the dominant (and singular) AFm phase (Figure 30b); but without Hc being predicted to coexist. This finding is contrary to the XRD data (see Figure 29). This discrepancy, i.e., of Hc/Mc coexistence is explained on the basis of the slow dissolution kinetics of limestone, and potentially kinetic restraints on Hc-to-Mc phase conversion. It is additionally speculated that with increasing HA dosage, the presence of Hc may also be a consequence of the large supply of aluminate ($Al(OH)_4^-$) species, which serve in a charge balancing role, and therefore suppress CO_3^{2-} abundances in solution; ensuring the precipitation of Hc, at the expense of Mc [131]. Substantial quantities of $Al(OH)_4^-$ are ensured by the high pH of pore solution, the soluble Na_2O content in HA, and its amorphous nature, which renders it amenable to dissolution [132]. In time, as the system converges to thermodynamic equilibrium, Hc, is expected to convert to Mc, given the higher stability of the latter as compared to the former. While a large quantity of limestone remains unreacted in the excess limestone systems (Figure 30b), per unit of OPC replacement, clearly, HA is most efficient at provoking CO_3-AFm phase formation. This supports the idea that unlike for metakaolin where the pozzolanic reaction allows for compensation in mechanical properties, when HA is added, it is the formation of CO_3-AFm's and accompanying phases (e.g., hydrogrossular) that enables strength recovery [133]. This supports the original premise that so long as limestone can be rendered reactive the favorable properties of the CO_3-AFm phases can be exploited to ensure near similar engineering properties (strength) as traditional OPC systems [11,15,29,134]. This suggests an important direction of future research, i.e., to identify new means to enhance the reactivity of limestone in cement systems, by mechanical or chemical activation.

4.4 Correlating Phase Balances to Mechanical Properties and Comparing Aluminous Agents

To better correlate microstructural indicators to compressive strength, the coarse porosity (i.e., volume fraction of pore solution, at a given degree of reaction, relevant at 28 and 90 days) was

estimated from the GEMS simulations [24,88,135]. The values of porosity thus determined were used to construct strength-porosity plots, for both the MET and HA systems. These two systems were chosen as they rendered the most promising results in terms of "strength similarity" as compared to the neat OPC formulation (i.e., with and without added limestone). Expectedly, the strength reduces with increasing porosity (i.e., decreasing CF). As seen in Figure 31(a), the MET and HA mixtures follow two distinct trend-lines wherein at any given porosity value, HA systems show a strength which is consistently ≈18% lower when compared to similar MET systems. This indicates that the solid (C-S-H) phases that are formed in MET systems, and the nature of their bonding is superior to HA systems from a compressive strength point of view.

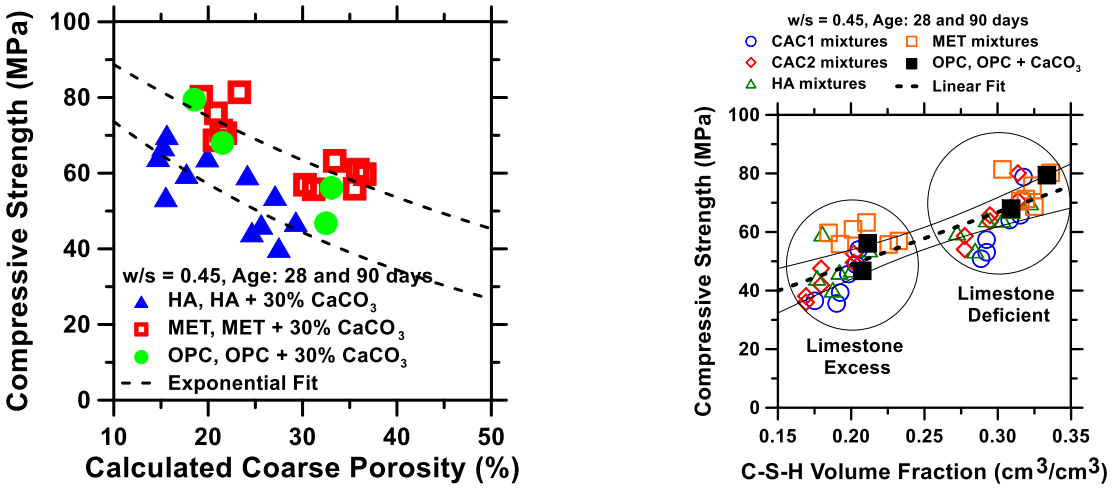

(a) (b)

Figure 31: (a) Calculated strength-porosity trends for cementitious blends containing HA or MET at 28 and 90 days of hydration and (b) The strength as a function of the C-S-H volume fraction for all the cementitious blends considered in this study.

More detailed analysis of the simulation datasets suggests that difference in strengths is directly linked to the amounts of C-S-H present in the system, e.g., with a linear correlation between C-S-H quantity and strength being observed (Figure 31b). This suggests that while the formation of the CO_3-AFm phases is able to offset the effects of dilution – strength recovery is partial at best. This is because in spite of their attractive mechanical properties [133,136], the CO_3-AFm phases

are not able to provide the same mechanical performance as the C-S-H phase; albeit of varying Ca/Si (molar) ratios. Therefore, in the context of cement factor (CF) reduction, it is safe to say that the most effective (and practically easiest) means lies in joint substitution of OPC by a pozzolanic and aluminous agent, (e.g., metakaolin). It is important to note that since this study has evaluated only pastes, (i.e., mixtures devoid of fine or coarse aggregates), the influences of a pozzolanic agent on strengthening the ITZ are not accounted for. This may suggest that in mortars and concretes, where the ITZ is present, the benefits of pozzolan addition (e.g., in the context of compressive strength enhancement), would likely be additive to the effects noted above.

To evaluate the ability of different aluminous agents to enhance limestone reactions, Figure 32 compares the quantity of limestone consumed, for a given dosage of an aluminous agent. It was found that the extent of limestone consumed scales in the order HA > CAC1 > CAC2 > MET. This trend is broadly correlated to the Al_2O_3 content available in these aluminous sources. Expectedly the quantity of Hc and/or Mc formed follows the same order, wherein MET produces the least quantity of CO_3-AFm phases, and HA, the largest quantity (Figure 33). It is noted that limestone consumption shows a pessimum-type effect, where intermediate dosages of the aluminous agent induce the largest (relative) extents of limestone consumption; after which a plateau in limestone consumption (for HA) or decrease is noted (for CAC1, CAC2, MET); as shown in Figure 32. This suggests that simply increasing the aluminous agent dosage does not ensure an increase in the extent of limestone reaction – but rather it depends on the type of aluminous source that is used.

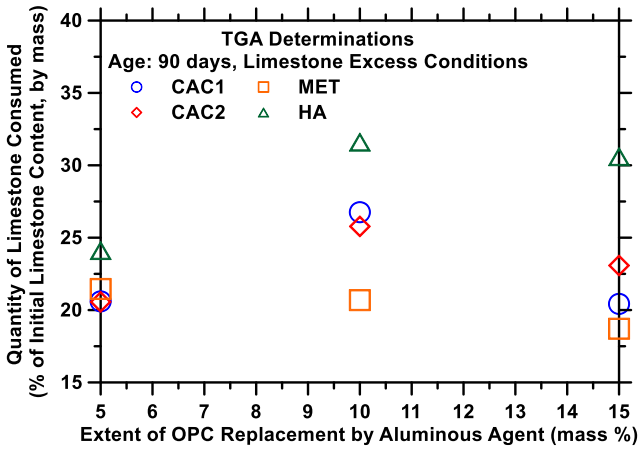

Figure 32: The quantity of limestone consumed as a percentage of the initial quantity of limestone present (mass basis) in excess limestone systems as evaluated using thermogravimetric analysis for the range of aluminous sources considered in this study.

It should be also highlighted that under limestone excess conditions across all aluminous agents considered, a clear thermal decomposition peak for AH_3 is revealed. This indicates that the initial dissolution of limestone may not be fast enough to supply CO_3^{2-} ions in a quantity required to ensure the continued formation of Mc. As a consequence, Hc forms and equilibrium is established between solution, and solid phases as dictated by the $[CO_3^{2-}]/[OH^-]$ ratio. Once this new solubility equilibrium (i.e., with respect to Hc) is established, given the presence of Ca^{2+}, AH_3 (or its non-stoichiometric variants) and hydrogrossular phases of variable silicon content also form so as to absorb the excess aluminum species in the solution. That action is necessary to accommodate "excess aluminum" from the solution and is unsurprising given that Al-equilibrium in these systems is established with respect to the AFm/AFt phases, which show very slight aqueous solubility, and very low abundances of Al-species (in the µmol/L range [131]). The lack of observation of AH_3 by XRD, is explained on account of its poor crystallinity. This reasoning is supported by DTG traces shown in Figure 33 which show higher quantities of hydrogrossular when limestone is deficient (i.e., provided by OPC only) and, AH_3 when limestone present in excess. These trends are strictly linked not to the quantity of limestone

present, but also the CF, wherein a higher CF (larger OPC, and silica content) supports the formation of hydrogrossular phases, and a lower CF (lower OPC content) ensures the formation of AH_3 like phases (see Figure 33). While it is acknowledged that the uptake of aluminum into the C-S-H phases will vary with the binder chemistry (e.g. Ca/Si ratio) and the abundance of aluminum in solution [104,124,137], it is not accounted for in this study due to lack of comprehensive thermodynamic data which describes the nature and extent of Al-uptake by the C-S-H as a function of its composition.

4.5 Summary and Conclusions of Chapter 4

A series of aluminous materials were evaluated in blended binder formulations in terms of their ability to enhance the reaction of limestone in cementitious systems. Such enhancements in limestone reaction are provoked by systematic manipulation of the binder chemistry (e.g., in terms of the SO_3/Al_2O_3 and CO_2/Al_2O_3 ratios of the binder). It is noted that in spite of the provision of sufficient aluminum, calcium and water, the extent of limestone reacted is somewhat limited. This is linked dominantly to the low reactivity (i.e., dissolution rate, and solubility) of limestone. Out of all aluminous agents considered in this study, a hydratable alumina (HA) is noted to be the most successful in enhancing limestone reaction, and the formation of the CO_3-AFm (Hc and/or Mc) phases. On the other hand, metakaolin on account of its pozzolanic nature is most effective in ensuring strength equivalence, or improvement (in spite of reductions in the OPC content) as compared to the neat OPC formulations. Calcium aluminate cements, in spite of their substantial aluminum content are modestly, if at all, capable of enhancing limestone reaction. This suggests a significant role of the nature and the type of aluminum source (i.e., and not simply its aluminum content) in terms of its ability to enhance limestone reactivity in OPC-based binder systems.

The conclusions are supported by a detailed multi-method experimental study, and supporting thermodynamic calculations. In general, thermodynamic simulations are able to reliably describe hydrated phase balances except for discrepancies noted in the stability of Hc, and AH_3 in select aluminum-enriched systems, under conditions of limestone excess. This is likely on account of the slow dissolution kinetics of limestone, and potential kinetic restraint in the conversion of Hc to Mc. It is noted that the formation of the Hc consumes portlandite. While this is typically not problematic, if the aluminous agent were to be substantially reactive (e.g., HA) and present in a high enough dosage under conditions of limestone excess, this would result in the hydrated binder entering a "portlandite-deficient" condition. This aspect would need careful consideration given the role of the portlandite in buffering the pore solution pH – an action which prevents the decalcification of the C-S-H, and ensures reinforcing steel passivation.

Chapter 5: The Influence of Slightly, and Highly Soluble Carbonate Salts on Phase Relations in Hydrated Calcium Aluminate Cements

5.1 Scope of Chapter 5

Previous chapters of this document have described the different effects of limestone use in cementitious systems (OPC and CAC). As described in chapter 4, one of the possible reasons for limited limestone reaction partake in cementitious systems can be it low solubility and slow dissolution rate. Chapter 5 focusses on bypassing this inconvenience by provision of a highly soluble carbonate salt (Na2CO3) in CAC systems. As a means of comparison limestone is provided in the same replacement levels.

The primary reactive compounds in CACs include monocalcium aluminate $CaO{\cdot}Al_2O_3$ (CA) and gehlenite $2CaO{\cdot}SiO_2{\cdot}Al_2O_3$ (C_2AS). Since C_2AS is slightly reactive at ambient temperatures, most studies simplify the hydration of CACs as the reaction of CA with water [138]. In water-rich systems (i.e., when w/c > 0.50, w/c: water-to-cement ratio, by mass) at ambient temperatures (T < 30°C), CACs hydrate to form CAH_{10}, C_2AH_8 and AH_3 as the initial ("early") hydration products (equations 21-23). The two former hydrates are termed as "metastable", as in time they transform to C_3AH_6 which coexists with AH_3, and strätlingite phases at "mature" times [104]. Since this nature of phase transformations involves the expulsion of water from the solids, the resulting accumulation of water in the microstructure results in an increase in porosity, and a detrimental reduction in the mechanical properties [139,140,141]. This process is termed as "conversion" [20].

Recently, Falzone et al. [58], showed that the reaction pathway involving the formation of the metastable hydrates (i.e., CAH_{10}, C_2AH_8) and their conversion to C_3AH_6 can be bypassed by the

addition of calcium nitrate ($Ca(NO_3)_2$). This is due to the formation of the NO_3-AFm phase, which acts to circumvent/bypass the conversion process.

$$CA + 10H \rightarrow CAH_{10} \quad \text{(equation 21)}$$
$$2CAH_{10} \rightarrow C_2AH_8 + AH_3 + 9H \quad \text{(equation 22a)}$$
$$2CA + 11H \rightarrow C_2AH_8 + AH_3 \quad \text{(equation 22b)}$$
$$3C_2AH_8 \rightarrow 2C_3AH_6 + AH_3 + 9H \quad \text{(equation 23a)}$$
$$3CA + 12H \rightarrow C_3AH_6 + 2AH_3 \quad \text{(equation 23b)}$$

It is postulated that similar to calcium nitrate, limestone and sodium carbonate, due to their ability to provision CO_3^{2-} ions, and the potential to stabilize the CO_3-AFm compounds (i.e., monocarboaluminate, Mc and hemicarboaluminate, Hc as shown in Eqs. 24-26) should also be able to prevent conversion [21,112]. Based on this concept, Luz and Pandolfelli [22] showed that the addition of $CaCO_3$ to CAC's does result in the formation of the carboaluminate phases which can somewhat inhibit phase conversion. However, recent studies have shown that the reaction of limestone with CAC's is kinetically hindered in spite of being thermodynamically favored [142]. It is therefore postulated that for carboaluminate phase formation to be enhanced, a carbonate source with high solubility, and fast dissolution, (i.e., a soluble carbonate salt similar to $Ca(NO_3)_2$), needs to be provisioned. Based on this idea, this study examines the influences of two carbonate salts of low (limestone, $CaCO_3$) and high solubility (sodium carbonate, Na_2CO_3) on hydrated phase relations in CACs. The role of water availability is discussed in terms of impacts on carboaluminate phase formation. Special focus is paid to understand if the supply of a suitable carbonate source can indeed suppress phase conversion reactions in calcium aluminate cements.

$$3CA + C\bar{C} + 17H \rightarrow C_4A\bar{C}H_{11} + 2AH_3 \quad \text{(equation 24)}$$

$$C_3AH_6 + C\bar{C} + 5H \leftrightarrow C_4A\bar{C}H_{11} \quad \text{(equation 25)}$$

$$C_3A + 0.5C\bar{C} + 0.5CH + 11.5H \rightarrow C_4A\bar{C}_{0.5}H_{12} \quad \text{(equation 26)}$$

5.2 Materials and Methods

A commercially available grey calcium aluminate cement (CAC) Secar 51 that is produced by Kerneos Aluminate Technologies was used. The oxide composition of the CAC as determined by X-ray Fluorescence (XRF) in mass % was: 4.9 % SiO_2, 52.1 % Al_2O_3, 2.3 % Fe_2O_3, 39.8 % CaO, 0.60 % MgO, 0.07 % Na_2O and 0.31 % K_2O. The mineralogical (phase) composition of the CAC as determined from Rietveld analysis of its x-ray diffraction patterns in mass % was: 73.3 % CA, 18.1 % C_2AS, 4.9 % CT, 1.5 % C_3FT, 0.6 % C_2F, 0.8 % CaO and 0.8 % Fe_2O_3. A nominally pure limestone powder (>95% $CaCO_3$) was sourced from OMYA A.G. Analytical reagent grade sodium carbonate was purchased from Sigma Aldrich (CAS Number: 497-19-8).

A series of cementitious mixtures (Table 10) were prepared using de-ionized (DI) water at 3 different water-to-solid ratios (w/s = 0.40, 0.45 and 0.70, by mass) as described in ASTM C305 [[13]]. In samples where CAC was replaced by limestone, the CAC and limestone were "dry mixed" prior to the addition of water. For blends where CAC was replaced by sodium carbonate; sodium carbonate was dissolved in water, and the CAC was then mixed into this solution. It should be noted that the w/s listed corresponds to the water-to-solids (i.e., CAC, sodium carbonate and limestone) ratio on a mass basis. The replacement of CAC by a carbonate source alters the: (a) equivalent carbon dioxide to aluminum oxide ($CO_{2\text{-}eq}/Al_2O_3$) ratio, (b) calcium to aluminum oxide (CaO/Al_2O_3) ratio, and, (c) equivalent carbon dioxide to calcium oxide ($CO_{2\text{-}eq}/CaO$) ratio (all on a mass basis). Trends in these ratios as a function of CAC replacement level are shown in Figure 33.

Table 10: An overview of the cementitious formulations used in this study.			
Mixture ID	**w/s**	**Replacement by $CaCO_3$ (%)**	**Replacement by Na_2CO_3 (%)**
SEC	0.45	0	0
10LSEC	0.40, 0.45, 0.70	10	0
30LSEC	0.45	30	0
50LSEC	0.45	50	0
10NSEC	0.40, 0.70	0	10
30NSEC	0.70	0	30

The particle size distributions (PSDs, Figure 33d) of all the solids were measured using a Beckman Coulter Static Light Scattering Analyzer (LS13-320). Powders were dispersed to their primary particles by sonication in isopropanol. The uncertainty in the light scattering analysis was around 6% based on six replicates and assuming the refractive index of the CAC, limestone and anhydrous Na_2CO_3 to be 1.7, 1.69 and 1.535 respectively [143].

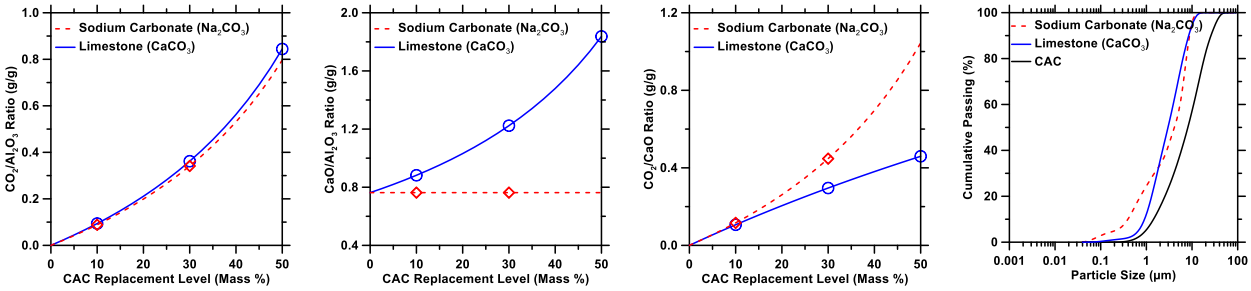

(a) (b) (c) (d)

Figure 33: (a) Carbon dioxide equivalent-to-aluminum oxide ($CO_{2\text{-eq}}/Al_2O_3$), (b) calcium-to-aluminum oxide (CaO/Al_2O_3), and, (c) carbon dioxide equivalent-to-calcium oxide ($CO_{2\text{-eq}}/CaO$) mass ratios as a function of the CAC replacement level for each carbonate source. (d) The particle size distributions (PSDs) of the solid reactants used in this study.

The compressive strength of the w/s = 0.45 mixtures (see Table 10) was measured at 1, 3, 7, 28 and 90 days using cubic specimens (50 mm x 50 mm x 50 mm) cured at 25 ± 1°C in lime water as described in ASTM C109 [13]. The strength reported is the average of three specimens cast from the same mixing batch.

X-Ray diffraction (XRD) patterns were obtained on finely powdered samples at desired ages using a Bruker-D8 Advance diffractometer in a θ-θ configuration using Cu-Kα radiation (λ = 1.54 Å). The samples were scanned between 5° and 70° (2θ, degrees) in continuous mode with an integrated step scan of 0.017° (2θ, degrees) using a VANTEC detector. The total time required for acquisition of the X-ray diffraction pattern was around 12 minutes. A fixed divergence slit of 0.50° was used during data acquisition. Care was taken to minimize preferred orientation errors by texturing the surfaces of the sample. Information on the X-ray structures of anhydrous and hydrated crystalline phases was sourced from standard databases (ICDD [144]) or the literature [145]. The anhydrous CAC was analyzed using a protocol described by Le Saout et al [85].

A Perkin Elmer STA 6000 simultaneous thermal analyzer (TGA/DTG/DTA) equipped with a Pyris data acquisition interface was used to identify and quantify solid phases present in the cementitious mixtures. The temperature and mass sensitivity of this instrument is ±0.25°C and ±0.1 μg respectively. To arrest hydration, solvent exchange was performed using isopropanol wherein at a desired age, hydrated pastes were crushed to a size less than 5 mm and submerged in isopropanol for fourteen days, with isopropanol being replaced every seven days. Following such solvent exchange, samples were placed under vacuum in a desiccator to remove the solvent for another seven days. During measurement, powder samples were placed in pure aluminum oxide crucibles under the UHP-N_2 purge at a flow rate of 20 ml/min and heated at a rate of 10°C per minute over a temperature range from 35-to-975°C. The weight loss (TG) and differential weight loss (DTG) patterns acquired were used to quantify the amount of $CaCO_3$ present in the system. It should be noted that the quantity of $CaCO_3$ is presented as a percentage of the phase present per dry mass of paste (% dry mass).

5.3 Thermodynamic Calculations: Prediction of Hydrated Phase Assemblage

Thermodynamic calculations were carried out using a geochemical speciation program, GEMS-PSI, Gibbs Energy Minimization Software, ver. 2.3 [146]. GEMS-PSI uses the initial mixture proportions represented in the form of the simple oxides present in the solid precursors and the water content, as inputs, and applies a convex programming approach in conjunction with data of the thermodynamic properties of phases (solids, liquid and air) to compute equilibrium phase balances and ion-speciation in a multicomponent system. The input oxide composition of the CAC was obtained from the XRF data. To simulate different levels of CAC reaction, the oxides present in the CAC were allowed to react in incremental steps of 10 %, from 0-to-100 % reaction with the total amount of water and carbonate source present. It should be noted that this approach does not consider the kinetics (i.e., the rate of reaction of the different phases in a CAC). Rather, it seeks to understand the evolution of phase balances with increasing reaction extent – assuming that in any given reaction step – the reactants are completely transformed to suitable products; to minimize the free energy. Thus, this "fractional reaction" approach elucidates the development of hydrated phases in the style of a step-wise reaction sequence [147,148,149].

Thermodynamic data of solid and aqueous species were sourced from the built in GEMS-PSI (NAGRA) database of minerals, and amended with additional data relevant to cementitious systems as embedded in the CEMDATA07 database [57,93,94,150,151]. The thermodynamic database was further expanded to consider gaylussite and thermonatrite as these phases were found to exist in Na_2CO_3 bearing blends [152] (see Table 2). Natron was also included to determine if this phase has a potential to form, and persist in blends containing higher Na_2CO_3 contents. The Gibbs free energy ($\Delta_f G^0$) of formation at T = 25°C and p = 1 bar along with other thermodynamic properties (e.g., enthalpy and entropy of formation) and the molar volumes of

these phases were adapted from the THERMODDEM database [152] (Table 11). All simulations are carried out at p = 1 bar and T = 25°C in CO_2-free air. It is important to note that the simulations presented do not account for the influences of temperature change on phase relations, (e.g., due the exothermic nature of CAC hydration). The simulations presented apply to two different scenarios: (i) "mature" time scales where C_3AH_6 and AH_3 are the stable hydrates that persists, and, (ii) "early" times where the metastable hydrates such as CAH_{10}, C_2AH_8 and AH_3 persist, while the C_3AH_6 phase is suppressed from forming. For example, the mature age scenario is simulated by restricting the formation of the metastable hydrates, and vice-versa. For the sake of clarity, since the present work seeks to understand the influences of carbonate salts on preventing conversion (i.e., preventing the C_3AH_6 phase from forming at later times), only results corresponding to mature systems are presented.

Table 11: Thermodynamic data for relevant compounds at T = 25°C and p = 1 bar which are used in calculations of phase equilibria		
Phase	**$\Delta_f G^0$ *[kJ/mol]***	**V *[cm^3/mol]***
C_3AH_6	-5010.1	150
C_4AH_{13} (Hydroxy-AFm)	-7326.6	274
C_4AcH_{11} Monocarboaluminate	-7337.5	261
$C_4Ac_{0.5}H_{12}$ Hemicarboaluminate	-7336	285
C_2ASH_8 (strätlingite)	-5705.1	216
M_4AH_{10} (OH-hydrotalcite)	-6394.56	220
M_4AcH_9 (CO_3-hydrotalcie)	-6580.15	220
Water (H_2O)	-237.2	18
SiO_2 (amorphous)	-848.9	29
$Fe(OH)_3$ (microcrystalline)	-711.6	34
$Al(OH)_3$ (amorphous)	-1143.21	32
$Al(OH)_3$ (gibbsite)	-1151	32
Portlandite, $Ca(OH)_2$, CH	-897	33
Calcite, $CaCO_3$,CC	-1129.2	37
Gypsum, $CaSO_4 \cdot 2H_2O$	-1797.8	75
Gaylussite, $Na_2Ca(CO_3)_2 \cdot 5H_2O$ [152]	-3372	148
Thermonatrite, $Na_2CO_3 \cdot H_2O$ [152]	-1286.2	54.8
Natron $Na_2CO_3 \cdot 10H_2O$ [152]	-3427.9	196

It is important to mention that table 11 is an expanded version of table 9 (chapter 4) designed exclusively to integrate the most important phases typically seen in CAC systems. In the case of table 9 (chapter 4), compounds typically found in OPC are used.

5.4 Experimental Results and Discussion

5.4.1 Influence of Limestone (Slightly Soluble Carbonate) Additions

Figure 34(a) shows compressive strength evolutions of mixtures prepared with various levels of CAC replaced by limestone. At any given age, the compressive strength reduces as the amount

of limestone replacing CAC is increased. To account for dilution (i.e., reduction of the CAC content), the compressive strength at 90 days was plot as a function of the CAC fraction in the pastes (Figure 34b). Despite the reduction in strength with a decrease in the CAC content, the strength values remain somewhat above the "dilution line". This implies that the inclusion of limestone results in synergistic effects – which however, are not sufficient to prevent reductions in strength caused due to dilution. As noted in Figure 34(a) all mixtures show a steady increase in strength with age – at ambient curing temperatures (25°C); a low temperature which is known to delay the onset of the conversion process [22,153]. Furthermore, Scrivener et al. [20] noted that compressive strength development in large CAC samples (i.e., more than a few centimeters thick) is different from thinner samples, due to significant heat generation which results in accelerated conversion reactions in the former. After conversion has completed it is postulated that further strength gain may be associated with the formation of increasing quantities of C_3AH_6, Mc, or due to the hydration of residual unhydrated CAC [20] as water released from the metastable hydrates becomes available for reaction.

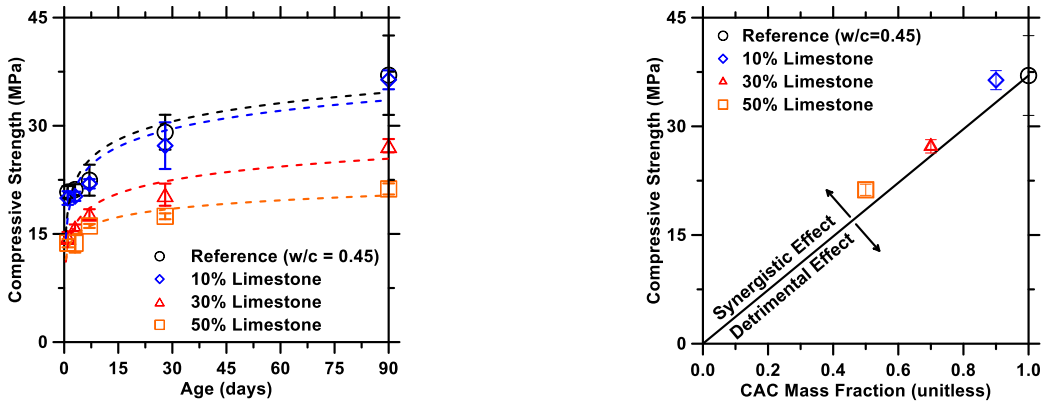

Figure 34: The compressive strength of CAC pastes: (a) As a function of age for various levels of CAC replacement by limestone and (b) After 90 days of hydration as a function of the CAC mass fraction in the binder. For all the mixtures illustrated in the figure, w/s = 0.45.

Figure 35 shows the development of phase assemblages, assessed by qualitative XRD, in blends where 10% (by mass) of the CAC is replaced by limestone. It was observed that an increase in the water content (w/s) results in increased monocarboaluminate (Mc) formation (i.e., based on simple peak height comparisons), and the reduced formation of C_3AH_6 – an outcome which may be associated with inhomogeneous water distributions in the microstructure. The enhanced formation of Mc occurs in conjunction with the consumption of $CaCO_3$ (as also verified from TGA quantifications; Figure 36), since the latter is a reactant in the formation of Mc. The consumption of $CaCO_3$ is accelerated by increasing water content as more limestone solubilizes. For example, after 90 days of hydration in a blend which initially contained 10 mass % limestone, there is less than 2 mass % unreacted limestone present in a system prepared at w/s = 0.70, while around 5 mass % limestone persists in a system prepared at w/s = 0.40. The reduced quantity of C_3AH_6 which was noted with increasing w/s is likely on the account of a larger water content which favors the formation of CAH_{10}, and C_2AH_8 – whose formation is favored at the expense of C_3AH_6 at early ages. In fact, the formation of the C_2AH_8 phase serves as a transitory step in the formation of C_3AH_6 [57,58].

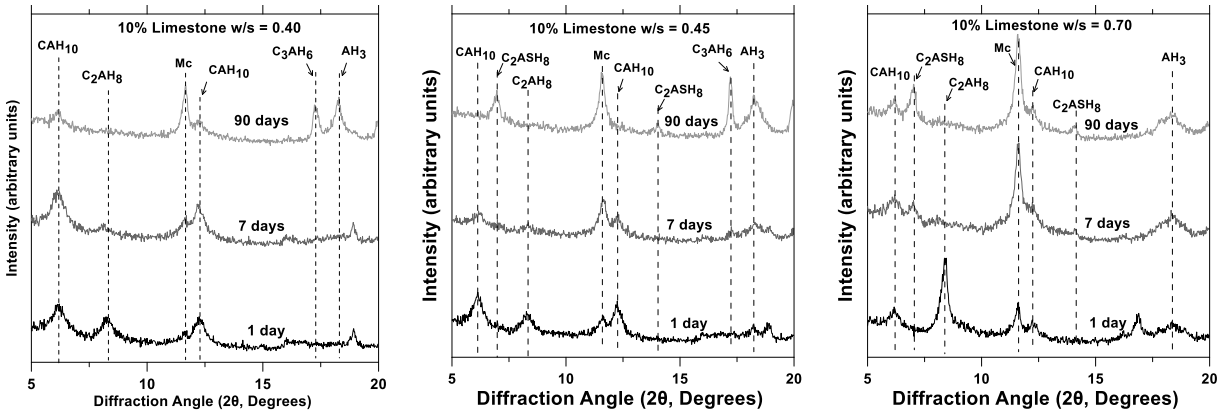

(a) (b) (c)

Figure 35: Representative XRD patterns for the hydrated blends wherein 10 mass % of CAC has been replaced by limestone for blends prepared at: (a) w/s = 0.40, (b) w/s = 0.45 and (c) w/s = 0.70. In all plots, Mc denotes the monocarboaluminate phase ($Ca_4Al_2(CO_3)(OH)_{12}\cdot 5H_2O$).

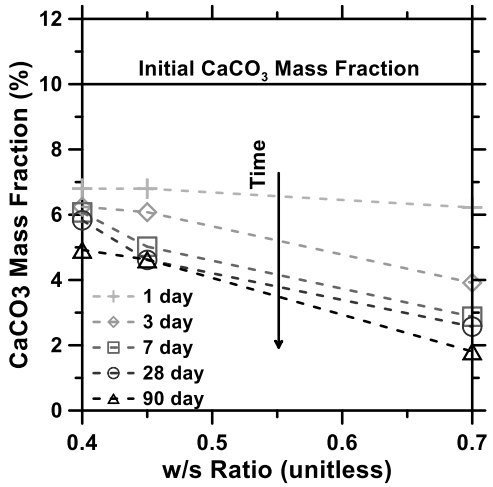

Figure 36: The residual $CaCO_3$ content quantified using thermal analysis (TGA/DTG) in CAC-limestone blends wherein 10 mass % of the CAC was replaced by limestone at different w/s.

The XRD patterns shown in Figure 35 revealed Mc as the only carboaluminate phase (i.e., no Hc is detected) formed independent of w/s or age. This is likely on account of maintenance of a suitable $[CO_3^{2-}]/[OH^-]$ molar ratio in solution which favors the formation of Mc, at the expense of Hc. This is a significant observation in comparison with OPC systems where Hc initially forms and over time transforms to Mc as calcite dissolution progresses [57]. The formation of strätlingite (C_2ASH_8) is favored with increasing water availability. The formation of strätlingite

suggests the hydration of gehlenite (C_2AS), a low reactivity phase [56]. These results, therefore, indicate that the reactivities of both limestone and of C_2AS, and hence the formation of Mc and C_2ASH_8 are enhanced in CAC blends with a higher water content and water activity [58].

5.4.2 The influence of Sodium (Highly Soluble) Carbonate Additions

Figures 37-38 show representative XRD patterns and DTG curves of water-rich (w/s = 0.70) CAC blends prepared with sodium carbonate – where 10 mass %, and 30 mass % of the CAC have been replaced by Na_2CO_3. Several differences with respect to limestone systems were identified. First, it was noted that, unlike systems containing limestone, an increase in the amount of the carbonate source (Na_2CO_3), does not increase the amount of the carboaluminate phase formed. Instead, Na_2CO_3 appears to combine with Ca^{2+} ions present in the solution to form gaylussite ($Na_2Ca(CO_3)_2{\cdot}5H_2O$), and minor amounts of thermonatrite ($Na_2CO_3{\cdot}H_2O$) – whose presence was verified by DTG analyses (Figure 38) which shows characteristic dehydration and decarbonation peaks for the former at 133˚C and 720-750˚C respectively (Eq. 27 [154]) and for the latter around 100°C [155,156]. Since both gaylussite and thermonatrite are "water-rich phases" containing 5 and 1 formula units of water respectively, the formation of these phases is suppressed in systems that are water deficient (e.g., w/s = 0.40; see Figures 37a and 38a).

$$Na_2Ca(CO_3)_2 \cdot 5H_2O \xrightarrow{133℃} Na_2Ca(CO_3)_2 + 5H_2O \quad \text{(equation 27a)}$$

$$Na_2Ca(CO_3)_2 \xrightarrow{720\ to\ 750℃} Na_2CO_3 + CaO + CO_2 \uparrow \quad \text{(equation 27b)}$$

Significantly, the conversion of metastable calcium aluminate hydrates (i.e., CAH_{10} and C_2AH_8) to C_3AH_6 occurs despite provision of a carbonate source, and water (Figures 37c and 38c). The amount of Mc present decreases between 7 and 90 days, while quantities of both C_3AH_6 and AH_3 increase during the same period. This destabilization of Mc with respect to C_3AH_6 is not

expected – as Mc is anticipated to remain stable (at ambient temperature) with respect to C_3AH_6 and the calcium salt, whose anion is contained in the AFm interlayer position. In contrast, in CAC-limestone blends, at high w/s (e.g., for w/s = 0.70), the amount of C_3AH_6 present is negligible as compared to the Mc content (Figure 35c).

The destabilization of Mc to C_3AH_6 over the course of time in the Na_2CO_3-rich systems, is speculated to be on account of differences in the binder chemistry. These differences in Na_2CO_3 mixtures as compared to $CaCO_3$ systems are likely due to changes in the $CO_{2\text{-}eq}$/CaO ratio (Figure 33c) with increasing CAC replacement. This implies that systems with a higher $CO_{2\text{-}eq}$/CaO ratio form phases with a higher CO_3^{2-} and lower Ca^{2+} content (i.e., as compared to Mc and Hc), which in a Na^+ concentrated environment results in the formation of gaylussite or thermonatrite. The formation of gaylussite and thermonatrite consumes a large quantity of water (e.g., 5 and 1 molar units of water respectively are taken up per formula unit of gaylussite and thermonatrite) which may lead to the formation of C_3AH_6 as the dominant stable phase due to its low water content, and simultaneously prevent carboaluminate phase formation. A similar hindrance in NO_3-AFm phase formation due to limited water availability was also noted when $Ca(NO_3)_2$ was used as an agent to suppress conversion in CACs [58] (i.e., to form the favored NO_3-AFm phase) suggesting that bulk chemical composition is an insufficient indicator of the ability to prevent conversion – but rather, the amount of water present is also a relevant variable.

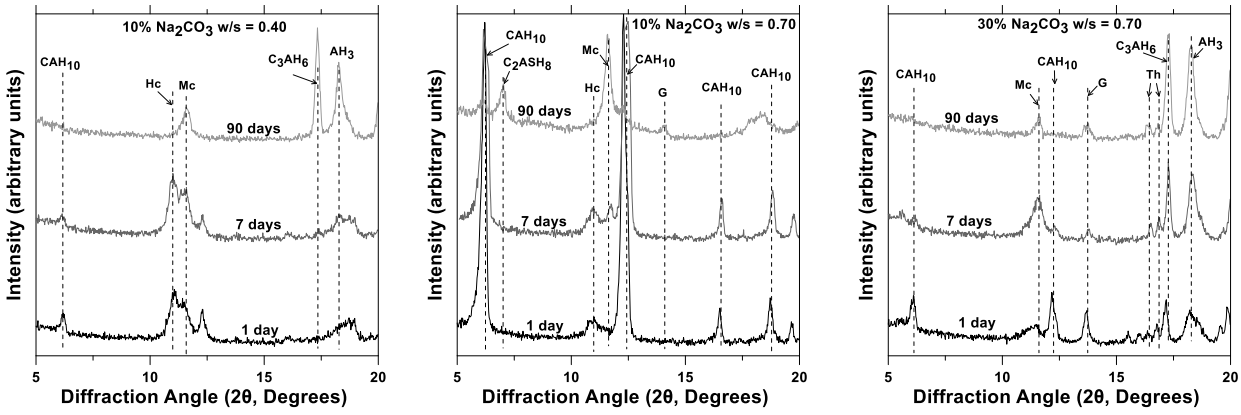

Figure 37: Representative XRD patterns of the hydrated CAC-Na_2CO_3 blends for: (a) w/s = 0.40, 10% Na_2CO_3, (b) w/s = 0.70, 10% Na_2CO_3 and (c) w/s = 0.70, 30% Na_2CO_3. In all plots, G: gaylussite ($Na_2Ca(CO_3)_2{\cdot}5H_2O$), Th: thermonatrite ($Na_2CO_3{\cdot}H_2O$), Mc: monocarboaluminate ($Ca_4Al_2(CO_3)(OH)_{12}{\cdot}5H_2O$), and Hc: hemicarboaluminate ($Ca_4Al_2(CO_3)_{0.5}(OH)_{13}{\cdot}5.5H_2O$).

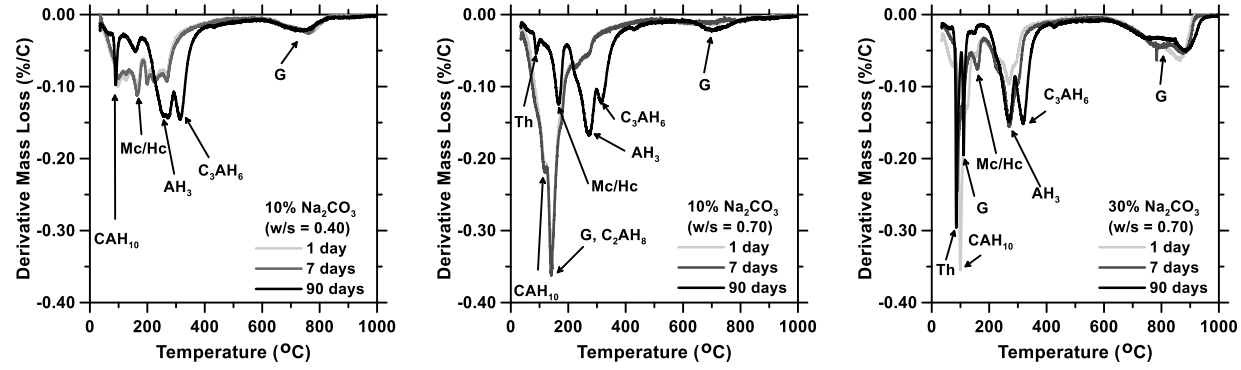

Figure 38: Representative DTG traces for the hydrated CAC-Na_2CO_3 blends for: (a) w/s = 0.40, 10% Na_2CO_3, (b) w/s = 0.70, 10% Na_2CO_3 and (c) w/s = 0.70, 30% Na_2CO_3. In all plots, G: gaylussite ($Na_2Ca(CO_3)_2{\cdot}5H_2O$), Th: thermonatrite ($Na_2CO_3{\cdot}H_2O$), Mc: monocarboaluminate ($Ca_4Al_2(CO_3)(OH)_{12}{\cdot}5H_2O$), and Hc: hemicarboaluminate ($Ca_4Al_2(CO_3)_{0.5}(OH)_{13}{\cdot}5.5H_2O$).

Unlike $CaCO_3$ containing systems, blends containing lower Na_2CO_3 contents (10 mass %) show the formation of Hc at early ages (see Figures 37a-b). The Hc formed, converts to Mc at later ages. While such behavior is seen in OPC systems containing limestone where the formation of Hc precedes Mc [79] – this behavior is not observed in CAC blends with limestone (see Figure 35) where Mc forms rapidly. Taken together, these results note the relevance of: (i) water

availability, (ii) the solubility of the carbonate source, and, (iii) the calcium content of the carbonate source as major variables which influence stable phase relations in CAC blends that are hydrated at 25°C and under sealed conditions.

5.5 Thermodynamic Calculations

5.5.1 The Role of Water Content on Phase Equilibria

A series of thermodynamic calculations were carried out to understand, parametrically, how the water content of a given mixture influences stable phase equilibria when CAC is replaced by a carbonate source. Figure 39 shows equilibrium phase assemblages assessed in blends wherein 10 mass % of the CAC has been replaced by limestone. In general, systems prepared at lower w/s (e.g., w/s = 0.40) show the increasing formation of Mc and AH_3, until water is exhausted (Figure 39a). The formation of C_3AH_6 is prevented so long as free water is available. However, once free water is consumed (around 70 % CAC reaction), Mc decomposes or stops forming, and other phases such as AH_3, C_3AH_6 and $CaCO_3$ are expected to precipitate. Such sacrificial behavior of Mc, in favor of C_3AH_6 and $CaCO_3$, in water deficient systems is not observed experimentally as Mc continues to form over time (i.e., as the CAC reaction progresses) despite the low water content (see Figure 35a) – at least until 90 days. This points to the stability of Mc in CAC-limestone systems, wherein once formed, this phase remains stable in spite of low water availability. It is however possible that the decomposition of Mc into $CaCO_3$ and C_3AH_6 occurs at times later than 90 days.

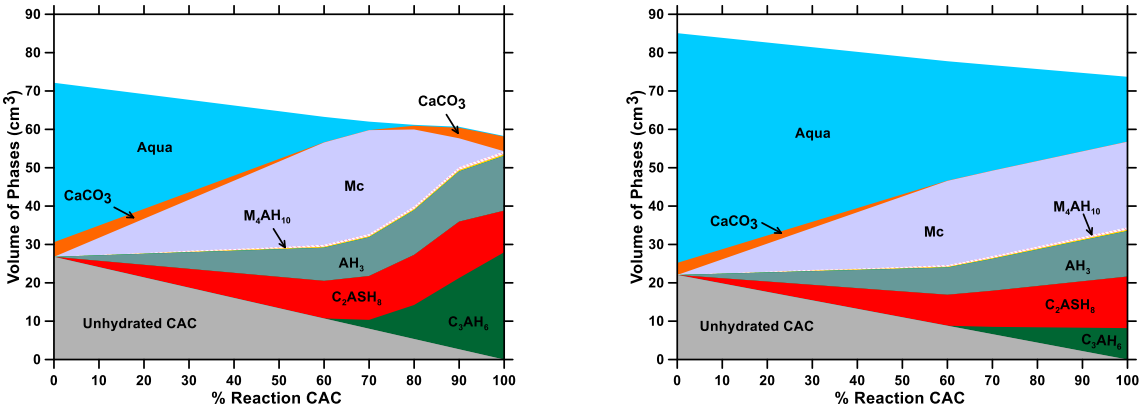

Figure 39: The volumetric phase assemblage calculated to exist when 10 mass % CAC has been replaced by limestone ($CaCO_3$) for: (a) w/s = 0.40 and (b) w/s = 0.70. In these plots: Mc: monocarboaluminate ($Ca_4Al_2(CO_3)(OH)_{12}\cdot 5H_2O$) and M_4AH_{10}: OH-hydrotalcite.

In cases where water is abundant, Mc persists, as long as limestone is present (see Figure 39b). But, when limestone is consumed, expectedly, C_3AH_6 forms as a stable phase. In agreement with experimental data (Figure 35), the calculations predict the formation of C_2ASH_8 (strätlingite) due to the C_2AS hydration, in water-deficient and water-rich systems (Figures 39). The calculations also suggest that under water-rich and kinetically unconstrained conditions, as long as limestone is present, the conversion process can be mitigated. This is however unrealistic, because under practical conditions the ability to suppress conversion when limestone is present is negligible [22]. This discrepancy arises because the calculations due to their equilibrium nature do not account for the slow dissolution of $CaCO_3$ – which prevents it from serving as an effective conversion suppression agent. As a result, at any extent of CAC reaction, the calculations overestimate the amount of $CaCO_3$ consumed, the quantity of Mc formed, and thus the success (or lack thereof) of mitigating the conversion phenomena.

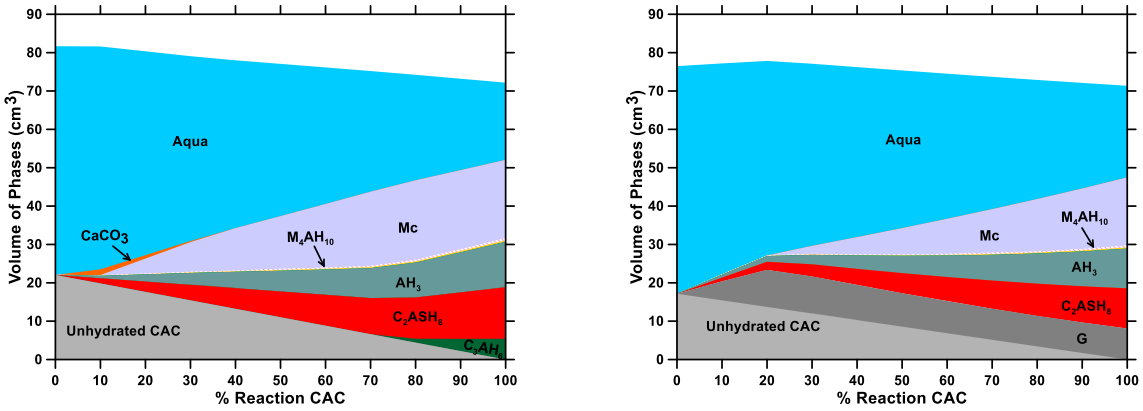

(a) (b)

Figure 40: The volumetric phase assemblage calculated to exist for w/s = 0.70 when CAC has been replaced by Na_2CO_3 at the level of (by mass): (a) 10 mass % and (b) 30 mass %. In these plots: G: gaylussite ($Na_2Ca(CO_3)_2 \cdot 5H_2O$), Mc: monocarboaluminate ($Ca_4Al_2(CO_3)(OH)_{12} \cdot 5H_2O$) and M_4AH_{10}: OH-hydrotalcite.

Figure 40 shows equilibrium phase assemblages in water-rich (w/s = 0.70) systems where 10 mass % and 30 mass % CAC have been replaced by Na_2CO_3. In these cases, the formation of C_3AH_6 is either delayed or negated with rising Na_2CO_3 dosages and with an increasing extent of CAC reaction. At modest Na_2CO_3 dosages (10 mass %), AH_3 and Mc are predicted to form (Figure 40a), the latter by the uptake of CO_3^{2-} species solubilized in the pore fluid, while Na^+ remains mobile in the pore solution (N.B.: alkali uptake is not considered herein). When Na_2CO_3 dosages are increased, gaylussite ($Na_2Ca(CO_3)_2 \cdot 5H_2O$) forms with a corresponding decrease in the amount of AH_3 and Mc present – in agreement with XRD and DTG data as shown in Figures 37c and 38c respectively. The formation of gaylussite is ensured by the need to allocate sodium and carbonate species, which in turn, penalizes the formation of Mc (see Figure 40b).

The formation of water rich phases (gaylussite and thermonatrite), and their resultant water uptake does not trigger the formation of C_3AH_6 (a dense, low water content phase) as seen in the XRD data (a Figure 37c) and Mc continues to form unimpeded (Figure 40). While the reasons for this discrepancy are not fully clear it is thought to be on account of the calculations being

unable to account for the water activity dependent stability of Mc, which destabilizes below a critical water activity [157,158], or due to C_3AH_6 formation in inhomogeneous microstructural zones. Water activity is discussed, as the solubilization of Na_2CO_3 into the mixing water would result in significant reductions in the water activity. It is seen that thermonatrite (Th, $Na_2CO_3 \cdot H_2O$) which although present in the XRD data (Figure 37c), is absent in the predicted phase assemblages at equilibrium (Figure 40b). This is thought to be because thermonatrite forms at the time of early CAC hydration (i.e., when Na_2CO_3 is added to the mixing water) and remains unaffected thereafter (e.g., see near constant thermonatrite intensities in the XRD patterns across all ages).

5.5.2 The role of the Calcium Content of the Carbonate Source

To estimate the effects of the "calcium content" of the carbonate source a new series of simulations were carried out. Here, the level of CAC replacement (by a carbonate source) varies between 0-to-50 mass %. At each replacement increment, a process simulation was carried out, in which, the amount of carbonate source was progressively reduced while increasing the CaO content of the system, (i.e., to simulate the influence of CaO that could accompany the carbonate salt). In these calculations the quantity of the carbonate source and additional CaO provided (i.e., over and above CaO contributed by the CAC) was fixed according to the level of CAC replacement. For example, in the case of a 30 mass % CAC replacement, the CaO-to-carbonate source ratio (see x-axis in Figure 41) ranges from 0.93-to-18.30 for both carbonate sources (Na_2CO_3 and $CaCO_3$).

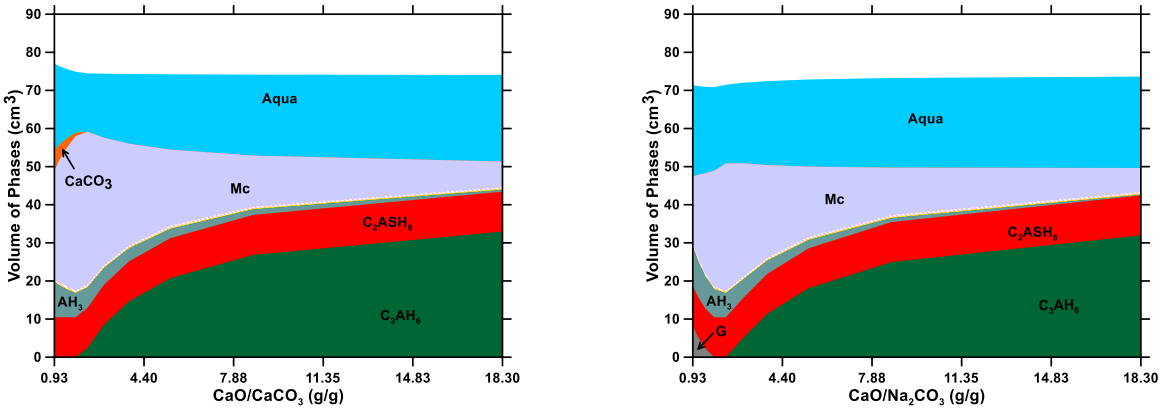

Figure 41: The volumetric phase assemblage calculated to exist for w/s = 0.70 when 30 mass % of the CAC has been replaced by a combination of: (a) CaO and $CaCO_3$ and (b) CaO and Na_2CO_3. In these plots: G: gaylussite ($Na_2Ca(CO_3)_2 \cdot 5H_2O$), Mc: monocarboaluminate ($Ca_4Al_2(CO_3)(OH)_{12} \cdot 5H_2O$) and M_4AH_{10}: OH-hydrotalcite.

Figure 41 shows the volumetric phase assemblage as a function of an increase in the CaO-to-carbonate source ratio. It is seen that the phase assemblage alters significantly as CaO/XCO_3 ratio (where X = Ca, Na_2) increases. Specifically, the amount of Mc produced, by both carbonate sources, initially increases and then reaches a maximum at a $CaO/XCO_3 \approx 2.0$, and decreases thereafter. $CaCO_3$ is slightly more efficient than Na_2CO_3 in forming Mc at a similar CaO/XCO_3 value on account of: (a) its greater provision of Ca^{2+} ions when X = Ca than X = Na, and (b) limestone's low solubility which implies that water activity of the pore fluid is higher when X = Ca than X = Na, a condition that potentially favors the formation of Mc. This points to the relevance of the carbonate source's calcium content, and its solubility as factors controlling carboaluminate phase formation in CAC systems.

5.6 Summary and Concussions Chapter 5

The influences of slightly ($CaCO_3$), and highly soluble (Na_2CO_3) carbonate salts on hydrated phase relations in calcium aluminate cements (CACs) have been critically examined. It has been shown that water availability, and the solubility and calcium content of the carbonate source play

important and interrelated roles in the formation of carboaluminate phases. In the case of slightly soluble carbonates ($CaCO_3$), a higher water availability (and water activity) is linked to an increase in carbonate source consumption and carboaluminate (Mc) phase formation. These conclusions are supported by experimental observations of thermogravimetric and X-ray diffraction datasets. Comparisons between thermodynamic calculations and experimental results reveal that $CaCO_3$ consumption is limited due to the low aqueous solubility and dissolution rate of $CaCO_3$ – which are limiting factors in carboaluminate phase formation.

To overcome the limitations of $CaCO_3$ use, a soluble carbonate salt (Na_2CO_3) was studied as a potentially more reactive carbonate source. Despite its high solubility, thermogravimetric and X-ray diffraction data show that Na_2CO_3 also fails to boost carboaluminate phase formation. In this case, the formation of other carbonate bearing phases (i.e., gaylussite and thermonatrite) that compete for CO_3^{2-} ions suppresses carboaluminate phase formation. The formation of these other carbonate phases (i.e., which lack aluminum, and feature a lower Ca^{2+} content as compared to the carboaluminate hydrates), and the persistence of AH_3 in Na_2CO_3 systems, indicates that the calcium content of the carbonate source is a key variable which influences carboaluminate phase formation. It is noted that reductions in water activity resulting from the solubilization of ions negatively affects carboaluminate phase formation. It is thus concluded that, independent of the carbonate salt used, carboaluminate phase formation is not a viable solution to mitigate conversion phenomena in hydrated CACs.

Chapter 6: Kinetics of Ion Exchange in AFm phases

6.1 Scope of Chapter 6

This chapter describes the kinetics of ion exchange in AFm phases. Chapter 5 showed that one limiting factor for formation of calcium carboaluminate phases in cement is the low solubility of limestone. However, the kinetics of ion exchange in AFm phases can also constitute a limiting step in calcium carboaluminate formation. In order to bring about an understanding of this ion exchange process, two anions (Cl^- and NO_3^-) are used as exchanging species in an AFm structure. Furthermore, studies on ion exchange kinetics can also be applied to the broader scope of layered double hydroxides which AFm phases are a part of.

Layered double hydroxides (LDHs) are complex inorganic oxides that consist of positively charged layers of $M(OH)_6$ where M represents metallic cations with valencies that range from 1 to 3 (i.e., Li^{1+}, Cu^{2+}, Zn^{2+}, Mg^{2+}, Ca^{2+}, Al^{3+}, Cr^{3+} and Fe^{3+}) that intercalate within interlayer sites neutralizing (valence compensating) anions that may be inorganic (i.e., Cl^-, CO_3^{2-},NO_3^- and SO_4^{2-}) [159] or organic (i.e. $C_2O_4^{2-}$, $C_6H_5O_7^{3-}$ or $C_7H_5O^{2-}$) [160,161] and water. The layered structure resembles that of naturally occurring minerals known as hydrotalcites and hence LDH's are also termed as *hydrotalcite-like* compounds [162,163,164]. LDH's have been the subject of intense study for their ability to exchange ions contained in their interlayer positions [162,163,165,166]; an ability can find applications in nanocomposites [167,168,169], flame retardants [170,171], catalysts [172,173], CO_2 sequestration [174], and medical applications where LDH's can be used for controlled drug release [175,176,177,178].

The majority of studies on LDH's have focused on their synthesis and characterization [167,179,180]. As a result, special focus has been paid to examine "thermodynamic factors" as relevant to the stability of LDH's structures and their intercalated organic and inorganic solvated

anions, metallic cations present at the $M(OH)_6$ layer, etc. [21,181,182,183,184]. While LDH's have often been synthesized by ion-exchange, where more favorable anions may displace less favorable anions [161,185,186,187,188] – the kinetics of the ion-exchange process have been lesser studied [189]. This is important because while thermodynamic equilibrium (e.g., between the solid and solution) may often be assumed during LDH formation or ion-exchange, the equilibrium may be conditional or metastable – due to kinetic restraint, hindered diffusion, or due to asymptotic ion-exchange (reaction) rates which manifest with reducing thermodynamic driving force.

To better understand kinetic controls on ion-exchange, a model hydrated calcium-alumino LDH (i.e., AFm: alumino-ferrite monosubstituent sub-group [21]) is studied in terms of its ability to accommodate solvated Cl^- anions at the expense of NO_3^- anions that are natively hosted in the interlayer. In brief, AFm's have the formula $[Ca_2(Al,Fe)(OH)_6]\cdot X\cdot nH_2O$ where X is the exchangeable singly charged or half of a doubly charged, anion, and n denotes the number of water molecules [21]. Similar to a brucite-like layered structure, the principal layers in AFm phases comprise Ca^{2+} ions with regular substitution of Ca^{2+} by Al^{3+} and/or Fe^{3+} species [21]. This positively charged "main layer" shows a composition of $[Ca_2(Al,Fe)(OH)_6]^+\cdot 2H_2O$ (Figure 42a). A variety of anions (and water molecules) can be hosted in the AFm interlayer with the general composition $[X\cdot xH_2O]-$ where X denotes, e.g., OH^-, or half of a doubly charged anion, e.g. $½SO_4^{2-}$ [21,190]. Common ions present in AFm interlayers include: OH^-, SO_4^{2-}, CO_3^{2-}, NO_3^-, NO_2^- and Cl^- [21,127,190]. Other anions like CrO_4^{2-} and SeO_4^{2-} can also be hosted [191,192,193]; and organic anions, e.g., carboxylic acid groups can also be incorporated [160,161] – although the interlayer spacing needs to expand to *fit* large moieties.

Based on recent studies, it has been revealed that the site occupation preference, for common ions, in the AFm interlayer scales as: $Cl^- > NO_3^- > NO_2^- > CO_3^{2-} > SO_4^{2-} > OH^-$ [127]. However, the rate of exchange of a more preferred species (e.g., Cl^-) for a less preferred species (e.g., NO_3^-) and its rate-controlling step [194,195] remain unknown. Therefore, to better understand such aspects, and develop more effective LDH synthesis routes monovalent anion exchange by the NO_3-AFm phase is studied across a range of Cl^- concentrations (0.01, 0.1 and 1 mol/L), at different temperatures (i.e., 5 °C, 25 °C, and 45 °C) and under different solution conditions, i.e., static (when transport of ions is diffusive), and convectively mixed (when the solution is robustly stirred). The outcomes reveal the rate constants of the ion-exchange process, and its rate-limiting step thereby offering robust abilities to model, predict and control such reactions in aqueous environments.

6.2 Materials Synthesis

Ca3Al2O6 Synthesis: Phase pure $Ca_3Al_2O_6$ was prepared by combining analytical reagent (AR) grade $CaCO_3$ and Al_2O_3 in a 3:1 molar ratio. The powders were initially dry-mixed, homogenized and pressed into pellets using a steel die at a compaction pressure of 10 MPa. The pellets were placed in zirconia grain-hardened platinum crucibles, and sintered at 1450 ˚C in a muffle furnace, in air, for a 24 hour period. At the end of the sintering routine, the pellets were air quenched. The pelletized, sintered material was then finely ground, pelletized once again, and the sintering routine repeated two more times. Grinding was carried out using a stainless steel ring grinder (Figure 42b). After preparation, the purity of the $Ca_3Al_2O_6$ was examined using X-ray diffraction (XRD) by comparing the measured XRD pattern to that of phase pure $Ca_3Al_2O_6$ (ICSD: 1841), $CaCO_3$ (ICSD: 79673) and Al_2O_3 (ICSD: 10425) to confirm phase purity. The

$Ca_3Al_2O_6$ thus prepared was stored under vacuum in a desiccator at room temperature until its time of use.

NO_3-AFm synthesis: Pure NO_3-AFm ($Ca_4Al_2(NO_3)_2(OH)_{12}\cdot xH_2O$, x indicates the number of water molecules) was prepared by a solution precipitation route by contacting $Ca_3Al_2O_6$ and reagent grade $Ca(NO_3)_2\cdot 4H_2O$ in a 1:1 (stoichiometric) molar ratio in excess MilliQ water. The liquid-to-solid ratio (mass basis) was around 50. The reaction was carried out under continuous stirring at 25 °C in an "atmos-bag", i.e., in a CO_2-free environment. This mixture was stirred continuously for a period of three weeks in sealed HDPE bottles to minimize carbonation, if any. At the end of the three week period, the precipitates were filtered using filter paper (2.5 µm opening) placed in a funnel that led into an Erlenmeyer flask. The precipitates were thoroughly rinsed in MilliQ water, three times, to remove any residual traces of precursors, solids, or solvated ions, which may be attached to their surfaces. The NO_3-AFm thus prepared was stored in an evacuated desiccator at 25 ˚C over a saturated $CaCl_2$ solution to equilibrate the samples to a relative humidity (RH) of 38 ± 2%. After equilibration for three weeks, the NO_3-AFm precipitates were ground using an agate mortar and pestle (Figure 42b), and once again placed over the saturated $CaCl_2$ solution for RH conditioning.

Cl-AFm synthesis: Pure Cl-AFm ($Ca_4Al_2(Cl)_{1.95}(OH)_{12.05}$ (i.e., Friedel's salt [184]) was prepared by ion-exchange of NO_3-AFm in a $CaCl_2$ solution. The exchange reaction was carried out with convective mixing in a 2 mol/L $CaCl_2$ solution for a period of 2 weeks until the Cl^- concentration in solution showed no further change. After this, the precipitates were filtered and rinsed using MilliQ water, three times, to remove any residual traces of precursors, solids or solvated ions, which may be attached to their surfaces. The Cl-AFm was stored in an evacuated Pyrex desiccator at 25 ˚C over a saturated $CaCl_2$ solution to equilibrate the samples to a relative

humidity (RH) ≈38%. After their equilibration for three weeks, the Cl-AFm precipitates underwent the same grinding procedure as the pure NO_3-AFm solids.

6.3 Experimental Procedures

Particle size analysis: The particle size distribution (PSDs, Figure 42b) of the synthesized $Ca_3Al_2O_6$ and NO_3-AFm particulates was measured using a Beckman Coulter Static Light Scattering Analyzer (LS13-320) using isopropanol (IPA) and ultrasonication for dispersing the powders to primary particles. The uncertainty in the light scattering analysis was determined to be around 6% based on analysis of six replicates. The specific surface area of the solid particulates was estimated by assuming the density of the $Ca_3Al_2O_6$ (660 m^2/kg) and NO_3-AFm (1450 m^2/kg) to be 3.028 g/cm^3, and 2.067 g/cm^3, respectively [58].

Solution phase analysis: A ThermoScientific Orion VersaStar multi-parameter benchtop meter provided with pH and ion-selective electrodes (ISEs) was used to assess the concentration of ions, and the solution pH. Temperature corrections were carried out dynamically. For anions, i.e., NO_3^- and Cl^-, the following ion-selective electrodes where used; ThermoScientific 9707BNWP (NO_3^- ISE) and 9617BNWP (Cl^- ISE). pH was measured using a ThermoScientific Ross Ultra electrode. The pH electrode was calibrated via a 4-point calibration every 48 hours using reference (buffer) solutions over the range $3 \leq pH \leq 13$ at 25 °C ± 3 °C. The ISEs were calibrated every 48 hours at 25 °C ± 3 °C using calibration solutions prepared with Milli-Q water and reagent grade $CaCl_2$ or $Ca(NO_3)_2.4H_2O$ respectively over the concentration range 0.0001 mol/L $\leq C \leq$ 1 mol/L where C is the solution concentration (mol/L). The calibration solutions were dosed with the recommended amount of ionic strength adjuster (ISA; 2 mL of ISA per 100 mL of solution).

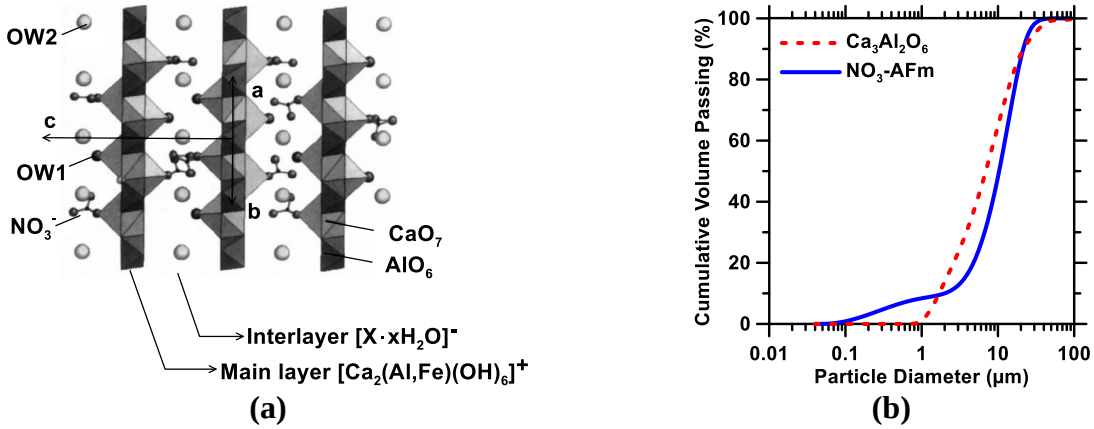

Figure 42: (a) The layered structure of $3CaO \cdot Al_2O_3 \cdot Ca(NO_3)_2 \cdot 10H_2O$ (i.e., NO_3-AFm) refined by Renaudin et al [196] showing the locations of $[AlO_6]$, $[CaO_7]$ polyhedral, charge compensating anions (NO_3^-), bound (OW1) and free water (OW2). The projection of the crystal structure is shown along the [110] plane, and, **(b)** The particle size distributions of the as-synthesized $Ca_3Al_2O_6$ and the NO_3-AFm powders.

X-Ray Diffraction (XRD): Qualitative X-ray diffraction analysis was carried out on the powdered $Ca_3Al_2O_6$ particulates, and AFm samples before/after ion-exchange using a Bruker D8-Advance diffractometer in a θ-θ configuration using Cu-Kα (λ = 1.54 Å) radiation. The powder samples were scanned between 5° and 70° (2θ) in continuous mode with an integrated step scan of 0.017° (2θ) using a VANTEC-1 detector. The time required for acquisition of X-ray diffraction patterns was around 12 minutes. A fixed divergence slit of 0.50° was used during data acquisition. Care was taken to minimize preferred orientation errors by texturing the sample surface, and using a rotating sample stage to acquire statistically averaged X-ray data.

Ion-exchange process: First, exchange of the anion (NO_3^-) contained in the AFm interlayer was carried out in a thermodynamically "preferred" forward direction, i.e., NO_3^- ions were exchanged for Cl^- species (Equation 28; left-to-right). Ion exchange was carried out by immersing NO_3-AFm in Cl^- solutions (prepared from $CaCl_2 \cdot H_2O$) of concentrations: 0.01 mol/L, 0.1 mol/L and 1 mol/L respectively. Here, 1 g of NO_3-AFm particulates were batched using an analytical balance, and immersed in 100 ml of "exchange solution". Ion-exchange was monitored at temperatures of

5 °C, 25 °C and 45 °C for each exchange solution concentration. Second, the thermodynamically "less preferred" reverse process was carried wherein 1 g of Cl-AFm (Friedel's salt) was immersed in 100 g of a 0.1 mol/L NO_3^- solution (prepared from $Ca(NO_3)_2 \cdot 4H_2O$) at 5 °C and 45 °C respectively (Equation 28; right-to-left). During ion-exchange, the HDPE containers containing the solids and solution were sealed to minimize the potential for evaporation.

Ion exchange was carried out under conditions of lime saturation to stabilize the pH and create a caustic environment (pH ≈ 12.6 at 25 °C) in which the AFm phases are stable. As such, 1 g of solid $Ca(OH)_2$, segregated in a "filter bag" was suspended at the mid-height of the container using a nylon filament. The conditions of evaluation included: (i) non-convective ("static conditions"), where the transport of ions in solution occurs by diffusion, and, (ii) convective ("stirred") mixing, wherein the solution was mixed by a magnetic stir-bar, so that ion-diffusion in bulk solution could not serve as a "rate-controlling step". In the case of reverse direction ion exchange, the systems were studied only under conditions of convective mixing.

$$Ca_4Al_2(NO_3)_2(OH)_{12} \cdot 4H_2O + 1.95\,Cl^- + 0.05OH^- \leftrightarrow Ca_4Al_2(Cl)_{1.95}(OH)_{12.05} + 4H_2O + 2NO_3^- \quad \text{(equation 28)}$$

After allowing ion-exchange to occur for a specific period (i.e., generally ≤ 35 days, or when the measured concentration differed from its preceding value by ≤ 5 %), small quantities (≤ 1.8 mL) of solution were extracted from close to the container wall, near the top-surface using a syringe fitted with a fine needle. The solution was subsequently filtered through a 0.2 μm syringe filter and diluted around 10 times (by mass) using MilliQ water. Any unused, or excess solution was returned to the container. Following dilution, the solution was acidified using HNO_3 when Cl^- species needed to be measured, or HCl, when NO_3^- species were to be measured. Acidification

was carried out such that the solution pH at the end of this step ranged between 3-to-4 (pH units). Finally, around 0.4 mL of ionic strength adjuster (ISA) was added to the acidified solution, after which the ion-selective electrodes (ISE's) were immersed in the solution for recording NO_3^- and Cl^- ion concentrations.

Solution analyses were carried out after 2, 5, 10, 30, 60, 120, 240 minutes and 24, 48, 72 and 144 hours after the NO_3-AFm (or Cl-AFm) was first immersed in the exchange solution. However, certain tests, especially those carried out at low-temperature were permitted to proceed until 336 hours due to the slow ion-exchange kinetics observed at sub-ambient temperatures. It should be noted that while Cl^- concentrations were measured under all conditions, NO_3^- concentrations were measured only for studies carried out at 25 °C under stirred conditions in the forward direction. At the end of the ion-exchange process, or when the experiment ended, the solid AFm particulates were extracted and filtered (2.5 μm opening). The filtered material was then stored in an evacuated desiccator over saturated $CaCl_2$ solution for a period of at least 4 weeks. At the end of 4 weeks, XRD patterns of the precipitates were acquired to assess the effects of ion-exchange processes on compositional conversions between NO_3-AFm and Cl-AFm.

6.4 Simulations

6.4.1 Thermodynamic Calculations

Thermodynamic calculations were carried out using a geochemical code, GEMS-PSI: Gibbs Energy Minimization Software, version 2.3.1 [89]. GEMS uses input chemical compositions in the form of simple oxides for the solid precursors and water, and applies a convex programming approach in conjunction with data of the thermodynamic properties of phases (solids, liquid, air) to compute equilibrium phase balances and ion-speciation in a multicomponent system.

Thermodynamic data of calcium hydroxide, the AFm phases and aqueous species were sourced from the GEMS-PSI database, and amended as needed [58,184]. Equilibrium phase balances were computed at standard pressure (1 bar) and across all temperatures studied (5 °C, 25 °C, and 45 °C). The input compositions consisted of NO_3-AFm (or Cl-AFm), $Ca(OH)_2$, $CaCl_2$ (or $Ca(NO_3)_2 \cdot 4H_2O$) and Milli-Q water to recreate the conditions of ion-exchange in both the forward or the reverse directions. The exchange solution environment was varied by increasing the quantity of $CaCl_2$ and $Ca(NO_3)_2$ that is present to increase the driving force for AFm ion-exchange and compositional alterations. The vapor phase at equilibrium with the solids and the liquid phase was set to be CO_2-free air.

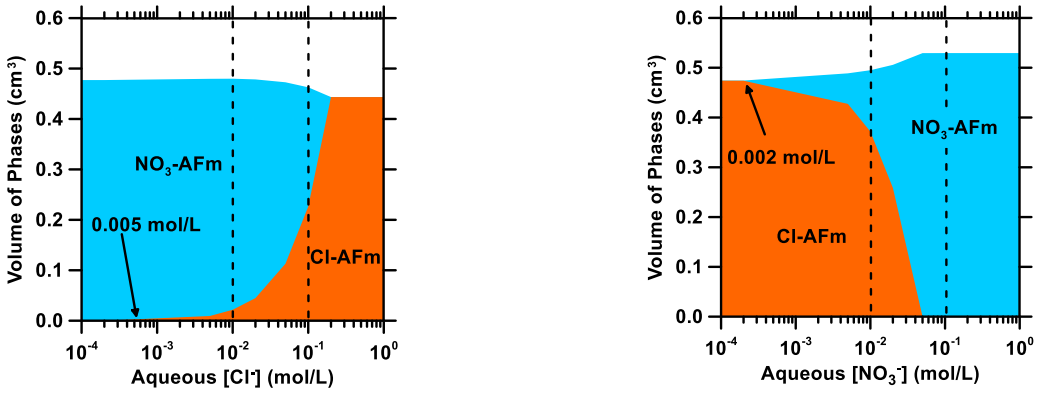

Figure 43: The volumetric distributions of AFm phases at 25 °C obtained via a progressive equilibrium simulation for: **(a)** NO_3-AFm exposed to Cl^- solutions (i.e., in direction of preferred ion-exchange, see Equation 1), and, **(b)** Cl-AFm exposed to NO_3^- solutions (i.e., in direction of non-preferred ion-exchange, see Equation 1). The dashed lines show the concentrations of ions (C_0) initially present in the exchange solution in the experimental studies that follow.

Figures 43 (a and b) show the volumetric distributions of AFm phases undergoing ion-exchange in the forward (i.e., NO_3-AFm converts to Cl-AFm) and reverse directions (i.e., Cl-AFm converts to NO_3-AFm), respectively. For clarity, the hydrate assemblages presented only show distributions of AFm phases (i.e., $Ca(OH)_2$, water, etc. are omitted). Expectedly, the extent of compositional conversion increases with the concentration of exchangeable anions in the

exposure solution. Significantly, it is noted that such conversions only initiate when the concentrations of the exchangeable anion in the exposure solution exceeds a threshold level. Unexpectedly, although Cl-AFm is more stable than its NO_3-AFm variant (i.e., based on solubility data [127]); conversion in the reverse direction Cl-AFm to NO_3-AFm initiates at a smaller abundance solution concentration ($[NO_3^-]$ = 0.002 mol/L) than that required to initiate the forward reaction ($[Cl^-]$ = 0.005 mol/L). Given the similar molar volumes of the AFm phases [127], negligible volume change (≤ 9%) occurs following compositional conversion. Due to the stability of the AFm phases over the temperature range (5 °C-to-45 °C) of interest, temperature exerts little influence on the results (not shown). It should be noted that the simulations make no consideration for the formation of solid-solutions and provide no guidance on the rate at which ion-exchange induced composition conversions may occur.

6.5 Experimental Results and Discussion

Reaction kinetics: Figure 44 shows the temporal Cl^- concentrations for NO_3-AFm undergoing ion-exchange at 5 °C and 45 °C under static and convective mixing conditions. Expectedly, the rate of ion-exchange (Cl^- ion uptake) significantly increases as the temperature is elevated. Convective mixing also accelerates ion exchange in comparison to static solution conditions. Ion-exchange completes rapidly at 45 °C (i.e., when the NO_3-AFm takes up 0.00325 moles of Cl^- ions per gram of solids to saturate the interlayer sites). Taking into account a total exchange solution volume of 0.1 mL, the Cl^- concentration in solution achieves a known C_f threshold when ion-exchange completes; see Figure 44b [58,197]). But, this is not so at 5 °C wherein the Cl^- concentration achieves a limiting asymptotic value. This is because of very retarded ion-exchange kinetics at low temperature, and/or to a smaller effect on account of improved stability of NO_3-AFm at low-temperatures vis-à-vis ambient temperatures.

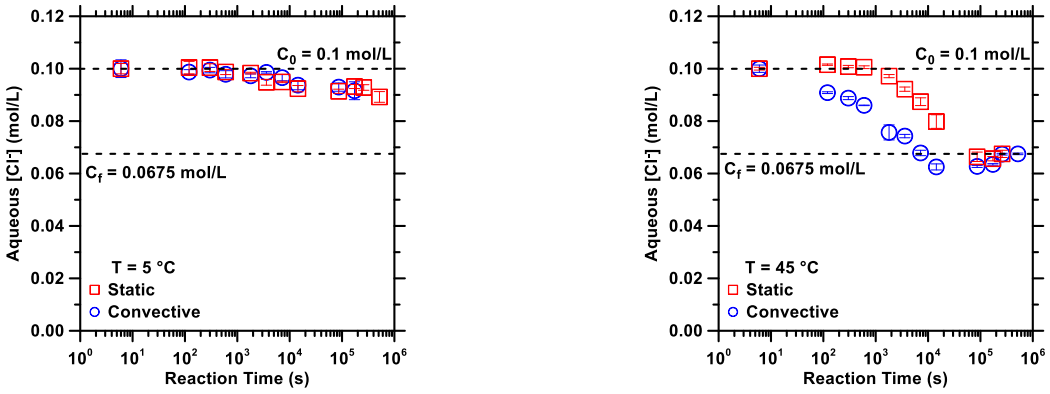

Figure 44: Representative Cl^- concentration evolutions as a function of time for NO_3-AFm undergoing ion-exchange under static and convective (stirred) mixing conditions for an initial Cl^- concentration of 0.1 mol/L at: **(a)** 5 ˚C, and, **(b)** 45 ˚C. Also shown are the initial (C_0) and final (C_f) concentrations of Cl^- ions that persist when ion-exchange begins, and completes.

Expectedly, increasing the concentration of exchangeable anions in the exposure solution increases the rate of ion-exchange (e.g., see Figure 45a). However, while exposure solutions with initial Cl^- concentrations C_0 = 0.1 mol/L and 1 mol/L present sufficient levels of exchangeable anions, this is not so when C_0 = 0.01 mol/L, where the solution is deficient in exchangeable species (i.e., to fully convert 1 g of AFm solids). As a result, with increasing ion-exchange the reaction rate drops not only because of incremental Cl^- (or NO_3^-) uptake, but also because of an exponential decrease in the driving force (i.e., chemical potential gradient) that provokes ion-exchange.

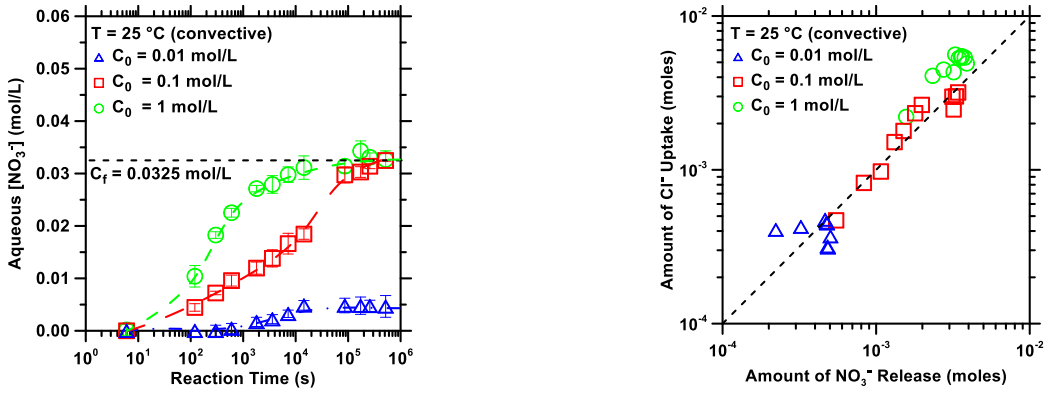

(a) **(b)**

Figure 45: (a) Representative NO_3^- ion concentrations as a function of time for convectively mixed NO_3-AFm systems undergoing ion-exchange (i.e., that are taking up Cl^- species) at 25 ˚C for initial chloride concentrations (C_0) of 0.01 mol/L, 0.1 mol/L and 1 mol/L. **(b)** An illustration of the stoichiometry of the NO_3-AFm ion-exchange reaction (see Equation 1) which illustrates that, as expected, per unit of Cl^- uptake into the AFm structure, a unit of NO_3^- species is released into the solution.

To accompany the Cl^- ion concentration measurements, and assess the stoichiometry of the ion-exchange process, parallel measurements of NO_3^- ion concentrations were also carried out for select systems (see Figure 45a). Expectedly, with the ejection of NO_3^- ions at the expense of Cl^- ions from the interlayer sites, the NO_3^- ion concentration in solution increases with time. Similar to the Cl^- assessments, the rate of NO_3^- increase amplifies with increased temperature, and convective mixing of the solution. Similar to Cl^- evolutions, the NO_3^- concentration in solution approaches a horizontal (asymptotic) plateau as the ion-exchange reaction completes (e.g., for C_0 = 0.1 mol/L and 1 mol/L), or as the concentration of exchangeable anions in the solutions diminishes to a level unsuitable for ion-exchange to continue. To assess the stoichiometry of the (forward) ion-exchange reaction, Figure 45(b) shows the amount of Cl^- taken-up into the AFm interlayer as a function of the amount of NO_3^- released into the solution. Throughout the duration of ion exchange, a near stoichiometric 1:1 ratio of Cl^-:NO_3^- is maintained in solution. This suggests that Cl^--for-NO_3^- exchange is rapid and thus no extrinsic means, e.g., the dissociation of water, is required to maintain electroneutrality in solution. Slight deviations from ideality as seen

in Figure 45(b) may be due to small changes in temperature during the measurements, and the somewhat slightly sub-stoichiometric nature of the ion-exchange reaction (e.g., 2 NO_3^- species in the AFm interlayer positions are exchanged by 1.95 Cl^- species per formula unit of AFm solid; see Equation 28).

In addition to "forward" ion-exchange, ion-exchange in the "reverse" direction was also tracked; i.e., as Cl-AFm converted to NO_3-AFm upon its exposure to a 0.1 mol/L NO_3^- solution under stirred conditions (not shown) at 5 ˚C and 45 ˚C. Similar to the data shown in Figure 44, the rate of ion-exchange; i.e., of Cl^- release and of NO_3^- uptake, increases with temperature, convective mixing vis-à-vis static solution conditions, and increasing concentration of exchangeable anions in the exposure solution. Despite the availability of NO_3^- species in solution, the solution concentration analysis indicate the "reverse" ion exchange reaction does not complete when T = 5 ˚C due to kinetic retardation; as confirmed by XRD analysis of the precipitates at the end of the experiment.

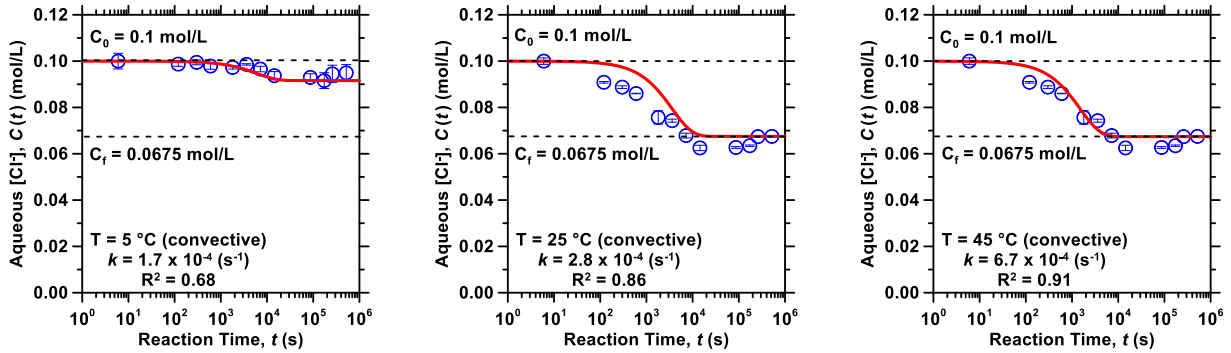

Figure 46: Representative evolutions of Cl^- ion concentrations as a function of time for NO_3-AFm systems undergoing ion-exchange in solutions having an initial Cl^- concentration of 0.1 mol/L under stirred conditions at: **(a)** 5 ˚C, **(b)** 25 ˚C and **(c)** 45 ˚C. The experimental data is fitted by a first-order reaction equation of the form: $C(t) = C_f + (C_0 - C_f)e^{-kt}$ where, C is the concentration (mol/L), t denotes time (seconds), k is the reaction rate constant (s^{-1}) and the subscripts '0' and 'f' indicate the initial and final ion concentrations, respectively.

Ion exchange reactions have often been modeled as a diffusion problem [198,199,200]. But, unless the rate-limiting step is well-known, force-fitting ion-exchange data to diffusion equations (e.g., see Crank [201]) only yields *lumped* diffusion constants that are indicative of all participating processes. To avoid such potentially misleading analyses, following critical evaluation, the measured kinetic data (e.g., see Figure 44) was fit to a generalized first-order reaction equation as shown in Figure 46. Such fittings to the measured data yield the rate constant of the ion-exchange reaction (k, s^{-1}), in both forward and reverse directions. In general, the high-quality fits are obtained, though the quality of fit (i.e., the coefficients of determination; R^2) are somewhat reduced for ion-exchange occurring at sub-ambient temperatures and dilute exposure solutions (where C_0 = 0.01 mol/L). It should also be noted that, when ion-exchange remained incomplete, and the ion concentrations plateaued at a value inferior to the expected equilibrium value – e.g., see Figure 46(a) – the value at which the concentrations plateaued was chosen as C_f for the sake of fitting.

First, it is noted that at 25°C, under static conditions, the reaction rate is effectively independent of the exposure solution concentration (see Figure 47a). However, under conditions of convective mixing, the reaction rate increases exponentially with an increase in solution concentration. This points to a significant role of transport effects on ion-exchange. Second, and as expected, the reaction rate constant increases with temperature. While convection in solution enhances the reaction rate constant, it does so by a *near-constant* value across all temperatures (see Figure 47b). Interestingly, Arrhenius analyses of the reaction rate constants (see Figure 47c) indicate that the activation energy of the forward ion-exchange reaction ($E_{a,F}$ = 38.2 ± 4.6 kJ/mol) is insensitive of the *mixing state* of the solution, i.e., whether the solution is stirred or not. Further, the reverse ion-exchange reaction (i.e., where Cl-AFm converts to NO_3-AFm; $E_{a,R}$ =

67.8 ± 8.2 kJ/mol) features an activation energy that is nearly double of the forward reaction. This is expected as Cl^- ions are favored to occupy the interlayer AFm positions vis-à-vis NO_3^- ions. Therefore, it is reasonable that a higher energy is needed to displace the preferred species (Cl^-) so as to facilitate occupation by the less preferred species (NO_3^-). To assess the reasonableness of the activation energy values, the enthalpy of the forward ion-exchange reaction (ΔH_r, kJ/mol; see Equation 28) was estimated [127,202]. This analysis indicates that ΔH_r = 36.2 kJ/mol. Next, given the first order nature of the ion-exchange reaction, its activation enthalpy ($\Delta H^{\ddagger}$, kJ/mol, where $E_a = \Delta H^{\ddagger} + RT$) was assessed from the rate constants (see Figures 46 and 47b) following transition-state theory (TST) and the well-known Eyring equation [203,204]:

$$k = \frac{k_B T}{h} e^{\left[\frac{\Delta S^{\ddagger}}{R} - \frac{\Delta H^{\ddagger}}{RT}\right]} \qquad \text{(equation 29a)}$$

$$\ln \frac{k}{T} = \frac{-\Delta H^{\ddagger}}{RT} + \ln \frac{k_B}{T} + \frac{\Delta S^{\ddagger}}{R} \qquad \text{(equation 29b)}$$

where, k is the reaction rate constant, $k_B$is Boltzmann's constant, h is Planck's constant, T is the thermodynamic temperature, $\Delta S^{\ddagger}$ and $\Delta H^{\ddagger}$ are entropy and enthalpy of activation, respectively. Analysis of the rate data using equation (29) reveals activation enthalpies around 38.2 kJ/mol and 67.8 kJ/mol for the forward and reverse ion-exchange reactions, respectively. These values are in excellent agreement with the activation energy estimated in Figure 47(c); thereby emphasizing the reasonableness of the values obtained. Coming back to the issue of rate controls on reaction, ion-exchange processes can feature a variety of rate controlling steps including [205,206]:

(1) Interdiffusion of exchangeable species within the solids,

(2) Diffusive transport of exchangeable species in bulk solution, and/or,

(3) Hindered diffusion of species into, and out of the Nernst diffusion layer (NDL) which is present in the vicinity of the solid surface.

By deduction, and inference, both (1) and (2) can be ruled out for ion-exchange in the AFm phases because: (i) if (1) were operative, the reaction rate constants shown in Figure 47(b) would be equal independent of the *mixing state* of the solution, and, (ii) the assessed activation energy values in the forward and the reverse directions suggest a (*near) surface-controlled* reaction [207,208]. This is anecdotally supported by the idea that the activation energies for ion transport in solution (e.g., diffusion, migration, etc.) are on the order of 10-to-20 kJ/mol [208,209]. While Rimstidt has carefully explained why E_a based assessments may be misleading to discriminate surface (i.e., interface) versus diffusion control in dissolution [210,211], for the case at hand (Figure 47c), where both static and mixed solution conditions yield similar activation energies – the data suggests that transport in solution is not rate limiting. This is because while solution viscosity and any changes therein would influence ion-transport in the static case, in the mixed solution where diffusion is not rate limiting, the effects of viscosity changes in solution are negated. Thus, by careful examination it can be deduced that hindered diffusion of ions through the NDL is the rate-limiting step. Herein, it should be noted that the specific "limiting step" is relevant to the rate at which ions displaced from the AFm interlayer are able to exit the NDL – an aspect which is aided by mixing the solution; which therefore explains why mixing amplifies the reaction rate constant by a constant offset, independent of reaction temperature, as shown in Figure 47(b).

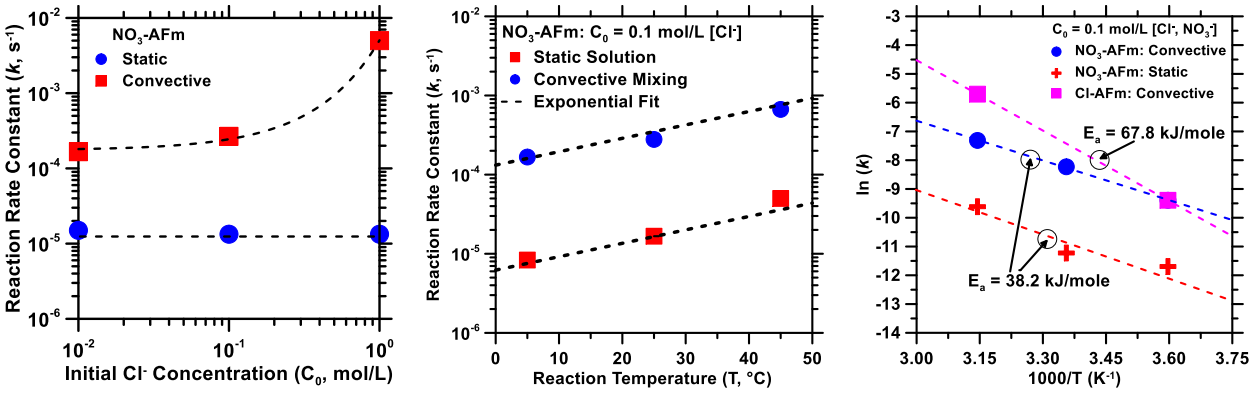

(a) **(b)** **(c)**

Figure 47: (a) The reaction rate constant as a function of the initial Cl^- concentration at 25°C. **(b)** The reaction rate constant as a function of temperature for NO_3-AFm systems transforming to Cl-AFm (via ion-exchange) in solutions with an initial Cl^- concentration (C_0) of 0.1 mol/L under static and convectively mixed conditions. The data are fitted by exponential functions of the form: y = Aexp(Bx) where A and B are numerical coefficients. The data corresponding to static and convectively mixed solution conditions are separated by a constant "y-offset". **(c)** An Arrhenius plot showing the natural logarithm of the reaction rate constant (k, s^{-1}) as a function of the inverse temperature for AFm systems undergoing ion-exchange in both in the forward (NO_3-to-Cl AFm) and reverse (Cl-to-NO_3 AFm) directions.

Analysis of Nernst diffusion layer: The circumstance of "film diffusion controlled ion exchange" (i.e., ion-exchange controlled by the NDL) was described by an analytical solution of the Nernst-Planck formulation within a finite volume as described in Equation (30) below [206]:

$$\left(1-a\bar{x}_B^{\infty}\right)\ln\left(1-U(t)\right)-\left(1-a\bar{x}_B^{\infty}-ab\right)\ln\left(1-\frac{U(t)}{1+b/\bar{x}_B^{\infty}}\right)=-ct \qquad \text{(equation 30a)}$$

$$a\equiv 1-\alpha_B^A;\ \text{where}\ \alpha_B^A=\frac{\bar{C}_A C_B}{\bar{C}_B C_A}\ \text{and}\ C_B(t)=\left[C_0V-\bar{C}_0\bar{V}\cdot U(t)\right]/V \qquad \text{(equation 30b)}$$

$$b\equiv\left[\left(\frac{1+w}{aw}\right)^2-\frac{4}{aw}\right]^{\frac{1}{2}};\ \text{where}\ w\equiv\frac{\bar{C}_0\bar{V}}{C_0V} \qquad \text{(equation 30c)}$$

$$c\equiv\frac{3ab\bar{V}D}{\delta r_0 V} \qquad \text{(equation 30d)}$$

$$\bar{x}_B^{\infty}=\frac{1+w}{2aw}-\frac{b}{2} \qquad \text{(equation 30e)}$$

where, C is the concentration (mol/L), V is the volume (L), D is the interdiffusion coefficient (m^2/s), δ is the film thickness (m), r_0 is the particle radius (m). Subscript A corresponds to the species initially within the AFm interlayer (i.e., NO_3^- for the forward reaction), subscript B corresponds to the exchangeable species within the solution (i.e., Cl^- in the forward reaction). The variables with overbars refer to the AFm solids, while those without overbars correspond to the solution. The analytical solution is derived under the assumptions that:

- Cl^- and NO_3^- ions show similar mobility (as described by the Nernst-Einstein equation [212]), such that no electric field arises, resulting in a constant interdiffusion coefficient *D*,
- Ionic interdiffusion across the film is quasi-stationary (i.e., diffusion across the film is fast relative to concentration changes at the NDL's boundaries) and 1-dimensional requiring that the particle radius $r_0 \gg$ film thickness δ,
- The separation factor α_B^A is a constant which indicates the selectivity of the ion exchanger (in this case, the AFm solids) for a given exchangeable species in solution.

Here, the separation factor α_B^A for the forward reaction was assumed to be zero (representing complete conversion of NO_3-Afm to Cl-Afm at the completion of ion exchange). In addition, the AFm particle radius was taken as its median diameter based on the measured particle size data (r_0 = 5 μm; as shown in Figure 42b).

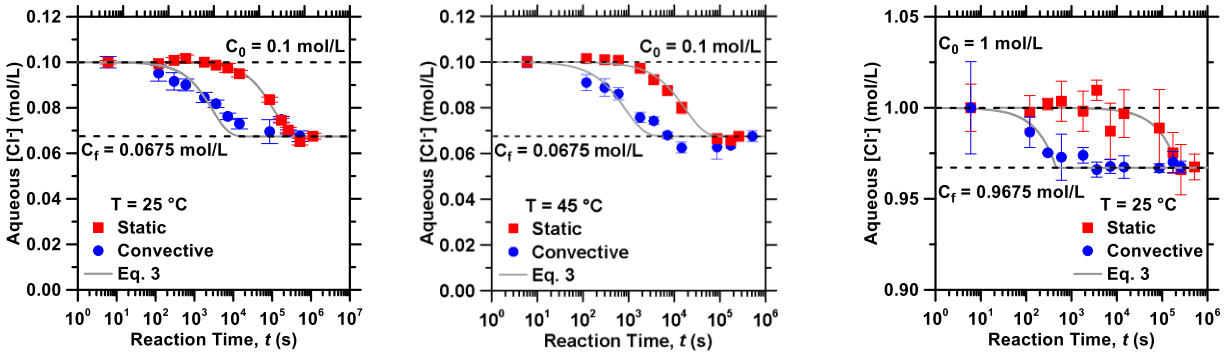

Figure 48: Representative comparisons of measured and calculated concentration profiles for ion-exchange in the forward direction (i.e., NO_3-AFm converting to Cl-AFm) for different combinations of reaction temperature and C_0: **(a)** C_0 = 0.1 mol/L Cl^-, T = 25°C, **(b)** C_0 = 0.1 mol/L Cl^-, T = 45°C, and, **(c)** C_0 = 1 mol/L Cl^-, T = 25°C.

Equation (30) was solved for both static and convective conditions of ion-exchange while varying the mass transfer coefficient through the NDL; i.e., the ratio "D/δ" (m/s, abbreviated as MTC). As seen in Figure 48, in general, favorable agreement with the experimental data can be obtained. Expectedly, the mass transfer coefficient is substantially larger – by 2-3 orders of magnitude – under conditions of convective mixing, as compared to a static solution; and increases with temperature. While this approach does quantitatively reveal the MTC, and its variations across the different reaction conditions; the coupling of D and δ prevents them from being individually quantified. Nevertheless, it is clear that a NDL (i.e., film controlled transport) is the rate-limiting step in ion-exchange processes in AFm-like layered double hydroxide solids.

Table 12: Representative parameters used in Equation (3) to replicate measured exchangeable ion concentrations in solution for the reaction conditions shown in Figure 7.

T (°C)	C_0 (mol/L)	D/δ, Convective Mixing (m/s)	D/δ, Static Solution (m/s)
25	1	2.5×10^{-8}	5.2×10^{-11}
25	0.1	2.9×10^{-8}	7.8×10^{-10}
45	0.1	1.0×10^{-7}	4.8×10^{-9}

Compositional conversions: To ascertain the role of ion-exchange on compositional changes in the AFm solids, the filtered particulates were examined by X-ray diffraction (XRD). Figure 49(a) shows the XRD patterns obtained following "forward direction" ion exchange in a convectively mixed 0.1 mol/L Cl^- solution across a range of temperatures. Additionally, Figure 49(b) shows the XRD patterns obtained following "forward direction" ion exchange at 25 °C across a range of exposure solution concentrations under static conditions. Across both mixing conditions, it is noted that increasing the temperature and Cl^- abundance in the solution aid and accelerate ion-exchange, and thus the conversion of NO_3-AFm to Cl-AFm.

In convectively mixed solutions, for the same exchangeable ion-abundance in solution (e.g., 0.1 mol/L), the extent of NO_3-AFm that is converted to Cl-AFm is larger as temperature increases; as indicated by Figure 49(a) based on relative XRD peak intensities. It is important to note however, when ion-exchange is incomplete (i.e., the NO_3-AFm partially converts to Cl-AFm) in the case of forward direction exchange; XRD patterns indicate the presence of NO_3-AFm and Cl-AFm as distinct components, i.e., no solid-solution is noted to form. Furthermore, it should be noted that at sub-ambient temperature – ion-exchange remains incomplete on account of retarded kinetics. On the other hand for C_0 = 0.01 mol/L Cl^- – independent of stirring, or not, ion-exchange remains incomplete – because the exposure solution is deficient in exchangeable anions (e.g., see Figure 49b). These results are in agreement with thermodynamic calculations shown in Figure 43(a) which indicate that, at equilibrium, complete ion exchange (i.e., NO_3-AFm conversion) will only be observed for $C_0 \geq 0.1$ mol/L Cl^- in the exposure solution.

AFm solids obtained following "reverse" ion-exchange were also examined by XRD; reflections of which are shown in Figure 50(a). It is seen that across temperatures, the Cl-AFm initially present has only partially transformed into NO_3-AFm; i.e., the ion-exchange reaction is

incomplete. The diffuse XRD reflections also indicate the presence of a Cl-NO_3-AFm solid solution. This is unlike the case of forward direction ion exchange (see Figure 8); wherein no solid-solution is observed. Balonis previously reported limited formation of solid-solution between Cl-AFm and NO_3-AFm in a range of compositions between 0.0-to-0.5 Cl-AFm/(Cl-AFm+NO_3-AFm) mole fraction; such that NO_3-AFm can accommodate up to 50% NO_3^- substitution by Cl^- ions [127]. For mole fractions above 0.50 a miscibility gap was observed at equilibrium. Therefore, it is perhaps unsurprising that limited formation of a solid-solution is observed as Cl-AFm is being progressively converted to NO_3-AFm. Thus it is proposed that while ion-exchange and compositional conversions amongst the AFm phases occur in "1-step" along the forward (i.e., NO_3-AFm converts to Cl-AFm) pathway; the reverse direction follows a "2-step" reaction pathway which involves the formation of a Cl-NO_3-AFm solid-solution as an intermediate compound. This pathway is illustrated in Figure 50(b).

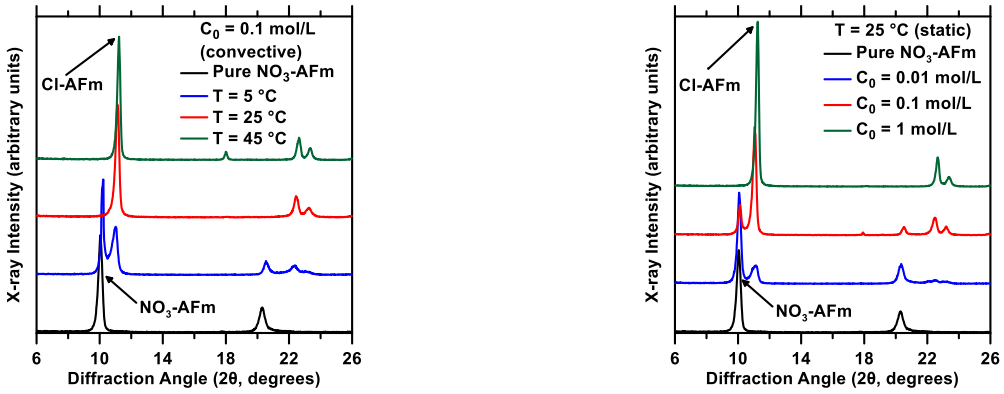

Figure 49: (a) Representative XRD reflections of the AFm solids following ion-exchange under convective mixing, for an initial concentration of the Cl^- solution (C_0) of 0.1 mol/L at T= 5 ˚C, 25 ˚C and 45 ˚C. **(b)** Representative XRD reflections of the AFm solids following ion-exchange for C_0 = 0.01 mol/L, 0.1 mol/L and 1 mol/L at T= 25 ˚C under static conditions. The XRD pattern for the NO_3-AFm precursor is shown for reference.

To model the formation of the Cl-NO_3-AFm solid solution, a model proposed by Guggenheim and refined by Redlich and Kister was applied (Equation 31) [213,214,215]. This model uses the

Guggenheim parameters to determine activity coefficients of each end-member ("pole") of the solid solution. The Guggenheim parameters suitable for a Cl-NO_3-AFm solid solution were obtained from Balonis [127] (a_0 = 0.188, a_1 =-2.49; N.B. the original compilation is missing the minus associated with a_1). This permits calculation of the activity coefficients (γ, unitless) for each pole using Equations 31(a-b) where, $X_{NO3-AFm}$ and X_{Cl-AFm} are the mole fractions of each pole in the solid solution and K is the equilibrium constant of a given pole (unitless); also known as the solubility product. By combining the solubility constants of each pole, with their mole fractions and activity coefficients [197], a total solubility product ($\Sigma\Pi_{eq,Sd}$, unitless) for the solid-solution (i.e., solidus curve, subscript "Sd"), as defined by Lippmann [216] can be calculated using Equation 31(c) [217].

$$ln\gamma_{NO3-AFm} = X_{Cl-AFm}{}^2\left(a_0 + a_1(3X_{NO3-AFm} - X_{Cl-AFm})\right) \quad \text{(equation 31a)}$$

$$ln\gamma_{Cl-AFm} = X_{NO3-AFm}{}^2\left(a_0 - a_1(3X_{Cl-AFm} - X_{NO3-AFm})\right) \quad \text{(equation 31b)}$$

$$\Sigma\Pi_{eq,Sd} = K_{NO3-AFm}\,X_{NO3-AFm}\,\gamma_{NO3-AFm} + K_{Cl-AFm}\,X_{Cl-AFm}\,\gamma_{Cl-AFm} \quad \text{(equation 31c)}$$

Knowledge of the total solubility product ($\Sigma\Pi_{eq,Sd}$, unitless) of the solid-solution allows calculation of the mole fractions of the pole components in the aqueous phase, and thus trace the solutus curve (subscript "Sl") as a function of composition of the poles using Equations 31(d-f) [218]. The Lippmann diagram shown in Figure 51(a) shows the deviation from ideal behavior of the solids and aqueous phases as a function of composition. In addition, Equations 32(a-c) permit calculation of the Gibbs energy of ideal mixing (ΔG_{id}), the excess Gibbs energy of mixing (ΔG_{ex}) and the molar Gibbs energy of mixing (ΔG_M) of the NO_3-AFm and Cl-AFm two component system.

$$X_{NO3,aq} = \frac{K_{NO3-AFm}\, X_{NO3-AFm}\, \gamma_{NO3-AFm}}{\Sigma \Pi_{eq,Sd}} \quad \text{(equation 31d)}$$

$$X_{Cl,aq} = \frac{K_{Cl-AFm}\, X_{Cl-AFm}\, \gamma_{Cl-AFm}}{\Sigma \Pi_{eq,Sd}} \quad \text{(equation 31e)}$$

$$\Sigma \Pi_{eq,Sl} = \frac{1}{\frac{X_{NO3,aq}}{K_{NO3-AFm}\ \gamma_{NO3-AFm}} + \frac{X_{Cl,aq}}{K_{Cl-AFm}\ \gamma_{Cl-AFm}}} \quad \text{(equation 31f)}$$

$$\Delta G^{id} = RT \sum X_i ln X_i \quad \text{(equation 32a)}$$

$$\Delta G^{ex} = RT \sum X_i ln \gamma_i \quad \text{(equation 32b)}$$

$$\Delta G^{Mix} = \Delta G^{id} + \Delta G^{ex} \quad \text{(equation 32c)}$$

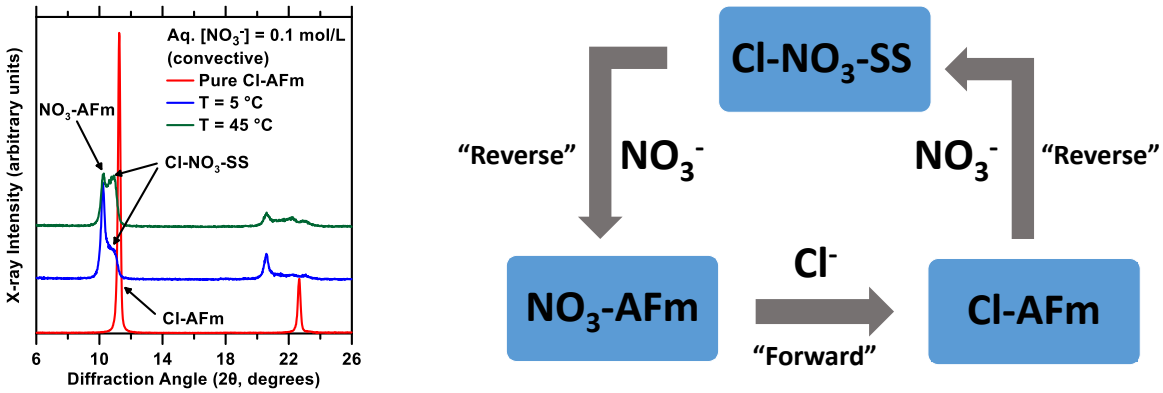

Figure 50: (a) Representative XRD reflections of the AFm solids following ion exchange for an initial concentration of the NO_3^- solution of 0.1 mol/L at 5 ˚C and 45 ˚C under convective mixing conditions. The XRD pattern of the Cl-AFm precursor is shown for reference. All data shown corresponds to "reverse direction" ion exchange reactions. **(b)** A schematic of the ion-exchange pathway for the thermodynamically preferred ("forward") and non-preferred ("reverse") directions showing the formation of a solid-solution as an intermediate step in the "reverse" direction of ion-exchange.

In accordance with the experimental data of Balonis [127], the excess free energy curve shows the existence of a limited solid-solution as NO_3-AFm is exposed to Cl^- species (i.e., in the region $0 \leq X_{Cl\text{-}AFm} \leq 0.45$, mole fraction; see Figure 51b). This is because, due to the more favored position of Cl^- in the AFm interlayer, NO_3-AFm tolerates the simultaneous coexistence of Cl^- species in

its structure. On the other hand, when $X_{Cl\text{-}AFm} \geq 0.45$ a miscibility gap emerges such that NO_3-AFm and Cl-AFm would co-exist, until progressively, all the NO_3-AFm converts to Cl-AFm. This explains why in the forward direction a solid-solution is not observed – due to its more favored position, Cl^- uptake rapidly converts NO_3-AFm such that either two distinct phases exist, or NO_3-AFm decomposes fully at the expense of Cl-AFm (e.g., see Figure 49). On the other hand, when Cl-AFm is exposed to NO_3^- species, initially two components, i.e., NO_3-AFm and Cl-AFm coexist. However, as the ion-exchange reaction proceeds, a limited solid-solution forms as Cl^- is progressively displaced from the AFm interlayer. As a result, a Cl-NO_3-AFm solid solution, and a discrete NO_3-AFm compound are noted to exist (see Figure 50a). While this does indicate that the ion-exchange reaction is incomplete (since NO_3-AFm is not the only compound that exists), it explains the observations in Figure 50(a) and corroborates the reaction pathway proposed in Figure 50(b). Taken together, the outcomes of this paper improve our understanding of kinetic and thermodynamic factors influential in AFm/LDH ion-exchange reactions.

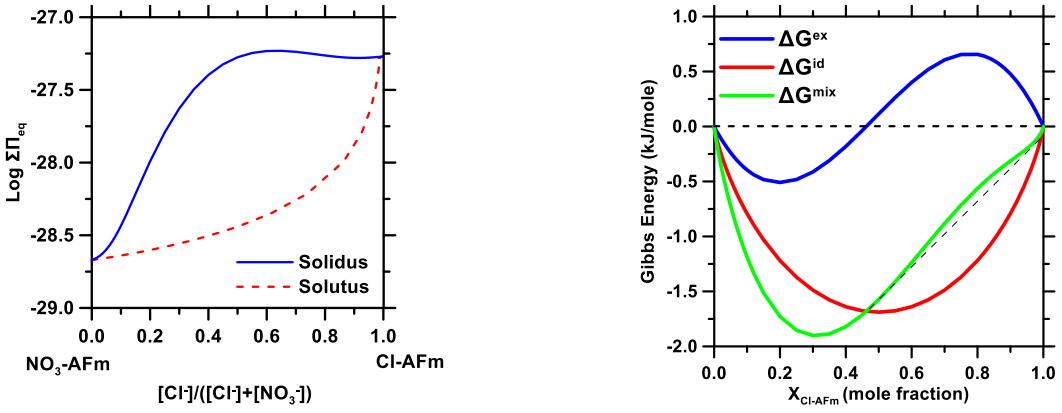

Figure 51: (a) A Lippmann diagram showing solidus and solutus traces for a solid-solution with end-members comprising NO_3-AFm (Pole 0) and Cl-AFm (Pole 1). **(b)** The Gibbs energy of ideal mixing (ΔG_{id}), excess Gibbs energy of mixing (ΔG_{ex}) and the molar Gibbs energy of mixing (ΔG_M) calculated using Equation (5) for the two component system comprising NO_3-AFm and Cl-AFm are shown.

6.6 Summary and Concussions Chapter 6

This study has rigorously examined the kinetics of monovalent ion-exchange in the AFm sub-group of layered double hydroxides (LDHs). Special attention is paid to understand the rate at which NO_3-AFm would exchange its interlayer anions to form Cl-AFm (and vice-versa). The rate of ion-exchange is noted to be influenced by three factors: (i) the concentration of exchangeable anions in the exposure solution, (ii) reaction temperature, and (iii) the state of the solution, i.e., whether it is mixed or not. The activation energy (E_a) of the forward ion-exchange reaction is estimated as 38.2 ± 4.6 kJ/mol; a value which is in agreement with both the activation enthalpy, and enthalpy of reaction of such a process. The rate of ion-exchange is found to be limited by the transport of species exiting the Nernst Diffusion Layer – i.e., a near-surface process – whose rate is described by a mass transfer coefficient (MTC; D/δ). This MTC varies by 2-3 orders of magnitude depending on the solution conditions (i.e., stirred or not), reaction temperature, etc.

Compositional alterations including the completion of ion-exchange reaction, or incompletion thereof, are correlated with the formation of solid solutions, and the existence of a miscibility gap – in relation to the direction of ion-exchange (i.e., forward or reverse), temperature and the abundance of exchangeable anions in the exposure solution. Specifically, for C_0 = 0.01 mol/L, ion-exchange remains incomplete (with the rate showing an asymptotic decay) independent of other extrinsic variables. Ion-exchange in the favored forward direction completes rapidly in 1-step, while reverse direction ion-exchange presents the transient formation of a Cl-NO_3-AFm solid solution; a view that is supported by thermodynamic data. Altogether, the outcomes improve our understanding of the kinetic and thermodynamics factor at the origin of monovalent

anion exchange in AFm, and LDH compounds. This has applications in optimizing the synthesis of such compounds, and modeling their performance in functional “ion-exchange” applications.

Chapter 7: General Conclusions

7.1 Scope of Chapter 7

This chapter provides the general conclusion of this research work. Detail explanations, specifics and outcomes of any of the subjects treated can be found in each chapter of this document and in the publication record of the author.

7.2 General Conclusions of this Research Work

Through the use of extensive experimental and analytical work, this research has sought to expand the use of powdered limestone is cementitious formulations as a means to a more sustainable material. While physical and chemical effects have been elucidated, limitations on further expansion of limestone use remain. This research has contributed to the field of construction materials and sustainability by stablishing the following:

- Despite provision of basic chemical precursors, including a suitable alumina source, for calcium carboaluminate formation (limestone reaction), calcite partake in hydration is limited. This was concluded to be on account of one or a combination of two factor: i) limited provision of CO_3^{2-} species in solution as limestone solubility and slow dissolution rate (as compared to normal cement solid phases i.e., C_3A, C_3S) and ii) limitations in the ion exchange reactions leading to limited carboaluminate (CO_3-AFm) formation despite provision of ionic species in solution.
- To study the first proposed limitation for calcite partake in hydration reactions, a highly soluble carbonate salt (Na_2CO_3) was used as a source for carbonate species in a calcium aluminate cement. However, it was found that the provision of large amounts of a highly soluble carbonate salt does not increase the amount of calcium phases, in fact, it appears to be detrimental. The reasons for this were found to be: i) formation of alternative

carbonate hydration products containing high alkali (in this particular case Na^+ i.e., thermonatrite) and calcium content (i.e., gaylussite). These phases compete for carbonate, calcium species and water hindering calcium carbonate formation. ii) the large concentration of alkali species in solution appears to destabilize calcium carboaluminate phases over the long periods of time leading to dissolution of any previously formed calcium carboaluminate phase in the long term. The former factor implies that carbonate and calcium content are both a prerequisite for a suitable carbonate source, in addition to the dissolution/solubility qualities, if calcium carbonate phase formation is intended. The latter factor points to a scenario in which it is possible that AFm phases are subject to water activity stability and that formation/stability is not only a function of provision of suitable precursor.

- The second proposed limitation for calcium carboaluminate formation was thought to be limited ion exchange in the AFm phases. However, this research has shown that ion exchange in AFm phases is, at room temperature and under non-convective mixing conditions (as those found in the solid/pore solution environments in cementitious systems), mainly a function of ionic concentration. Furthermore, kinetics of ion exchange reaction is also regulated by the existence of a Nernst Diffusion Layer which regulates the exchange of species in and out of the exchanger (AFm or LHD particle). This conclusion in important as ion replacement at the AFm interlayer is what regulates the variations in monosulfoaluminate-carboaluminate fractions as well as ettringite stability in OPC systems.

Chapter 8: Future Work

8.1 Scope of Chapter 8

This chapter intents top provide insights on possible future investigations related to limestone activation and cement chemistry in general, this based on the findings of the present research work as well as literature currently available.

8.2 Future Research

In this work, the physical and chemical effects of limestone in binder formulations have been explained. However, further research is required as a means to a more sustainable binder in which use of limestone can be further extended without detrimental effects on mechanical properties. Some of the most interesting directions for future research are: i) the study of the mechanical properties (i.e., modulus of elasticity and compressive strength) of alumina activated limestone-OPC systems, ii) the ion exchange kinetics of AFm phases where divalent (SO_4^{2-}, CO_3^{2-}, etc..) monovalent (Cl^-, NO_3^-, etc..) anions are exchanged or where anionic charge of exchanging species is different, iii) the stability of hydrotalcites (magnesium-alumino LDH's) with respect to the different anions present in cementitious systems, iv) the expansive (likely harmful but beneficial if controlled) properties of NO_3-AFm due to its ability to show incremental water content, just to mentioned a few.

The rheological and mechanical properties of formulations with large limestone contents have been studied previously [15,122]. However, the systems studied have not intended on limestone activation (extended carboaluminate phase formation) and hence the volumetric fractions of typical hydrated phases might be different. While the present study has shown that compressive strength, despite higher carboaluminate phase formation, remains mostly a function of C-S-H

content (chapter 4), the modulus of elasticity as well as rheological properties of such formulations might vary on account of the different fractions of hydrated compounds/phases formed (as compared to typical OPC systems) which themselves also show different mechanical properties [219,220]. Linking the amount of carboaluminate phase formation, or the amount of limestone that remains reactive and unreactive, with changes in mechanical/rheological properties is a crucial step for determining characteristics of future, and more sustainable, binder formulations.

While the kinetics of ion exchange in AFm phases (calcium-alumino LDH's) has been studied by the use of Cl^- and NO_3^- inions (monovalent) in this research program, the question of kinetics when anions of different charges are exchanged (i.e., monovalent by divalent anion) still remains. It is expected than when anions of similar electrical charges are exchanged, a one to one replacement is in order to maintain electroneutrality of the system. However, when an anion replaces another with a different electric charge at the AFm interlayer, the substitution is not expected to occur on a one to one basis. The effects of this substantial difference in the kinetics of ion exchange still remains to be studied. As shown in chapter 6, multiplicity of ion exchange reactions are used in the production of LDH's for specific applications but in most cases these ion exchange reactions are not carried out using anions of similar electric charges [221]. Furthermore, while the hierarchy of occupancy of the AFm interlayer under equilibrium conditions (Cl^->NO_3^->NO_2^->CO_3^{2-}>SO_4^{2-}>OH^-) has been studied [21,80,98,69], kinetic effects of exchange amongst most of the species found at the AFm interlayer remains largely unstudied, with most data available focusing on equilibrium conditions.

Other relevant factor in ion exchange reactions has to do with the formation of solid solutions in which the interlayer space is shared by multiple anions. While many solid solutions in cementitious systems have been studied (i.e., hydrogrossular, C-S-H, AFm, etc….), the effects of solid solution formation on the kinetics of the ion exchange have not been studied. A clear example can be taken from this research in which no solid solution formation can be detected in the forward ion exchange reaction (see chapter 6) from NO_3-AFm to Cl-AFm in a highly Cl^- concentrated environment, but once the reaction is reversed from Cl-AFm to NO_3-AFm in a highly NO_3^- concentrated environment, a solid solution forms in which NO_3^- and Cl^- anions coexist at the interlayer. The formation of such type of solid solution could have effects in the kinetics of ion exchange as such solid solution forms around the pristine Cl-AFm bringing about a diffusion barrier that exits in only one reaction direction (figure 58). As the ions go through this solid solution barrier, total conversion to NO_3-AFm happens in the outside and the solid solutions barrier moves inwards consuming the pristine Cl-AFm and transforming it into solid solution. Eventually, if NO_3^- concentrations remain high, total consumption of the pristine Cl-AFm will happen and the solid solution will in turn transform into NO_3-AFm. In the case of the forward reaction, this solid solution barrier does not occur and phase transformation occurs more readily. This findings might imply that limited formation of solid solutions might actually be an intermediate step in conversion of AFm phases.

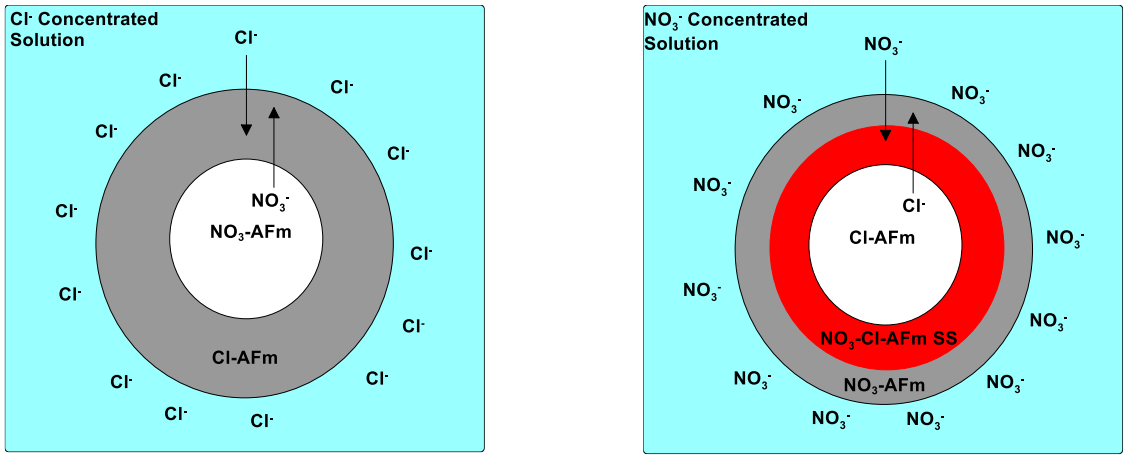

(a) (b)

Figure 52: Schematic representation of ion exchange reaction in the (a) forward and (b) reverse directions.

In addition to the AFm, other layered double hydroxides present in cementitious systems are the calcium-magnesium "hydrotalcite-like" layered hydrates. While the AFm contains partial calcium replacement by aluminum in a portlandite type of structure leading to the presence of the negatively charged interlayer, hydrotalcites present in cement show partial magnesium replacement by aluminum in a brucite type of structure leading also to the presence of a neutralizing interlayer. In fact, layered double hydroxides were initially termed "hydrotalcite-like" compounds [222] as they are much more commonly found in nature as compared to the calcium-aluminum layered structures formed in cementitious systems (AFm). Unlike AFm phases, the hierarchy of occupancy of anions, as those commonly found in OPC systems, at the interlayer appears to be not well studied [**Error! Bookmark not defined.**] and while some solubility data is acquired experimentally [223], the implementation of these data sets into thermodynamic simulations has not been carried out. During the course of this research, thermodynamic equilibrium simulations showed the hydroxyl anion (OH^-) as the more stable species, as compared to other anions such as sulfate, carbonate and even chloride, the latter has been

experimentally measure by Miyata [Error! Bookmark not defined.]. This result is in direct contradiction to experimental results carried out with AFm phases.

While the reasons for studying the calcium-aluminum (AFm), instead of the calcium-magnesium variant of LDH's, in OPC systems relies mainly on the low MgO content present in normal cements, this factor effectively limits the potential for calcium-magnesium layered structure formation. However, the use of magnesite ($MgCO_3$), after decarbonation, in combination with portlandite ($Ca(OH)_2$) might bring new light on the behavior of this compound, and if, OH^- ions are amongst the most stable in cementitious systems (as calculated using currently available fields of stability and as stated by Miyata [Error! Bookmark not defined.]), the addition of a reactive magnesium source in OPC in junction with a larger $Ca(OH)_2$ content, might bring about the water intake required to produce a reduction in porosity values while maintaining mechanical properties. Such reactive source of magnesium is not likely to be a normally stable magnesium mineral, as those found in nature (i.e., magnesite, dolomite, etc...) on account of their low solubility and dissolution rate at pH levels as those found in cementitious systems [224]. Instead, a more soluble magnesium salt should be used (i.e., MgCl2). Similar salts (i.e., CaCl2) have been studied in cementitious systems [69,184], the effects have been noticed to include an acceleration in cement hydration as well as a higher risk of corrosion due to the high chloride concentration levels in pore solution which eventually lead to early reinforcement damage. This might also be a problem with the use of highly soluble $MgCl_2$ as the formation of metastable corrosion products on steel reinforcement would occur [225].

Another interesting observation in this research was the multiplicity of water formula units shown by the NO_3-AFm phase as a function of water availability. While NO_3-AFm appears to be

a suitable compound for bypassing conversion processes in CAC systems [58], the expansion of this phase when water availability increases can be harmful [226]. While expansion of different AFm phases has be studied previously [227], potential for NO_3-AFm expansion in cement remains less understood. This is particularly problematic in mortar or concretes exposed to large periods of wet/dry cycles as the expansion of NO_3-AFm can induce stress in the binder matrix and cracking, possibly in a way similar to what occurs during late ettringite formation [228]. While the harmful consequences of NO_3-AFm expansion not fully understood yet, the possible applications in reduced shrinkage formulations or water release for internal curing can also be envisioned by the tailoring the amount of NO_3-AFm in cementitious systems, although, a broad research program would be required before suitable proportions/products for industrial applications are found.

The feasibility of limestone as a reactive component of cementitious binders also depends on the stability of the AFm phase over time. In this research, it was found that carboaluminate phases might become instable over time (chapter 5) when condition of low water activity occur. This is problematic as large sulfate or alkali concentrations can occur over time leading to a destabilization of some of the AFm phases present in the matrix. In cases where carboaluminate formation has been targeted for suitable mechanical properties at low clinker factors, this type of concentration increase due to sulfate or alkali penetration can reduce water activity and lead to decomposition of carboaluminate phases which, in this particular type of formulation, are fundamental for good mechanical behavior. Such situation can lead to problems similar to those of CAC systems undergoing conversion phenomena where reduction in compressive strength and even failure might occur at later ages [56]. Research on water activity effects on C_3S hydration has been carriedout through the use of varying fractions of water and isopropanol in

the liquid phase of systems [229], a similar approach can be proposed to determine the stabilities of different AFm phases with respect to different water activity values.

Reference List

[1] E. Worrell, L. Price, N. Martin, C. Hendriks, and L. Ozawa-Meida. "Carbon dioxide emissions from the global cement industry 1." Annual review of energy and the environment 26, no. 1 (2001): 303-329.

[2] C. A. Hendriks, E. Worrell, D. De Jager, K. Blok, and P. Riemer. "Emission reduction of greenhouse gases from the cement industry." InProceedings of the fourth international conference on greenhouse gas control technologies, pp. 939-944. 1998.

[3] M. Schneider, M. Romer, M. Tschudin, and H. Bolio. Sustainable cement production—present and future. Cement and Concrete Research 41, no. 7 (2011): 642-650.

[4] D. J. M Flower, and J.G. Sanjayan. Green house gas emissions due to concrete manufacture. The International Journal of Life Cycle Assessment12, no. 5 (2007): 282-288.

[5] P. K. Mehta. High-performance, high-volume fly ash concrete for sustainable development. In Proceedings of the international workshop on sustainable development and concrete technology, pp. 3-14. Ames, IA, USA: Iowa State University, 2004.

[6] M. L. Berndt. Properties of sustainable concrete containing fly ash, slag and recycled concrete aggregate. Construction and Building Materials 23, no. 7 (2009): 2606-2613.

[7] D. W. S. Ho, and R. K. Lewis. Carbonation of concrete and its prediction. Cement and Concrete Research 17, no. 3 (1987): 489-504.

[8] V. G. Papadakis, M. N. Fardis, and C. G. Vayenas. Hydration and carbonation of pozzolanic cements. ACI Materials Journal 89, no. 2 (1992): 119-130.

[9] S. G. Tsivilis, E. C. Batis, Gr. Grigoriadis, and D. Theodossis. Properties and behavior of limestone cement concrete and mortar. Cement and Concrete Research 30, no. 10 (2000): 1679-1683.

[10] A. A Ramezanianpour, E. Ghiasvand, I. Nickseresht, M. Mahdikhani, and F. Moodi. Influence of various amounts of limestone powder on performance of Portland limestone cement concretes. Cement and Concrete Composites31, no. 10 (2009): 715-720.

[11] G. V. B. B. Menéndez, V. Bonavetti, and E. F. Irassar. Strength development of ternary blended cement with limestone filler and blast-furnace slag. Cement and Concrete Composites 25, no. 1 (2003): 61-67.

[12] M. Heikal, H. El-Didamony, and M. S. Morsy. Limestone-filled pozzolanic cement. Cement and Concrete Research 30, no. 11 (2000): 1827-1834.

[13] Standard, A. S. T. M. Annual book of ASTM standards. American Society for Testing and Materials Annual, Philadelphia, PA, USA 4, no. 04.08 (2004).

[14] B. Lothenbach, G. Le-Saout, E. Gallucci, and K. Scrivener. Influence of limestone on the hydration of Portland cements. Cement and Concrete Research 38, no. 6 (2008): 848-860.

[15] V., Kirk, M. Aguayo, T. Oey, G. Sant, and N. Neithalath. Hydration and strength development in ternary Portland cement blends containing limestone and fly ash or metakaolin. Cement and Concrete Composites 39 (2013): 93-103.

[16] E. Berodier, and K. Scrivener. Understanding the Filler Effect on the Nucleation and Growth of C-S-H. Journal of the American Ceramic Society 97, no. 12 (2014): 3764-3773.

[17] T. Oey, A. Kumar, J. W. Bullard, N. Neithalath, and G. Sant. The filler effect: the influence of filler content and surface area on cementitious reaction rates. Journal of the American Ceramic Society 96, no. 6 (2013): 1978-1990.

[18] J. Kaufmann, F. Winnefeld, and D. Hesselbarth. Effect of the addition of ultrafine cement and short fiber reinforcement on shrinkage, rheological and mechanical properties of Portland cement pastes. Cement and Concrete Composites 26, no. 5 (2004): 541-549.

[19] D. P. Bentz, Influence of water-to-cement ratio on hydration kinetics: simple models based on spatial considerations. Cement and Concrete Research 36, no. 2 (2006): 238-244.

[20] K. Scrivener, J. L. Cabiron, and R. Letourneux. High-performance concretes from calcium aluminate cements. Cement and concrete research 29, no. 8 (1999): 1215-1223.

[21] T. Matschei, B. Lothenbach, and F. P. Glasser. The AFm phase in Portland cement. Cement and Concrete Research 37, no. 2 (2007): 118-130.

[22] A. P. Luz, and V. C. Pandolfelli. $CaCO_3$ addition effect on the hydration and mechanical strength evolution of calcium aluminate cement for endodontic applications. Ceramics International 38, no. 2 (2012): 1417-1425.

[23] V. Manovic, and E. J. Anthony. CaO-based pellets supported by calcium aluminate cements for high-temperature CO_2 capture. Environmental science & technology 43, no. 18 (2009): 7117-7122.

[24] B. Lothenbach, T. Matschei, G. Möschner, and F. P. Glasser. Thermodynamic modelling of the effect of temperature on the hydration and porosity of Portland cement. Cement and Concrete Research38, no. 1 (2008): 1-18.

[25] T. Schmidt, B. Lothenbach, M. Romer, J. Neuenschwander, and K. Scrivener. Physical and microstructural aspects of sulfate attack on ordinary and limestone blended Portland cements. Cement and Concrete Research 39, no. 12 (2009): 1111-1121.

[26] S. A. Hartshorn, J. H. Sharp, and R. N. Swamy. Thaumasite formation in Portland-limestone cement pastes. Cement and Concrete Research 29, no. 8 (1999): 1331-1340.

[27] E. F. Irasser, D. Violini, V. F. Rahhal, C. Milanesi, M. A. Trezza, V. L. Bonavetti, Influence of limestone content, gypsum content and fineness on early age properties of Portland limestone cement produced by inter-grinding. Cement and Concrete Composites 33 (2011), 192-200.

[28] S. Tsivilis, E. Chaniotakis, G. Kakali, G. Batis, An analysis of the properties of Portland limestone cements and concrete. Cement and Concrete Composites 24 (2002), 371-378.

[29] S. Tsivilis, E. Chaniotakis, E. Badogiannis, G. Pahoulas, and A. Ilias, A study on the parameters affecting the properties of Portland limestone cements. Cement and concrete composites 21, no. 2 (1999) 107-116.

[30] L. Opoczky, Grinding technical questions of producing composite cement. International Journal of Mineral Processing 44 (1996): 395-404.

[31] C. Ferraris, F. Chiara, A. Vincent, A. I. Avilés, Measurement of particle size distribution in Portland cement powder: analysis of ASTM round robin studies. Cement, concrete and aggregates 26 (2004) 1-11.

[32] D. P. Bentz, D.P., Blending Different Fineness Cements to Engineer the Properties of Cement-Based Materials. Magazine of Concrete Research, 62 (2010) 327-338.

[33] E.J. Garboczi and J.W. Bullard, Shape analysis of a reference cement. Cement and concrete Research 34 (2004) 1933-1937.

[34] A. Kumar, T. Oey, S. Kim, D. Thomas, S. Badran, J. Li, F. Fernandes, N. Neithalath, G. Sant, Simple methods to estimate the influence of limestone fillers on reaction and property evolution in cementitious materials. Cement and Concrete Composites (2012).

[35] D. P. Bentz, A. S. Hansen, J. M. Guynn, Optimization of Cement and Fly Ash Particle Sizes to Produce Sustainable Concretes. Cement and Concrete Composites 33 (2011) 824-831.

[36] D. P. Bentz, T. Barrett, I. De la Varga, W.J. Weiss, Relating Compressive Strength to Heat Release in Mortars. Advances in Civil Engineering Materials (2012), in press.

[37] J. J. Thomas, A new approach to modeling the nucleation and growth kinetics of tricalcium silicate hydration, Journal of the American Ceramic Society. 90 (2007) 3282–3288.

[38] S. Garrault, A. Nonat, Hydrated layer formation on tricalcium and dicalcium silicate surfaces: experimental study and numerical simulations, Langmuir 17 (2001) 8131–8138.

[39] V. K. Peterson, M.C.G. Juenger, Hydration of tricalcium silicate: effects of $CaCl_2$ and sucrose on reaction kinetics and product formation, Chemistry of Materials 18 (2006) 5798–5804.

[40] N. Tenoutasse, A. de Donder, The kinetics and mechanism of hydration of tricalcium silicate, Silicates Ind. 35 (1970) 301–307.

[41] J. W. Cahn, The kinetics of grain boundary nucleated reactions, Acta Metallurgica 4 (1956) 449–459.

[42] J. W. Christian, The Theory of Transformations in Metals and Alloys, Part 1, 3rd edition, Pergamon Press, Oxford, 2002.

[43] J. J. Thomas, H.M. Jennings, Effects of D2O and mixing on the early hydration kinetics of tricalcium silicate. Chemistry of Materials 11 (1999) 1907–1914.

[44] G. W. Scherer, J. Zhang, J. J. Thomas, Nucleation and growth models for hydration of cement. Cement and Concrete Research 42 (2012) 982-993.

[45] G. W. Scherer, Models of confined growth. Cement and Concrete Research 42 (2012) 1252-1260.

[46] J. J. Biernacki, and T. Xie. An advanced single particle model for C_3S and alite hydration. Journal of the American Ceramic Society 94, no. 7 (2011): 2037-2047.

[47] T. Sato, and F. Diallo. Seeding effect of nano-$CaCO_3$ on the hydration of tricalcium silicate. Transportation Research Record: Journal of the Transportation Research Board 2141 (2010): 61-67.

[48] D. P. Bentz, E. F. Irassar, B. Bucher, W. J. Weiss, Limestone Fillers to Conserve Cement in Low w/cm Concretes: An Analysis Based on Powers' Model, Concrete International, 31 (2009) 41-46.

[49] V. Bonavetti, H. Donza, G. Menendez, O. Cabrera, E.F. Irassar, Limestone filler cement in low w/c concrete: a rational use of energy. Cement and Concrete Research. 33 (2003) 865–871.

[50] Concrete for the Environment. Published on Behalf of the Nordic Network Concrete for Environment by SP Swedish National Testing and Research Institute, Boras, Sweden, June 2003.

[51] W. Gutteridge, J. Dalziel. Filler cement: the effect of the secondary component on the hydration of Portland cement: part I. A fine non-hydraulic filler. Cement and Concrete research. 1990; 20: 778-782.

[52] B. Lothenbach, K. Scrivener, R. D. Hooton. Supplementary cementitious materials. Cement and Concrete Research. 2011; 41: 1244-1256.

[53] C. Martin, P. Lawrence, E. Ringot. Efficiency of mineral admixtures in mortars: quantification of the physical and chemical effects of fine admixtures in relation with compressive strength. Cement and Concrete Research. 2006; 36: 264-277.

[54] A. Kumar, T. Oey, G. Puerta-Falla, R. Henkensiefken, N. Neithalath, G. Sant. A comparison of intergrinding and blending limestone on reaction and strength evolution in cementitious materials. Construction and Building Materials. 2013; 43: 428-435.

[55] Z. Maciej, S. K. Bremseth, M. Whitehead, M. B. Haha. Effect of $CaMg(CO_3)_2$ on hydrate assemblages and mechanical properties of hydrated cement pastes at 40° C and 60° C. Cement and Concrete Research. 2014; 65: 21-29.

[56] K. Scrivener, A. Capmas, Calcium aluminate cements, Chapter 13, in: P.C. Hewlett (Ed.), Lea's Chemistry of Cement and Concrete, John Wiley & Sons, New York, 1998.

[57] B. Lothenbach, L. Pelletier-Chaignat, F. Winnefeld. Stability in the system $CaO–Al_2O_3–H_2O$. Cement and Concrete Research. 2012; 42: 1621-1634.

[58] G. Falzone, M. Balonis, G. Sant. X-AFm stabilization as a mechanism of bypassing conversion phenomena in calcium aluminate cements. Cement and Concrete Reseasrch. 2015; 72: 54-68.

[59] A. Kumar, J. Reed, G. Sant. Vertical Scanning Interferometry: A New Method to Measure the Dissolution Dynamics of Cementitious Minerals. Journal of the American Ceramic Society. 2013; 96: 2766-2778.

[60] A. Luttge, U. Winkler, A.C. Lasaga. Interferometric study of the dolomite dissolution: a new conceptual model for mineral dissolution. Geochimica et Cosmochimica Acta 2013; 67: 1099-1116.

[61] S. Mindess, S. Diamond. SEM investigations of fracture surfaces using stereo pairs: II. Fracture surfaces of rock-cement paste composite specimens. Cement and Concrete Research. 1992; 22: 678-688.

[62] C. Gosselin, E Gallucci, K. Scrivener. Influence of self heating and Li_2 SO_4 addition on the microstructural development of calcium aluminate cement. Cement and Concrete Research. 2010; 40: 1555-1570.

[63] M. S. Siddiqui, W. Nyberg, W. Smith. B. Blackwell, K. R. Riding. Effect of curing water availability and composition on cement hydration. ACI Materials Journal. 2013; 110: 315-322.

[64] H. J. Yim, J. H. Kim, H. H. Han, H. Kwak. Influence of Portland cement and ground-granulated blast-furnace slag on bleeding of fresh mix. Construction and Building Materials. 2015; 80: 132-140.

[65] J. J.Thomas, H. M. Jennings, J. J. Chen. Influence of nucleation seeding on the hydration mechanisms of tricalcium silicate and cement. Journal of Physical Chemistry C. 2009; 113: 4327-4334.

[66] V. K. Peterson, A. E. Whitten. Hydration processes in tricalcium silicate: application of the boundary nucleation model to quasielastic neutron scattering data. Journal of Physical Chemistry C. 2009; 113: 2347-2351.

[67] S. Garrault, E. Finot, E. Lesniewska, A. Nonat. Study of C-S-H growth on C_3S surface during its early hydration. Materials and Structures. 2005; 38: 435-442.

[68] A. Kumar, S. Bishnoi, K. Scrivener. Modelling early age hydration kinetics of alite. Cement and Concrete Research. 2012; 42: 903-918.

[69] T. Oey, J. Stoian, J. Li, C. Vong, M. Balonis, A. Kumar, W. Franke, G. Sant. Comparison of $Ca(NO_3)_2$ and $CaCl_2$ Admixtures on Reaction, Setting, and Strength Evolutions in Plain and Blended Cementing Formulations. Journal of Materials Civil Engineering. 2014; 04014267-1 04014267-12.

[70] A. Kumar, G. Sant, C. Patapy, C. Gianocca, K. Scrivener. The influence of sodium and potassium hydroxide on alite hydration: Experiments and simulations. Cement and Concrete Research. 2012; 42; 1513-1523.

[71] N. Ukrainczyk. Kinetic modeling of calcium aluminate cement hydration. Chemical Engineering Science. 2010; 65: 5605-5614.

[72] S. Garrault, A. Nonat, Hydrated layer formation on tricalcium and dicalcium silicate surfaces: experimental study and numerical simulations. Langmuir 2001; 17: 8131-8138.

[73] J. W. Cahn. The kinetics of grain boundary nucleated reactions. Acta Metallugica. 1956; 4: 449-459.

[74] R. Fernandez, F. Martirena, and K. L. Scrivener. The Origin of the Pozzolanic Activity of Calcined Clay Minerals: A Comparison between Kaolinite, Illite and Montmorillonite, Cement and Concrete Research. 41, 113-122 (2011).

[75] K. Scrivener, NANOCEM Internal Communication, (2003).

[76] V. L. Bonavetti, V. F. Rahhal, and E. F. Irassar. Studies on the Carboaluminate Formation in Limestone Filler-Blended Cements, Cement and Concrete Research. 31, 853-859 (2001).

[77] M. Nikola, and C. Jolicoeur. Influence of superplasticizers on the rheology and stability of limestone and cement pastes. Cement and Concrete Reseach. 38, 907-919 (2008).

[78] D. L. Rayment, and A. J. Majumdar. The Composition of the C-S-H Phases in Portland Cement Pastes. Cement and Concrete Research. 12, 753-764 (1982).

[79] T. Matschei, B. Lothenbach, and F. P. Glasser. The role of calcium carbonate in cement hydration. Cement and Concrete Research. 37, 551-558 (2007).

[80] T. Matschei, B. Lothenbach, and F. P. Glasser. Thermodynamic Properties of Portland cement hydrates in the system $CaO–Al_2O_3–SiO_2–CaSO_4–CaCO_3–H_2O$. Cement and Concrete Research. 37, 1379-1410 (2007).

[81] S. Mindess, J. F. Young, D. Darwin, Concrete, 2nd edition, Prentice Hall, NJ, 2003.

[82] F. J. Peryea, and J. A. Kittrick. Relative solubility of corundum, gibbsite, boehmite, and diaspore at standard state conditions. Clay and Clay Minerals. 36, 391-396 (1988).

[83] J. Zhang, and G. W. Scherer, Comparison of Methods for Arresting Hydration of Cement, Cement and Concrete Research. 41, 1024-1036 (2011).

[84] American Mineralogist Crystal Structure Database. Available at: http://rruff.geo.arizona. edu/AMS/amcsd.php.

[85] G. Le-Saout, V. Kocaba, and K. Scrivener, Application of the Rietveld Method to the Analysis of Anhydrous Cement. Cement and Concrete Research. 41, 133-148, (2011).

[86] B. H. O'Connor, D. R.. Mark. Application of the Rietveld refinement procedure in assaying powdered mixtures. Powder Diffraction, 01, 2-6, (1988).

[87] D. Jansen, g. N. Friedlinde, S. Christopher, J. Neubauer. A remastered external standard method applied to the quantification of early OPC hydration. Cement and Concrete Research, 6, 602-608 (2011).

[88] G. Le-Saoût, B. Lothenbach, A. Hory, T. Higuchi, F. Winnefeld. Hydration of Portland cement with additions of calcium sulfoaluminates. Cement and Concrete Research, 81-94, (2013).

[89] D. A. Kulik, T. Wagner, S. V. Dmytrieva, G. Kosakowski, F. F. Hingerl, K. V. Chudnenko, and U. R. Berner. GEM-Selektor Geochemical Modeling Package: Revised Algorithm and

GEMS3K Numerical Kernel for Coupled Simulation Codes. Computational Geosciences. 17, 1-24 (2013).

[90] M. Antoni, J. Rossen, F. Martirena, K. Scrivener. Cement substitution by a combination of metakaolin and limestone. Cement and Concrete Research. 12, 1579-1589 (2012).

[91] W. Kunther, B. Lothenbach, K. Scrivener. On the Relevance of Volume Increase for the Length Changes of Mortar Bars in Sulfate Solutions. Cement and Concrete Research. 46, 23-29 (2013).

[92] F. Deschner, B. Lothenbach, F. Winnefeld, J. Neubauer. Effect of temperature on the hydration of portland cement blended with siliceous fly ash. Cement and Concrete Research.52, 169-181 (2013).

[93] M. B. Haha, B. Lothenbach, G. Le-Saout, F. Winnefeld. Influence of slag chemistry on the hydration of alkali-activated blast-furnace slag—Part II: Effect of Al_2O_3. Cement and Concrete Research. 42, 74-83 (2012).

[94] L. Pelletier-Chaignat, F. Winnefeld, B. Lothenbach, C. J. Müller. Beneficial use of limestone filler with calcium sulphoaluminate cement." Construction and Building Materials. 26, 619-627 (2012).

[95] D. A. Kulik, and M. Kersten. Aqueous Solubility Diagrams for Cementitious Waste Stabilization Systems: II, End-Member Stoichiometries of Ideal Calcium Silicate Hydrate Solid Solutions. Journal of the American Ceramic Society. 84, 3017-3026 (2001).

[96] J. W. Bullard, H. M. Jennings, R. A. Livingston, A. Nonat, G. W. Scherer, J. S. Schweitzer, K. Scrivener, J. J. Thomas. Mechanisms of Cement Hydration. Cement and Concrete Research. 41, 1208-1223. (2011).

[97] M. D. Andersen, H. J. Jakobsen, J. Skibsted. Incorporation of Aluminum in the Calcium Silicate Hydrate (C-S-H) of Hydrated Portland Cements: A High-Field 27Al and 29Si MAS NMR Investigation. Inorganic Chemistry. 42, 2280-2287 (2003).

[98] T. Matschei, Thermodynamics of cement hydration. Ph.D. Thesis., Aberdeen University, Scotland (2007).

[99] B. Lothenbach, and F. Winnefeld. Thermodynamic Modelling of the Hydration of Portland Cement. Cement and Concrete Research. 36, 209-226 (2006).

[100] M. Sacerdoti, E. Passaglia. The Crystal Structure of Katoite and Implications within the Hydrogrossular Group of Minerals. Bulletin de minéralogie, 108, 1-8 (1985).

[101] T. Shoji. $Ca_3AI_2(SiO4)_3$-$Ca_3AI_2(O_4H_4)_3$ Series Garnet: Composition and Stability. Joutal of the Mineralogical Society of Japan. 11, 359-372 (1974).

[102] T. G. Jappy, F. P. Glasser. Synthesis and Stability of Silica-Substituted hydrogarnet $Ca_3Al_2Si_{3-x}O_{12-4x}(OH)_{4x}$ Advances in Cement Research. 4, 1-8 (1991).

[103] Z. Yang, H. Fischer, and R. Polder. Modified Hydrotalcites as a New Emerging Class of Smart Additive of Reinforced Concrete for Anticorrosion Applications: A Literature Review. Materials and Corrosion. 64, 1066-1074 (2013).

[104] Taylor, Harry FW. Cement chemistry. 2nd Edition, Thomas Telford, (1997).

[105] L. J. Vandeperre, M. Liska, A. Al-Tabbaa. Microstructures of Reactive Magnesia Cement Blends. Cement and Concrete Composites. 30, 706-714 (2008).

[106] K. G. Ahari, J. H. Sharp, W. E. Lee. Hydration of Refractory Oxides in Castable Bond Systems—I: Alumina, Magnesia, and Alumina–Magnesia Mixtures. Journal of the European Ceramic Society. 22, 495-503 (2002).

[107] K. G. Ahari, J. H. Sharp, W. E. Lee. Hydration of Refractory Oxides in Castable Bond Systems—II: Alumina–Silica and Magnesia–Silica Mixtures. Journal of the European Ceramic Society. 23, 3071-3077 (2003).

[108] R. Snellings, A. Salze, and K. Scrivener. Use of X-ray diffraction to quantify amorphous supplementary cementitious materials in anhydrous and hydrated blended cements. Cement and Concrete Research. 64, 89-98 (2014).

[109] K. Scrivener, B. Lothenbach, N. De Belie, E. Gruyaert, J. Skibsted, R. Snellings, A. Vollpracht. TC 238-SCM: Hydration and Microstructure of Concrete with SCMs. Matererials and Structures. 48, 835-862 (2015).

[110] P. Gu, J. J. Beaudoin, E. G. Quinn, R. E. Myers. Early Strength Development and Hydration of Ordinary Portland Cement/Calcium Aluminate Cement Pastes. Advances in Cement Based Materials. 6, 53-58 (1997).

[111] P. Gu, J. J. Beaudoin. A Conduction Calorimetric Study of Early Hydration of Ordinary Portland Cement/High Alumina Cement Pastes. Journal of Material Science. 32, 3875-3881 (1997).

[112] H. J. Kuzel. Initial Hydration Reactions and Mechanisms of Delayed Ettringite Formation in Portland Cements. Cement and Concrete Composites. 18, 195-203 (1996).

[113] A. Violante, P. M. Huang. Formation Mechanism of Aluminum Hydroxide Polymorphs. Clay and Clay Minerals. 41, 590-597 (1993).

[114] D. Damidot, S. Stronach, A. Kindness, M. Atkins, F. P. Glasser. Thermodynamic Investigation of the CaO-Al_2O_3-$CaCO_3$-H_2O Closed System at 25 C and the Influence of Na_2O. Cement and Concrete Research. 24, 563-572 (1994).

[115] D. Damidot, B. Lothenbach, D. Herfort, F. P. Glasser. Thermodynamics and Cement Science. Cement and Concrete Research. 41, 679-695 (2011).

[116] D. P. Bentz, Modeling the Influence of Limestone Filler on Cement Hydration Using CEMHYD3D. Cement and Concrete Composites. 28, 124-129 (2006).

[117] A. S. Silva, A. Gameiro, J. Grilo, R. Veiga, A. Velosa. Long-Term Behavior of Lime–Metakaolin Pastes at Ambient Temperature and Humid Curing Condition. Applied Clay Science. 88, 49-55 (2014).

[118] P. S. De Silva, F. P. Glasser. Phase Relations in the System CaO-Al_2O_3-SiO_2-H_2O Relevant to Metakaolin-Calcium Hydroxide Hydration. Cement and Concrete Research. 23, 627-639 (1993).

[119] K. Kwan, J. LaRosa-Thompson, M. W. Grutzeck. Structures and Phase Relations of Aluminum-Substituted Calcium Silicate Hydrate. Journal of the American Ceramic Society. 79, no. 4 (1996): 967-971.

[120] G. Puerta-Falla, G. Falzone, G.Sant. Unpublished Results, University of California Los Angeles, (2014).

[121] J. M. Makar T. Sato. The effect of drying method on ordinary portland cement surfaces during the early stages of hydration. Materials and structures. 46, 1-12 (2013).

[122] K. Vance, A. Kumar, G. Sant, N. Neithalath. The rheological properties of ternary binders containing portland cement, limestone, and metakaolin or fly Ash. Cement and Concrete Research. 52, 196-207 (2013).

[123] M. Zajac, M. B. Haha. Experimental investigation and modeling of hydration and performance evolution of fly ash cement. Materials and structures. 47, 1259-1269 (2014).

[124] P. Faucon, T. Charpentier, A. Nonat, J.C. Petit. Triple-quantum two-dimensional 27Al magic angle nuclear magnetic resonance study of the aluminum incorporation in calcium silicate hydrates. Journal of the American Chemical Society. 120(46), 12075–12082, (1998)

[125] D. Damidot, F. P. Glasser. Investigation of the $CaO-Al_2O_3-SiO_2-H_2O$ System at 25°C by Thermodynamic Calculations. Cement and Concrete Research. 25, 22-28 (1995).

[126] M. Balonis, F. P. Glasser. The Density of Cement Phases. Cement and Concrete Research. 39, 733-739 (2009).

[127] M. Balonis, The Influence of Inorganic Chemical Accelerators and Corrosion Inhibitors on the Mineralogy of Hydrated Portland Cement Systems. Ph.D. Thesis., University of Aberdeen, Scotland (2010).

[128] M. Whittaker, M. Zajac, M. Ben Haha, F. Bullerjahn, L. Black. The Role of the Alumina Content of Slag, Plus the Presence of Additional Sulfate on the Hydration and Microstructure of Portland Cement-Slag Blends. Cement and Concrete Research. 66, 91-101 (2014).

[129] L. Baquerizo, T. Matschei, K. Scrivener. The impact of water chemical potential on the hydration states of Monosulfoaluminate. Presented at the 31st cement and concrete Science Conference, London, England, (2011).

[130] G. Renaudin, A. Mesbah, C. Cau-dit-Coumes, F. Frizon, F. Leroux, Chloride and carbonate immobilisation by monosulfoaluminate: study of the solid solutions in the CO_3^{2-} - Cl^- - SO_4^{2-} AFm systems, XIII International Congress on the Chemistry of Cement (ICCC), Madrid, Conference Proceedings (2011).

[131] G. Sant. Unpublished results. University of California Los Angles-UCLA (2014).

[132] M. Nouri-Khezrabad, M. A. L. Braulio, V. C. Pandolfelli, F. Golestani-Fard, H. R. Rezaie. Nano-Bonded Refractory Castables. Ceramics International. 39, 3479-3497 (2013).

[133] J. Moon, J. E. Oh, M. Balonis, F. P. Glasser, S. M. Clark, P. J.M. Monteiro. High Pressure Study of Low Compressibility Tetracalcium Aluminum Carbonate Hydrates $3CaO{\cdot}Al_2O_3{\cdot}CaCO_3{\cdot}11H_2O$. Cement and Concrete Research. 42 , 105-110 (2012).

[134] S. Das, M. Aguayo, V. Dey, R. Kachala, B. Mobasher, G. Sant, N. Neithalath. The Fracture Response of Blended Formulations Containing Limestone Powder: Evaluations Using Two Parameter Fracture Model and Digital Image Correlation. Cement and Concrete Composites. 53, 316-326 (2014).

[135] K. De Weerdt, M. Ben Haha, G. Le Saout, K. O. Kjellsen, H. Justnes, and B. Lothenbach. Hydration Mechanisms of Ternary Portland Cements Containing Limestone Powder and Fly Ash. Cement and Concrete Research. 41, no. 3 (2011): 279-291.

[136] J. Moon, J. E. Oh, M. Balonis, F. P. Glasser, S. Clark, P. J. M. Monteiro, Pressure induced reactions amongst calcium aluminate hydrate phases. Cement and Concrete Research. 41(6), 571-578, (2012)

[137] R. J. Myers, E. L'Hôpital, J. L. Provis, B. Lothenbach. Effect of temperature and aluminum on calcium (alumino) silicate hydrate chemistry under equilibrium conditions. Cement Concrete Research. 68, 83-93 (2015).

[138] S.R. Klaus, J. Neubauer, F. Goetz-Neunhoeffer F. Hydration kinetics of CA_2 and CA—investigations performed on a synthetic calcium aluminate cement. Cement and Concrete Research 43, 62-69 (2013).

[139] R.J Mangabhai, F.P. Glasser. Calcium Aluminate Cements, IOM communications, London, UK (2001).

[140] R. Shahwana, P. Barnes, J. Bensted, X. Turrillas. Conversion of calcium aluminate cement hydrates re-examined with synchrotron energy-dispersive diffraction. Journal of materials science letters 13 (17): 1232-1234 (1994).

[141] N. Ukrainczyk, J. Šipušić, P. Dabić, T. Matusinović. Microcalorimetric study on calcium aluminate cement hydration – 13th International conference on Materials, Processes, Friction and Wear, pp. 382-388 (2008).

[142] G. Puerta-Falla, M. Balonis, G. Le-Saout, G. Falzone, C. Zhang, N. Neithalath, G. Sant. Elucidating the role of the aluminous source on limestone reactivity in cementitious materials, Journal of the American Ceramic Society 98(12): 4076-4089 (2015).

[143] National Center for Biotechnology Information (NCBI) – PubChem database. Available at https://www.ncbi.nlm.nih.gov/pccompound. Accessed on 12/10/2015

[144] FIZ/NIST - Inorganic crystal structure database (ICSD) (version 2009/1). Available for purchase at http://www.nist.gov/srd/nist84.cfm.

[145] Mineralogical Society of America - American mineralogist crystal structure database. Available at http://rruff.geo.arizona. edu/AMS/amcsd.php. Accessed on 01/15/2015.

[146] D. Kulik. GEMS-PSI 2.1. Available at http://les.web.psi.ch/ Software/GEMS-PSI/. Accessed 06/18/2013.

[147] R.J. Myers, B. Lothenbach, S.A. Bernal and J.L Provis. Thermodynamic modelling of alkali-activated slag cements. Applied Geochemistry 61: 233-247.

[148] L.H.J Martin, F. Winnefeld, C.J. Müller, B. Lothenbach. Contribution of limestone to the hydration of calcium sulfoaluminate cement. Cement and Concrete Composites 62: 204-211 (2015).

[149] J.J. Thomas, H.M. Jennings. Free-Energy-Based Model of Chemical Equilibria in the $CaO–SiO_2$-H_2O System. Journal of the American Ceramic Society 81(3): 606-612 (1998).

[150] P. Scherrer Institute. GEMS: Gibbs free energy software for geochemical modeling. Available at http://gems.web.psi.ch/. Accessed 06/18/2015.

[151] B. Lothenbach. CEMDATA. Available at http://www.empa.ch/web/s308/cemdata. Accessed 06/18/2014.

[152] Geoscience for a sustainable earth. Mineral species data base. Available at http://thermoddem.brgm.fr/data/mineraux.php. Accessed on 01/15/2015

[153] K. Önder, I.O. Yaman, M. Tokyay. Compressive strength development of calcium aluminate cement–GGBFS blends. Cement and Concrete Composites 35(1): 163-170 (2013).

[154] D.R. Johnson, W.A. Robb. Gaylussite: thermal properties by simultaneous thermal analysis. American Mineralogist 58: 778-784 (1973).

[155] M. Hartmant, O. Trnka, V. Vesely, K. Svodoba K. Thermal dehydration of the sodium carbonate hydrates. Chemical Engineering Communications 185(1): 1-16 (2001).

[156] A. Steudel, D. Mehl, K. Emmerich. Simultaneous thermal analysis of different bentonite–sodium carbonate systems: an attempt to distinguish alkali-activated bentonites from raw materials. Clay Minerals 48(1): 117-128 (2013).

[157] L.G. Baquerizo, T. Matschei, K. Scrivener, M. Saeidpour, L Wadsö. Hydration states of AFm cement phases. Cement and Concrete Research 73: 143-157 (2015).

[158] L.G. Baquerizo. Impact of water activity on the mineralogy of hydrated cement Ph.D. diss., École Polytechnique Fédérale de Lausanne, Lausanne, Switzerland (2015).

[159] V.R.L. Constantino, T.J. Pinnavaia. Basic Properties of Mg2+1-x Al3+x Layered Double Hydroxides Intercalated by Carbonate, Hydroxide, Chloride, and Sulfate Anions. Inorganic Chemistry, 34, 883-892 (1995).

[160] S. Mitaye, T. Kumura. Synthesis of New Hydrotalcite-Like Compounds and their Physico-Chemical Properties. Chemistry Letters 2, 2, 843-848 (1973).

[161] M. Meyn, K. Beneke, G. Lagaly. Anion-Exchange Reactions of Layered Double Hydroxides. Inorganic Chemistry. 29, 5201-5207 (1990).

[162] V. Rives. Layered double hydroxides: present and future. Nova Publishers, New York-USA, 2001.

[163] P.S. Braterman, Z.P. Xu, F. Yarberry. Handbook of Layered Materials. New York-USA, 2004.

[164] C. Gomes-Silva, Y. Bouizi, Y. Fornés, H. García. Layered Double Hydroxides as Highly Efficient Photocatalysts for Visible Light Oxygen Generation from Water. Journal of the American Chemical Society. 131, 13833-13839 (2009).

[165] C. Depège, F.Z. El-Metoui, C. Forano, A. De-Roy, J. Dupuis, J.P. Besse. Polymerization of Silicates in Layered Double Hydroxides. Chemistry of Materials. 8, 952-960 (1996).

[166] K.H. Goh, T.T. Lim, Z. Dong. Application of Layered Double Hydroxides for Removal of Oxyanions: A Review. Water Research. 42, 1343-1368 (2008).

[167] F. Leroux, J.P. Besse. Polymer Interleaved Layered Double Hydroxide: A New Emerging Class of Nanocomposites. Chemistry of Materials. 13, 3507-3515 (2001).

[168] M. Darder, M. López-Blanco, P. Aranda, F. Leroux, E. Ruiz-Hitzky. Bio-Nanocomposites Based on Layered Double Hydroxides. Chemistry of Materials. 17, 1969-1977 (2005).

[169] M. Zammarano, M. Franceschi, S. Bellayer, J.W. Gilman, M. Meriani. Preparation and Flame Resistance Properties of Revolutionary Self-Extinguishing Epoxy Nanocomposites Based on Layered Double Hydroxides. Polymer. 46, 9314-9328 (2005).

[170] J. Das, B.S. Patra, N. Baliarsingh, K.M. Parida. Adsorption of Phosphate by Layered Double Hydroxides in Aqueous Solutions. Applied Clay Science. 32, 252-260 (2006).

[171] Y. You, G.F. Vance, H. Zhao. Selenium Adsorption on Mg–Al and Zn–Al Layered Double Hydroxides. Applied Clay Science. 20, 13-25 (2001).

[172] B.M. Choudary, S. Madh, N.S. Chowdari, M.L. Kantam, B. Sreedhar. Layered Double Hydroxide Supported Nanopalladium Catalyst for Heck-, Suzuki-, Sonogashira-, and Stille-Type Coupling Reactions of Chloroarenes. Journal of the American Chemical Society. 124, 14127-14136 (2002).

[173] F. Cavani, F. Trifirò, A. Vaccari. Hydrotalcite-Type Anionic Clays: Preparation, Properties and Applications. Catalysis Today. 11, 173-301 (1991).

[174] M.K. Ram-Reddy, Z.O. Xu, G.Q. Lu, J.C. Diniz-da-Costa. Layered Double Hydroxides for CO2 Capture: Structure Evolution and Regeneration. Industrial & Engineering Chemistry Research. 45, 7504-7509 (2006).

[175] V. Ambrogi, G. Fardella, G. Grandolini, L. Perioli. Intercalation Compounds of Hydrotalcite-like Anionic Clays with Anti-inflammatory Agents—I: Intercalation and in Vitro Release of Ibuprofen. International Journal of Pharmaceutics. 220, 23-32 (2001).

[176] V. Ambrogi, G. Fardella, G. Grandolini, L. Perioli, M.C. Tiralti. Intercalation Compounds of Hydrotalcite-like Anionic Clays with Anti-inflammatory agents, II: Uptake of Diclofenac for a Controlled Release Formulation. AAPS. International Journal of Pharmaceutics. 3, 77-82 (2002).

[177] S.Y. Kwak, W.M. Kriven, M.A. Wallig, J.H. Choy. Inorganic Delivery Vector for Intravenous Injection. Biomaterials. 25, 5995-6001 (2004).

[178] K.M. Tyner, M.S. Roberson, K.A. Berghorn, L. Li, R.F. Gilmour, C.A. Batt, E.P. Giannelis. Intercalation, Delivery, and Expression of the Gene Encoding Green Fluorescence Protein Utilizing Nanobiohybrids. Journal of Controlled Release. 100, 399-409 (2004).

[179] F. Li, J. Liu, D.G. Evans, X. Duan. Stoichiometric Synthesis of Pure MFe2O4 (M= Mg, Co, and Ni) Spinel Ferrites from Tailored Layered Double Hydroxide (Hydrotalcite-like) Precursors. Chemistry of Materials. 16, 1597-1602 (2004).

[180] J.W. Boclair, P.S. Braterman, J. Jiang, S. Lou, F. Yarberry. Layered Double Hydroxide Stability. 2. Formation of Cr (III) Containing Layered Double Hydroxides Directly from Solution. Chemistry of Materials. 11, 303-307 (1999).

[181] S. Miyata. Anion Exchange Properties of Hydrotalcite-like Compounds. Clays and Clay Minerals. 31, 305-311 (1983).

[182] J.W. Boclair, P.S. Braterman. Layered Double Hydroxide Stability. 1. Relative Stabilities of Layered Double Hydroxides and their Simple Counterparts. Chemistry of Materials. 11, 298-302 (1999).

[183] Z.P. Xu, G.S. Stevenson, C.Q. Lu, G.Q. Lu. Bartlett, P.F.; Gray, P.P. Stable Suspension of Layered Double Hydroxide Nanoparticles in Aqueous Solution. Journal of the American Chemical Society. 128, 36-37 (2006).

[184] M. Balonis, B. Lothenbach, G. Le-Saout, F.P. Glasser. Impact of Chloride on the Mineralogy of Hydrated Portland Cement Systems Cement and Concrete Research. 40, 1009-1022 (2010).

[185] A.M. Fogg, J.S. Dunn, S.G. Shyu, D.R. Cary, D. O'Hare. Selective Ion Exchange Intercalation of Isomeric Dicarboxylate Anions into the Layered Double Hydroxide [LiAl2(OH)6]Cl· H2O. Chemistry of Materials. 10, 351-355 (1998).

[186] Z. Liu, R. Ma, M. Osada, N. Iyi, Y. Ebina, K. Takada, T. Sasaki. Synthesis, Anion Exchange, and Delamination of Co-Al Layered Double Hydroxide: Assembly of the Exfoliated Nanosheet/Polyanion Composite Films and Magneto-optical Studies. Journal of the American Chemical Society. 128, 4872-4880 (2006).

[187] A.I. Khan, D. O'Hare. Intercalation Chemistry of Layered Double Hydroxides: Recent Developments and Applications. Journal of Materials Chemistry. 12, 3191-3198 (2002).

[188] G. Varga, A. Kukovecz, Z. Kónya, L. Korecz, S. Muráth, Z. Csendes, G. Peintler, S. Carlson, P. Sipos, I. Pálinkó. Mn (II)–Amino Acid Complexes Intercalated in CaAl Layered Double Hydroxide Well Characterized, Highly Efficient, Recyclable Oxidation Catalysts. Journal of Catalysis. 335, 125-134 (2016).

[189] J. Plank, Z. Dai, P.R. Andres. Preparation and Characterization of New Ca–Al–Polycarboxylate Layered Double hydroxides. Materials Letters. 60, 3614-3617 (2006).

[190] F.P. Glasser, A. Kindness, S.A. Stronach, S.A. Stability and Solubility Relationships in AFm Phases: Part I. Chloride, Sulfate and Hydroxide. Cement and Concrete Research. 29, 861-866 (1999).

[191] C.A. Johnson. Cement Stabilization of Heavy-Metal-Containing Wastes Geological Society Special Publication. 236, 595-606 (2004).

[192] I. Baur, C.A. Johnson. The Solubility of Selenate-AFt ($3CaO{\cdot}Al_2O_3{\cdot}3CaSeO_4$ 37.5 H_2O) and selenate-AFm ($3CaO{\cdot}$ Al_2O_3 $CaSeO_4$ xH_2O). Cement and Concrete Research. 33, 1741-1748 (2003).

[193] I.R.B. Keller. The Immobilization of Heavy Metals and Metalloids in Cement Stabilized Wastes: A Study Focusing on the Selenium Oxyanions SeO_3^{2-} and SeO_4^{2-}. PhD dissertation. Universität Zürich, 2002.

[194] A, Bonnefont, F. Argoul, M.Z. Bazant. Analysis of Diffuse Layer Effects on Time Dependent Interfacial Kinetics. Journal of Electroanalytical Chemistry. 500, 52-61 (2001).

[195] C.F. Dickinson, G.R. Heal. Solid Liquid Diffusion Controlled Rate Equations. Thermochimica Acta. 340, 89-103 (1999).

[196] G. Renaudin, M. François. The lamellar double-hydroxide (LDH) compound with composition $3CaO{\cdot}Al_2O_3$ Ca $(NO_3)_2.10\ H_2O$. Acta Crystallographica Section C. 55, 835-838 (1999).

[197] M. Balonis, F.P. Glasser. Calcium Nitrite Corrosion Inhibitor in Portland Cement: Influence of Nitrite on Chloride Binding and Mineralogy. Journal of the American Ceramic Society. 94, 2230-2241 (2011).

[198] F. Helfferich, M.S. Plesset. Ion Exchange Kinetics. A Nonlinear Diffusion Problem. The Journal of Chemical Physics. 28, 418-424 (1958).

[199] F. Helfferich. Ion Exchange Kinetics III. Experimental Test of the Theory of Particle Diffusion Controlled Ion Exchange. Journal of Chemical Physics. 66, 39-44 (1962).

[200] F. Helfferich. Ion Exchange Kinetics IV. Demonstration of the Dependence of the Interdiffusion Coefficient on Ionic Composition. Journal of Chemical Physics. 67, 1157-1159 (1963).

[201] Crank, J. The Mathematics of Diffusion. Oxford university press, 1979.

[202] E.L. Shock, D.D. Sassani, M. Willis, D.A. Sverjensky. Inorganic Species in Geologic Fluids: Correlations Among Standard Molal Thermodynamic Properties of Aqueous Ions and Hydroxide Complexes. Geochimica et Cosmochimica Acta. 61, 907-950 (1997).

[203] H. Eyring. The Activated Complex in Chemical Reactions. The Journal of Chemical Physics. *3* (2), 107–115 (1935).

[204] J.I. Steinfeld, J.S. Francisco, W,L. Hase. Chemical Kinetics and Dynamics, 2nd edition. Pearson, 1998.

[205] F.G. Helfferich. Ion exchange. Courier Corporation, 1962.

[206] M.M. Bazri, M. Mohseni. Impact of Natural Organic Matter Properties on the Kinetics of Suspended Ion Exchange Process. Water Research. 91, 147-155 (2016).

[207] C. Su, R.W. Puls. Kinetics of Trichloroethene Reduction by Zerovalent Iron and Tin: Pretreatment Effect, Apparent Activation Energy, and Intermediate Products. Environmental Science & Technology. 33, 163-168 (1999).

[208] A.C. Lasaga. Chemical kinetics of Water-Rock Interactions. Journal of Geophysical Research: Solid Earth. 89, 4009-4025 (1984).

[209] G. Sant, F. Rajabipour, J. Weiss. The Influence of Temperature on Electrical Conductivity Measurements and Maturity Predictions in Cementitious Materials During Hydration. Indian Concrete Journal. 82, 7-16 (2008).

[210] J.D. Rimstidt, H.L. Barnes. The Kinetics of Silica-Water Reactions. Geochimica et Cosmochimica Acta. 44, 1683-1699 (1980).

[211] J.D. Rimstidt, P.M. Dove, Mineral/Solution Reaction Rates in a Mixed Flow Reactor: Wollastonite Hydrolysis. Geochimica et Cosmochimica Acta. 50, 2509-2516 (1986).

[212] K.S. Spiegler. Transport processes in ionic membranes. Transaction of the Faraday Society. 54, 1408-1428 (1958).

[213] P. Glynn. Solid-Solution Solubilities and Thermodynamics: Sulfates, Carbonates and Halides. Reviews in Minerology and Geochemistry. 40, 481-511 (2000).

[214] P. Glynn. MBSSAS: A Code for the Computation of Margules Parameters and Equilibrium Relations in Binary Solid-Solution Aqueous-Solution Systems. Computers and Geosciences. 17, 907-966 (1991).

[215] P. Glynn, E.J. Reardon, L.N. Plummer, E. Busenberg. Reaction Paths and Equilibrium End-Points in Solid-Solution Aqueous-Solution systems. Geochimica et Cosmochimica Acta. 54, 267-282 (1990).

[216] F. Lippmann. Phase Diagrams Depicting Aqueous Solubility of Binary Mineral Systems. Neues Jahrbuch für Mineralogie – Abhandlungen. 139, 1-25 (1980).

[217] M. Prieto, A. Fernández-González, U. Becker, A. Putnis. Computing Lippmann Diagrams from Direct Calculation of Mixing Properties of Solid Solutions: Application to the Barite-Celestite System. Aquatic Chemistry. 2, 133-146 (2000).

[218] Matschei, T. Thermodynamics of Cement Hydration. PhD dissertation. Aberdeen University, 2007.

[219] J. Moon, J.E. Oh, M. Balonis, F.P. Glasser, S.M. Clark, P.J.M Monteiro. Pressure induced reactions amongst calcium aluminate hydrate phases. Cement and Concrete Research 41, no. 6: 571-578 (2011).

[220] S.M. Clark, B. Colas, M. Kunz, S. Speziale, P.J.M. Monteiro. Effect of pressure on the crystal structure of ettringite. Cement and Concrete Research 38, no. 1: 19-26 (2008).

[221] S.P. Newman, J. William Jones. Synthesis, characterization and applications of layered double hydroxides containing organic guests. New Journal of Chemistry 22, no. 2: 105-115 (1998).

[222] S.K. Yun, T.J. Pinnavaia. Water content and particle texture of synthetic hydrotalcite-like layered double hydroxides. Chemistry of Materials 7, no. 2: 348-354 (1995).

[223] M. Balonis. Internal communication. Laboratory for the chemistry of construction materials-UCLA. 2016.

[224] L.E.I. Chou, R.M Garrels, R. Wollast. Comparative study of the kinetics and mechanisms of dissolution of carbonate minerals. Chemical Geology 78, 269-282 (1989).

[225] Ph. Refait, M. Abdelmoula, J.MR. Génin. Mechanisms of formation and structure of green rust one in aqueous corrosion of iron in the presence of chloride ions. Corrosion Science 40, 1547-1560 (1998).

[226] G. Puerta-Falla, G. Falzone, T. Oey and G. Sant. Unpublished Results, laboratory for the chemistry of construction materials-UCLA, 2015.

[227] L.G. Baquerizo, T. Matschei, K. Scrivener, M. Saeidpour, L. Wadsö. Hydration states of AFm cement phases. Cement and Concrete Research 73, 143-157 (2015).

[228] M. Collepardi. A state-of-the-art review on delayed ettringite attack on concrete. Cement and Concrete Composites 25, no. 4: 401-407 (2003).

[229] T. Oey, A. Kumar, G. Falzone, J. Huang, S. Kennison, M. Bauchy, N. Neithalath, J.W. Bullard, G. Sant. The influence of water activity on the hydration rate of tricalcium silicate. Journal of the American Ceramic Society (2016).